Roadmap for electronic structure, anharmonicity, and electron-phonon calculations in locally disordered inorganic and hybrid halide perovskites

Marios Zacharias, George Volonakis, Laurent Pedesseau, Claudine Katan, Feliciano Giustino, Jacky Even

Marios Zacharias, George Volonakis, Laurent Pedesseau, Claudine Katan, Feliciano Giustino, et al.. Roadmap for electronic structure, anharmonicity, and electron-phonon calculations in locally disordered inorganic and hybrid halide perovskites. Physical Review B, 2026, 113 (8), pp.085118. ⟨10.1103/67c2-yzjw⟩. ⟨hal-05528302⟩

PHYSICAL REVIEW B **113**, 085118 (2026)

Editors' Suggestion

Roadmap for electronic structure, anharmonicity, and electron-phonon calculations in locally disordered inorganic and hybrid halide perovskites

Marios Zacharias,[1,2,*] George Volonakis,[3] Laurent Pedesseau,[1] Claudine Katan,[3]
Feliciano Giustino,[4,5] and Jacky Even[1,†]
[1]*Univ Rennes, INSA Rennes, CNRS, Institut FOTON–UMR 6082, F-35000 Rennes, France*
[2]*Computation-based Science and Technology Research Center, The Cyprus Institute, Aglantzia 2121, Nicosia, Cyprus*
[3]*Univ Rennes, ENSCR, INSA Rennes, CNRS, ISCR–UMR 6226, F-35000 Rennes, France*
[4]*Oden Institute for Computational Engineering and Sciences, The University of Texas at Austin, Austin, Texas 78712, USA*
[5]*Department of Physics, The University of Texas at Austin, Austin, Texas 78712, USA*

(Received 11 June 2025; accepted 22 January 2026; published 12 February 2026)

The role of data in modern materials science becomes more valuable and accurate when effects such as electron-phonon coupling and anharmonicity are included, providing a more realistic representation of finite-temperature material behavior. Furthermore, positional polymorphism, characterized by correlated local atomic disorder usually not reported by standard diffraction techniques, is a critical yet underexplored factor in understanding the electronic structure and transport properties of energy-efficient materials, like halide perovskites. In this manuscript, we present a first-principles methodology for locally disordered (polymorphous) cubic inorganic and hybrid halide perovskites, rooted in the special displacement method, that offers a systematic and alternative approach to molecular dynamics for exploring finite-temperature properties. By enabling a unified and efficient treatment of anharmonic lattice dynamics, electron-phonon coupling, and positional polymorphism, our approach generates essential data to predict temperature-dependent phonon properties, free energies, band gaps, and effective masses. Designed with a high-throughput spirit, this framework has been applied across a range of inorganic and hybrid halide perovskites: $\mathrm{CsPbI_3}$, $\mathrm{CsPbBr_3}$, $\mathrm{CsSnI_3}$, $\mathrm{CsPbCl_3}$, $\mathrm{MAPbI_3}$, $\mathrm{MAPbBr_3}$, $\mathrm{MASnI_3}$, $\mathrm{MAPbCl_3}$, $\mathrm{FAPbI_3}$, $\mathrm{FAPbBr_3}$, $\mathrm{FASnI_3}$, and $\mathrm{FAPbCl_3}$. We provide a comprehensive comparison between theoretical and experimental results and we systematically uncover trends and insights into their electronic and thermal behavior. For all compounds, we demonstrate strong and consistent correlations between local structural disorder, band gap openings, and effective mass enhancements. We present anharmonic phonon quasiparticle dispersions and show that both electron-phonon coupling and thermal expansion contributions to the band gap are significantly affected by local disorder, improving agreement with experiment. Furthermore, we discuss deviations from these trends in Sn-based compounds, which we attribute to the enhanced stereochemical activity of the Sn lone pair. We also present phonon spectral functions of polymorphous structures that illustrate the breakdown of the phonon quasiparticle picture in these soft materials. For hybrid halide perovskites, we introduce the concept of reference structures to address the complex interplay of disordered orientations of MA and FA molecules with the inorganic sublattice distortions, affecting both anharmonicity, transverse optical and longitudinal optical phonon frequencies, and electron-phonon coupling. Our work underscores the potential of integrated, high-throughput computational frameworks to transform the discovery and optimization of halide perovskite photovoltaic devices at finite temperatures.

DOI: 10.1103/67c2-yzjw

I. INTRODUCTION

Halide perovskites, either layered, bulk, nanocrystals, or heterostructures, are attracting immense interest due to their impressive power conversion efficiencies in optoelectronics, with new candidates emerging constantly [1–22]. Several key challenges in the field of halide perovskites remain partially unexplored and continue to be active areas of research. These include gaining a deeper understanding of (i) the complex anharmonic potential energy surface responsible for the formation of local structure/disorder [23–35], anharmonic lattice vibrations [25,30,36–42], and phase stability [25,43–46], and (ii) anharmonic carrier-phonon coupling and its role to the electronic structure renormalization [30,47–50], temperature-dependent optical absorption, photoluminescence (PL) [51–59], carrier mobilities [52,60–64], polaron formation [65–81], and ultrafast nonequillibrium dynamics [69,82–84].

The seminal work by Stoumpos *et al.* [60] has brought to light the strong dependence of structural, optical, and electronic properties of hybrid (organic-inorganic) metal iodide perovskites on composition and synthesis conditions. One key element for understanding the peculiar properties of these materials is the description of correlated local

---

[*] Contact author: zachariasmarios@gmail.com

[†] Contact author: jacky.even@insa-rennes.fr

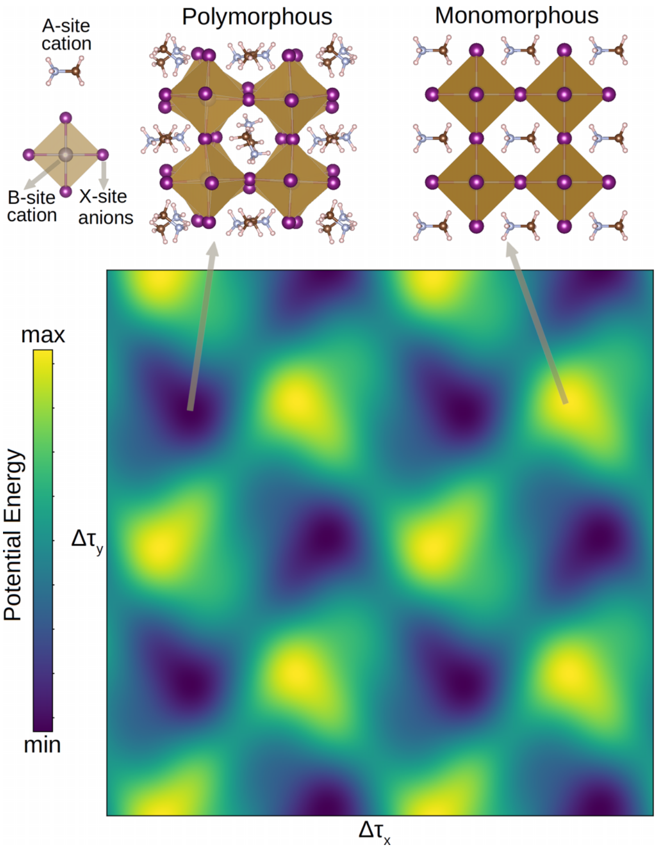

FIG. 1. Top view of the schematic representation of an anharmonic PES showing minima and maxima defined by the polymorphous (locally disordered) and monomorphous halide perovskite structures, respectively. $\Delta\tau$ indicates atomic displacements away from static-equilibrium positions of the monomorphous structure along the Cartesian directions x and y. The example ABX_3 structure used at the top is for $MASnI_3$ and consists of the A-site cation (MA), the B-site metal (Sn), and the X-site halide anions (I). In this study we explore cases where A = methylammonium (MA), formamidinium (FA), or Cs, B = Pb or Sn, and X = I, Br, or Cl.

disorder (positional polymorphism) [26,30,85–87] in the tetragonal and cubic high-symmetry perovskite structures, not distinct in standard diffraction experiments [88,89]. In particular, positional polymorphism represents multiple domains of local disorder at static-equilibrium that define a minimum in the system's anharmonic potential energy surface (PES), as shown in Fig. 1. These domains can be identified experimentally by local probes such as pair distribution functions [24,33,90] or nuclear magnetic resonance spectroscopy [91] and are present in crystals not exclusive to perovskites [92–94]. In halide perovskites, local disorder manifests through B-site (metal) off-centering, which induces the formation of stereochemically active lone pairs [27], octahedral tilting, and a distribution of A-site cations within the octahedral voids. Despite the presence of positional polymorphism in tetragonal and cubic phases, the overall structure, on a *macroscopic level*, retains the average high-symmetry crystallographic form, as reported by traditional diffraction techniques. The quasistatic network of local structures also mimics the very slow structural relaxations [30,93], where the system does not settle into a single minimum but instead fluctuates between multiple low-energy configurations.

Ab initio electronic structure and electron-phonon calculations for halide perovskites typically utilize a simple monomorphous network, which can be described by a minimal unit cell [10,49,62,95–107]. However, this structure is dynamically unstable, corresponding to a local maximum on the PES (Fig. 1). As a result, density-functional theory (DFT) calculations in halide perovskites based on monomorphous cells fail to capture the physics related to the more stable polymorphous networks, which are known to significantly influence the electronic structure [26]. In Ref. [30], relying on the anharmonic special displacement method (ASDM) [42,108,109], we have introduced a bottom-up *ab initio* approach for the exploration of polymorphous structures and a unified treatment of the complex interplay between local disorder, anharmonicity, and electron-phonon coupling. We have demonstrated using the case of inorganic Cs-based halide perovskites that local disorder plays a key role to accurately describe strongly overdamped vibrational dynamics, anharmonic electron-phonon coupling, and temperature-dependent band gaps. In Ref. [110], we have generalized and applied our approach in a high-throughput framework to the computationally more demanding and technologically more significant case of cubic hybrid halide perovskites.

In this paper, we provide a detailed description of our approach and conduct a comprehensive comparative analysis of 12 materials (4 FA-, 4 MA-, and 4 Cs-based compounds) through large-scale calculations for 120 polymorphous structures (i.e., 10 structures each) using supercells. We obtain the following results:

(i) We introduce the concept of reference structures for hybrid halide perovskites, different than the monomorphous structures, where disorder is accounted initially only for the molecules. The reference structures enable the separation of the effects arising from the distinct dynamics of organic molecules and facilitate systematic comparisons with the electronic structure of the corresponding fully polymorphous states.

(ii) We quantify local disorder in terms of B-X bond length and B-X-B bond angle distortions and demonstrate strong correlations with the increase in band gap and effective masses induced by positional polymorphism.

(iii) We demonstrate that the extent of local disorder is influenced by the size of the A-site cation, with FA-based compounds exhibiting the least positional polymorphism, followed by MA-based compounds, and Cs-based compounds displaying the highest degree of polymorphism.

(iv) We compute anharmonic phonons at finite temperatures within the self-consistent phonon theory based on reference structures, and present phonon quasiparticle dispersions for all compounds. Our results compare well with diffuse scattering maps and phonon frequencies measured by various experimental techniques. We also discuss the role of A-site cations and X-site anions to transverse optical (TO) and longitudinal optical (LO) phonon splitting.

(v) We calculate the free energies and Boltzmann-weighted averages of temperature-dependent band gaps of all cubic compounds using several reference and polymorphous structures, to account for configurational entropy effects.

Our results highlight the critical role of local disorder in achieving accurate anharmonic electron-phonon coupling calculations, which result in unprecedented agreement with experiments [44,52,54–59,61,111].

(vi) We distinguish the contributions of thermal expansion and electron-phonon coupling to band gap renormalization, demonstrating that they do not contribute equally, contrary to common assumptions [112,113]. Overall, electron-phonon coupling dominates for Cs-based and MA-based compounds, reaching as high as 97% while for FA-based compounds thermal expansion plays more important role. For locally disordered Sn-based compounds, we find an enhanced thermal expansion contribution to the band gap renormalization due to the enhanced lone pair activity, promoting Sn-I-Sn bond angle bending under lattice expansion.

(vii) We calculate temperature-dependent hole and electron effective masses of all cubic compounds using both reference and polymorphous structures. The effective mass enhancement due to polymorphism and electron-phonon coupling reach as high as one order of magnitude, improving agreement between calculated and measured reduced effective masses.

(viii) We show that, starting from maximally symmetrized reference structures, even one polymorphous configuration can be enough to calculate anharmonic electron-phonon properties in some systems.

(ix) We show that positional polymorphism leads to a continuum of strongly overdamped vibrations and the breakdown of the phonon quasiparticle picture obtained by standard approaches to anharmonicity applied to monomorphous or reference cells [42,47,49].

(x) We demonstrate the role of local disorder to accurately describe the band gap variations across different phases.

We organize the manuscript as follows: In Sec. II we introduce the theory underpinning our electron-phonon coupling, temperature-dependent electron energies, polymorphous structure, and anharmonic phonon calculations via the ASDM. Section III describes our main methodology for computing anharmonic electron-phonon properties in locally disordered halide perovskites, starting from reference structures. In the same section, we show the total energy lowering obtained for locally disordered structures with respect to reference structures and present strong correlations of the band gap widening and effective masses enhancements with bond length and angle variations. We also demonstrate our methodology for computing anharmonic phonon quasiparticle dispersions, and free energies, as well as Boltzmann-weighted averages of temperature-dependent band gaps and effective masses of MAPbBr$_3$ and FAPbI$_3$. In Sec. IV, we provide a case-by-case analysis of all 12 halide perovskites, showing band gaps at the DFT and hybrid functional levels, DFT effective masses, analyzing anharmonic phonon dispersions and TO, LO phonon energies, and temperature-dependent band gaps and effective masses calculated within the ASDM. Where available we compare our results with state-of-the-art *GW* calculations. In the same section, we analyze the electron-phonon and thermal expansion contributions to the band gap renormalization for each material. In Sec. V, we present a general comparison and discussion of our results focusing on electronic structure modifications due to local disorder, the band gap across different polymorphs, LO-TO splitting, the breakdown of the phonon quasiparticle picture, and thermal-induced renormalization. Section VII summarizes our key results and conclusions as well as provides avenues of future work.

II. THEORY

In this work, we employ the ASDM [42,108,109] for the simulation of polymorphous structures, phonon anharmonicity at finite temperatures, and anharmonic electron-phonon coupling. The ASDM is classified as an efficient nonperturbative supercell approach. In this method, atoms are displaced according to a special linear combination of the computed phonon eigenvectors with amplitudes determined by the associated root mean squared displacements. It allows the generation of a single optimal structure that best represents the system at thermal equilibrium within the supercell under study. In other words, the ASDM generates, essentially, deterministic high "quality" locally disordered and thermal configurations, replacing the need for stochastic samplings or molecular dynamics simulations used in nonperturbative simulations of phonon anharmonicity and/or electron-phonon coupling.

A. Electron-phonon coupling

Compared to perturbative methods for electron-phonon coupling [114–122], nonperturbative approaches offer some advantages [108,109,123,124]. For instance, nonperturbative methods inherently capture electron-phonon coupling through the adiabatic response of electrons to nuclear displacements in supercells, eliminating the need for explicit calculation of electron-phonon matrix elements. More, these approaches account for higher-order electron-multiphonon interactions [102] and low-frequency structural relaxations [30], which are known to be important in halide perovskites. Another strength of nonperturbative methods lies in their ability to unify the treatment of anharmonicity and electron-phonon coupling, allowing to explore the complex potential energy surfaces of anharmonic systems [30,50,123,125,126]. This capability is central in this work to seamlessly accommodate positional polymorphism in our first principles calculations. Nonetheless, understanding the physics captured by nonperturbative approaches requires establishing a direct link to perturbative expressions. The standard electron-phonon matrix element is defined as [108,115]

$$g_{nm\nu} = \sqrt{\frac{\hbar}{2M_0\omega_\nu}}\,\langle\psi_n|\,\partial U_{\mathrm{KS}}^{\{\tau\}}/\partial x_\nu\,|\psi_m\rangle, \tag{1}$$

where $\hbar$ is the reduced Planck constant, M_0 is the proton mass, and ψ_n, ψ_m represent two electron states coupled by a phonon of normal coordinate x_ν and frequency ω_ν. U_{KS} is the DFT Kohn-Sham (KS) potential determined by the electron density with the system at static-equilibrium and depends parametrically on the nuclei positions $\{\tau\}$. The KS energy calculated in a fixed nuclear configuration corresponds to a point on the PES.

B. Temperature-dependent electron energies

It is apparent from Fig. 2(a) that whenever the system is in static equilibrium (i.e., when the forces acting on the atoms are zero), it can reside at a local maximum, a local

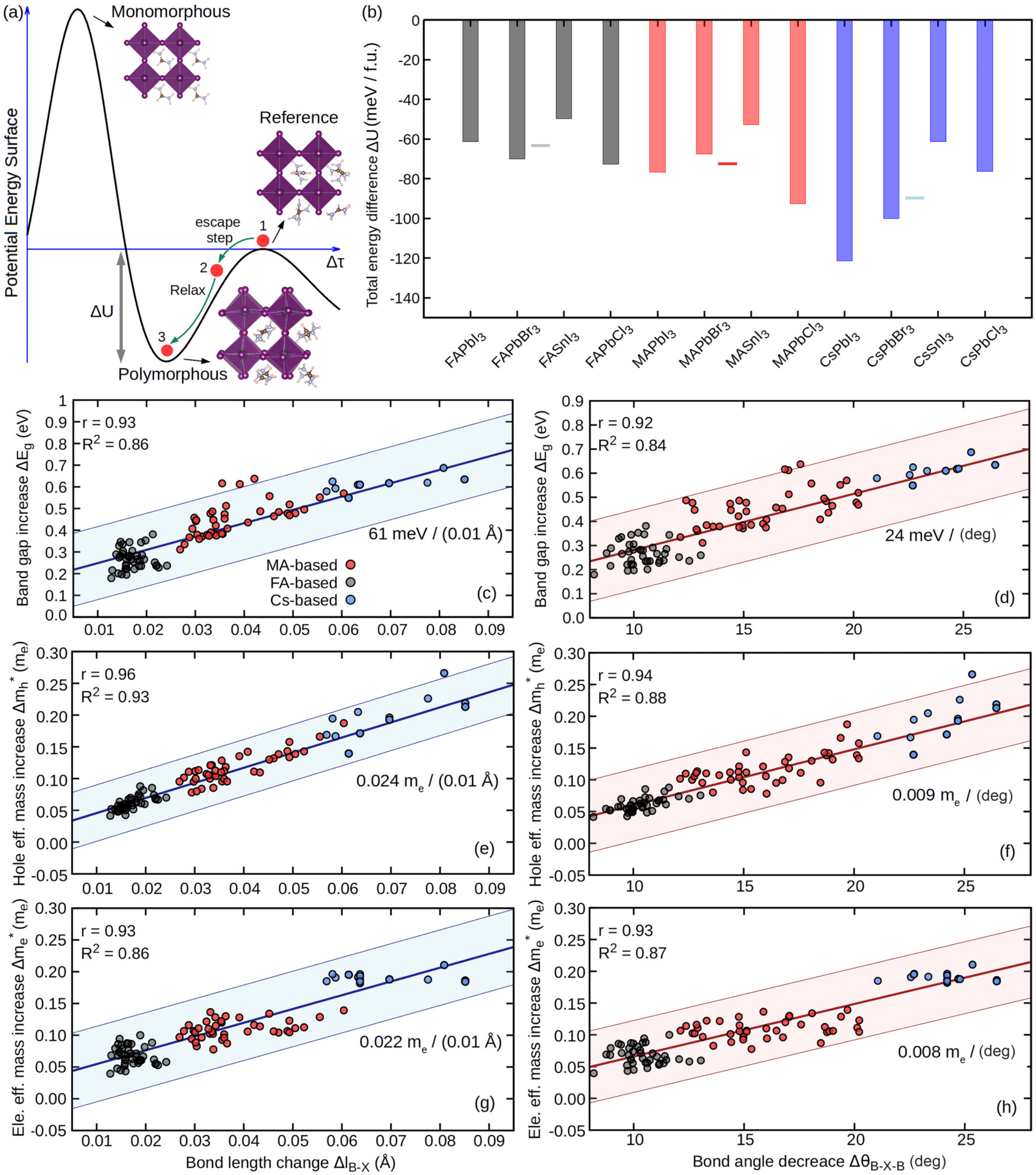

FIG. 2. (a) Schematic representation of the transitions of the PES from the monomorphous to the polymorphous, and from the polymorphous to the reference structure, indicated by ball and stick models of cubic $\mathrm{FAPbI_3}$. (b) DFT total energy lowering per formula unit (ΔU) of polymorphous cubic halide perovskites relative to their reference structures, evaluated using Eq. (11), assuming $T = 300\,\mathrm{K}$, and 10 configurations in $2\times2\times2$ supercells for each system. One formula unit (f.u.) refers to the unit cell containing 5 atoms. Horizontal gray, red, and light-blue lines indicate the mean ΔU of FA-, MA-, and Cs-based compounds, respectively. (c)–(h) Scatter plots showing the dependence of the band gap and effective mass increase due to polymorphism on the average B-X bond length and B-X-B bond angle variations. The 120 data points correspond to 10 polymorphous configurations generated for 4 FA (black), 4 MA (red), and 4 Cs (blue)-based compounds. The straight thick lines represent the least-squares regression fit to the data, with the slopes indicated on each plot. The shaded regions represent three standard deviations on either side of the lines. All calculations refer to the DFT-PBEsol approximation. Our calculations for the band gaps and effective masses include spin-orbit coupling (SOC) effects.

minimum or a saddle point on the PES. In view of Eq. (1), using either a monomorphous, a reference, or a polymorphous structure is expected to have a direct impact on first-principles electron-phonon calculations. Not only a different point on the PES is entering Eq. (1), but also the phonon frequencies ω_ν and electron wavefunctions ψ_n are renormalized by choosing a different structure.

In this work, we focus on electron-phonon renormalized KS energies ε_n which can be written in terms of normal coordinates as [108]

$$\Delta\varepsilon_n(T) = \frac{1}{2}\sum_\nu \frac{\partial^2\varepsilon_n}{\partial x_\nu^2}\sigma_{\nu,T}^2 + \frac{3}{4!}\sum_{\nu,\mu}\frac{\partial^4\varepsilon_n}{\partial x_\nu^2 \partial x_\mu^2}\sigma_{\nu,T}^2\sigma_{\mu,T}^2 + \mathcal{O}(\sigma^6)\cdots. \tag{2}$$

Here, $\Delta\varepsilon_n(T) = \varepsilon_n(T) - \varepsilon_n$, where $\varepsilon_n(T)$ is the electron energy at temperature T and ε_n is the electron energy with the system at static equilibrium. $\sigma_{\nu,T}^2$ represents the mean square displacements of the atoms along a phonon mode given by

$$\sigma_{\nu,T}^2 = \frac{\hbar}{2M_0\omega_\nu}(2n_{\nu,T} + 1), \tag{3}$$

where the $n_{\nu,T} = [\exp(\hbar\omega_\nu/k_\mathrm{B}T) - 1]^{-1}$ is the Bose-Einstein occupation of the mode and k_B is the Boltzmann constant. Eq. (2) is obtained by taking a Taylor expansion of ε_n with respect to the normal coordinates x_ν and applying the standard thermal average as a multivariate Gaussian integral [108].

To make a connection with perturbation theory, we adopt the adiabatic Allen-Heine (AH) theory [127,128] of temperature-dependent band structures and express $\varepsilon_n(T)$ in terms of electron-phonon matrix elements, considering terms up to second order in normal coordinates:

$$\Delta\varepsilon_n^{\mathrm{AH}}(T) = \left[\sum_{\beta\neq n}\frac{|g_{n\beta\nu}|^2}{\varepsilon_n - \varepsilon_\beta} + h_{n\nu\nu}\right](2n_{\nu,T} + 1), \tag{4}$$

where the first term inside the square brackets represents the Fan-Migdal contribution and $h_{n\nu\nu}{=}\hbar/2M_0\omega_\nu \langle\psi_n|\,\partial^2 U_{\mathrm{KS}}^{\{\tau\}}/\partial x_\nu^2\,|\psi_n\rangle$ represents the Debye-Waller contribution to electron-phonon renormalized band structures [115]. We note that the electron-phonon matrix elements [Eq. (1)] entering Eq. (4), when computed within the harmonic approximation, may be ill-defined if the system exhibits imaginary phonon modes. This is usually an artifact of applying the harmonic approximation to an inherently anharmonic system. This underscores the need to explicitly consider the system's anharmonicity, as discussed in Secs. II C and II D. Another source of anharmonicity affecting the electronic structure at finite temperatures is thermal lattice expansion, which is treated separately in this work, as discussed in Ref. [110] and Sec. VI F.

C. Polymorphous structure exploration

At a local maximum (or a saddle point), unstable phonons arise due to the negative curvature of the potential energy surface in certain directions, resulting in imaginary phonon frequencies ($\omega_\nu^2 < 0$) that imply a dynamic instability. Hence, the monomorphous and reference structures, shown in Fig. 2(a), are dynamically unstable. Displacing the atoms of the monomorphous or reference structures along phonon eigenvectors corresponding to imaginary phonons indicates a direction in which the system can lower its energy and move toward a more stable configuration. However, achieving the polymorphous structure (i.e., a local minimum on the PES) through a linear combination of such eigenvectors is a challenging task. Instead, we first test displacing the atoms of the reference structure in a supercell along the phonon eigenvectors associated with imaginary phonons using displacements given by

$$\Delta\tau_{p\kappa\alpha} = (M_0/M_\kappa)^{\frac{1}{2}}\sum_{\nu,\omega_\nu^2<0} e_{p\kappa\alpha,\nu}\, x_\nu. \tag{5}$$

Here p is an index for the unit cells comprising the supercell, α denotes a Cartesian direction, and x_ν represents the normal coordinates that determine the magnitude of displacement. This initial step allows the system to escape from a saddle point [point 1 in Fig. 2(a)] and move toward a more stable configuration [point 2 in Fig. 2(a)], depending on the value of x_ν. As a final step, the system is driven toward a local minimum [point 3 in Fig. 2(a)] by relaxing the atomic positions while keeping the lattice constants fixed.

Using the example of $\mathrm{CsPbI_3}$ for a 2×2×2 supercell, we tested the values $x_\nu = \{0.05, 0.5, 1, 2, 3, 4, 5\}$ Å to initially displace the atoms of the reference structure using Eq. (5), followed by structural relaxation. For $x_\nu = \{0.5, 1, 2\}$ Å, the system reached a polymorphous structure, resulting in a total energy lowering of 121 meV relative to the reference structure. For $x_\nu = \{3, 4, 5\}$ Å, the system converged to a saddle point with a total energy reduction of 108 meV, whereas for $x_\nu = 0.05$ Å, the system returned back to the reference structure.

As a more consistent escape step from the unstable stationary point, we employed Zacharias-Giustino (ZG) displacements, the key element of the ASDM, which are defined as [108]

$$\Delta\tau_{p\kappa\alpha}^{\mathrm{ZG}}(T) = (M_0/M_\kappa)^{\frac{1}{2}}\sum_{\nu,\omega_\nu^2>0} S_\nu\, e_{p\kappa\alpha,\nu}\,\sigma_{\nu,T}. \tag{6}$$

Here, the summation is performed over stable phonons modes with $\omega_\nu^2 > 0$ and S_ν represents signs associated with each eigenvector. These signs are assigned combinatorially by `ZG.x` of EPW [121] to ensure that the anisotropic displacement parameters are closely reproduced [109]. Using $\mathrm{CsPbI_3}$, we tested ZG displacements for $T = 0$ K. While the system after the escape step moves toward a less stable configuration than the reference structure, the final relaxation step leads to a polymorphous structure with the same energy lowering of 121 meV, as achieved using Eq. (5) for $x_\nu = \{0.5, 1, 2\}$ Å. We note that for generating polymorphous structures with distinct atomic coordinates, one can employ different initial sets of ZG displacements by using various permutations of the set of signs S_ν or different temperatures T.

In this work, we employed ZG displacements [Eq. (6)] for $T = 0$ K as the escape step to explore effectively polymorphous structures, rather than using Eq. (5). The ZG method avoids biasing the system toward specific soft-mode distortions, which may otherwise lead to saddle points on the PES after relaxation. In addition, Eq. (6) relies on mode amplitudes determined by phonon occupations via Boltzmann statistics, ensuring that the system is sampled in a manner consistent with the underlying PES. In contrast, Eq. (5) requires an arbitrary choice of displacement amplitude, which may not correspond to a physically meaningful point on the PES.

D. Anharmonic phonons via the ASDM

The degree of polymorphism, reflected by the total energy lowering relative to the reference structure, can also serve as a quantitative measure of the system's anharmonicity. To address anharmonicity within the phonon quasiparticle picture, we employ the self-consistent phonon (SCP) theory [129–131] using the ASDM [42]. The SCP theory has been implemented successfully in several state-of-the-art approaches, including those described in Refs. [132–138].

In the SCP theory, an effective harmonic matrix of interatomic force constants (IFCs) at temperature T is evaluated iteratively until convergence, a process that effectively corresponds to minimizing a reference system's trial free energy F_0 corresponding to a PES U_0. This can be understood in the context of the Gibbs-Bogoliubov inequality [139,140],

$$F(T) \leqslant F_0(T) = \langle U - U_0 \rangle_T + F_{\text{vib}}(T), \tag{7}$$

where F is the true free energy, F_{vib} is the vibrational free energy of the reference system, and U is the PES of the actual system with the thermal average $\langle . \rangle_T$ taken with respect to the eigenstates of the reference system. The inequality in Eq. (7) suggests that variational minimization of the trial free energy $F_0(T)$ of the simpler reference system provides an upper bound on the true free energy $F(T)$ of the more complex anharmonic system.

In Eq. (7) the thermal average $\langle U - U_0 \rangle_T$ is decoupled as $\langle U \rangle_T - \langle U_0 \rangle_T$ due to the linearity of expectation under a normalized probability distribution, with both terms evaluated over the same reference ensemble. Hence, the trial free energy can be expressed with respect to the phonon frequencies of the reference system as follows [42]:

$$\begin{aligned} F_0(T) = \langle U \rangle_T - \frac{M_0}{2} \sum_{\nu} \omega_\nu^2 \, \sigma_{\nu,T}^2 \\ + \sum_{\nu} \left[\frac{\hbar \omega_\nu}{2} - k_{\text{B}} T \ln[1 + n_\nu(T)] \right]. \end{aligned} \tag{8}$$

To minimize the reference system's free energy, it suffices to calculate iteratively the matrix of effective IFCs until self-consistency is achieved, i.e.,

$$C_{p\kappa\alpha,p'\kappa'\alpha'}(T) = \left\langle \frac{\partial^2 U_{\text{KS}}^{\{\tau\}}}{\partial \tau_{p\kappa\alpha} \partial \tau_{p'\kappa'\alpha'}} \right\rangle_T . \tag{9}$$

To reach the above result one needs to perform the derivative of Eq. (8) with respect to the IFCs, $C_{p\kappa\alpha,p'\kappa'\alpha'}$, and find the solution for $\partial F_0(T)/\partial C_{p\kappa\alpha,p'\kappa'\alpha'} = 0$ as derived in Refs. [42] and [140].

In the ASDM for polymorphous systems [42], obtaining an initial set (zeroth iteration) of effective IFCs involves computing the IFCs by finite differences of the polymorphous structure and applying the symmetries of the reference system, including both rotations and translations. Subsequent iterations involve the calculation of $C_{p\kappa\alpha,p'\kappa'\alpha'}(T)$, which is determined at each iteration by finite differences applied to a single thermally displaced configuration generated using Eq. (6). At each iterative step, the symmetry operations of the reference system are applied to $C_{p\kappa\alpha,p'\kappa'\alpha'}(T)$. Furthermore, to speed up convergence, linear mixing [42] between the IFCs is applied at each iteration.

After convergence is achieved, the final set of IFCs, is used to generate effective harmonic phonons to simulate lattice anharmonicity, and thus anharmonic ZG displacements via Eq. (6) which are applied on the polymorphous or reference structures. A DFT supercell calculation on the resulting thermally displaced structure enables the evaluation of a temperature-dependent charge density, opening the way for computing anharmonic electron-phonon properties [30]. For example, the ASDM can be used for computing anharmonic electron-phonon renormalized electron energies given by Eq. (2) using only a single configuration without relying on the explicit computation of the electron-phonon matrix elements entering Eq. (4). Another significant advantage of the ASDM is its ability to incorporate higher-order contributions to electron-phonon coupling without additional computational cost. Furthermore, it offers the flexibility to initiate calculations from different points on the PES, thereby being able to straightforwardly account for the influence of polymorphism on the electronic structure, without the use of molecular dynamics simulations.

III. METHODOLOGY AND MAIN RESULTS

A. Methodology

To compute electron-phonon renormalized quantities in locally disordered hybrid halide perovskites, we employ the ASDM as described in Sec. II D and Ref. [42], but now incorporating a separate treatment for the organic molecules. The methodology is outlined below:

(1) Compute the dynamically unstable harmonic phonons of the monomorphous structure.

(2) Construct a $2m \times 2n \times 2p$ supercell of the monomorphous structure, where m, n, p are integers $\geqslant 1$. Place the FA or MA molecules in different orientations, which can either be random or determined by a subgroup of the structure's space group. Choosing a subgroup allows to explore the effect of symmetries on the IFCs in step 5 below.

(3) Apply special displacements at temperature T [Eq. (6)] to the molecules and perform a geometry optimization with the atoms of the inorganic network and lattice constants fixed. The resulting geometry is the *reference structure* [Fig. 3(a)].

(4) Starting from the reference structure, apply special displacements at T [Eq. (6)] to the inorganic network and perform a full geometry optimization with the lattice constants fixed. The resulting geometry is the *polymorphous structure* (e.g., Fig. 1).

(5) Compute the IFCs of the polymorphous structure and enforce translational invariance with respect to a *fictitious reference structure* [Fig. 3(b)], so that if $\tau_{PK} = \tau_{p\kappa} + R_m$ and $\tau_{P'K'} = \tau_{p'\kappa'} + R_m$ then

$$\tilde{C}_{0\kappa\alpha,p'\kappa'\alpha'} = \frac{1}{N_p} \sum_m \tilde{C}_{PK\alpha,P'K'\alpha'}, \tag{10}$$

where τ_{PK} and $\tau_{p\kappa}$ represent atomic positions within the reference and fictitious structures, respectively, $\tilde{C}_{PK\alpha,P'K'\alpha'}$ are

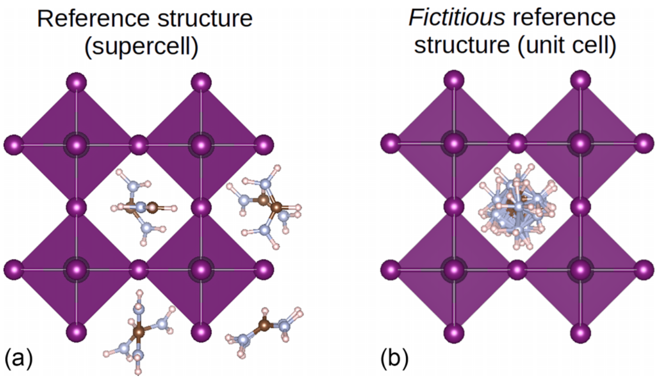

FIG. 3. (a) Example reference structure of FAPbI_3 with relaxed random molecular orientations in a $2\times2\times2$ sypercell. (b) Example fictitious reference structure of FAPbI_3 obtained by applying unit cell translations to the molecules in the reference structure, placing all back to a single unit cell. This fictitious structure serves as the reference point for calculating the interatomic force constants within the SCP theory.

the IFCs computed for the polymorphous structure, and N_p is the number of unit cells contained in the reference structure. The summation over m runs over N_p pairs of atoms in the reference structure connected by lattice translations R_m of the fictitious unit cell. Depending on the size of the supercell and the orientation of the molecules, if the reference system respects specific rotational symmetries (whether proper or improper), these symmetries should be applied to $\tilde{C}_{PK\alpha,P'K'\alpha'}$, as described in Ref. [42].

(6) Generate the effective dynamical matrix and obtain the phonons by diagonalization. Using the phonons, generate $\Delta\tau^{\text{ZG}}$ for T [Eq. (6)] and displace the nuclei of the reference structure. The resulting geometry is the *ZG reference structure*.

(7) Repeat steps 5 and 6 with linear mixing of the IFCs until self-consistency. For step 5, *use the ZG reference instead of the polymorphous structure*.

(8) Use the self-consistent phonons to generate a ZG $2M\times2N\times2P$ supercell by displacing atoms of the reference or polymorphous structures, where $M\geqslant m$, $N\geqslant n$, $P\geqslant p$, for computing electron-phonon properties. The resulting geometries are the *ZG reference structure* or *ZG polymorphous structure*.

(9) When configurational entropy is accounted for, i.e., multiple ZG reference or polymorphous structures are used to compute a property O, perform a Boltzmann-weighted average, defined as

$$\langle O\rangle_j = \frac{1}{Z}\sum_j e^{-F_j/k_{\text{B}}T} O_j, \qquad (11)$$

where $\langle . \rangle_j$ is a configurational average, F_j is the free energy of the structure j [Eq. (7)], and $Z=\sum_j e^{-F_j/k_{\text{B}}T}$ is the partition function. When no vibrational contributions are considered, the free energy is replaced by the DFT KS total energy.

The choice to first obtain a reference structure, i.e., relaxing the organic molecules before relaxing the entire halide perovskite system, rather than using the monomorphous structure, helps prevent artifacts arising from the net dipole moments of the molecules, particularly in the case of MA-based compounds. We note that for inorganic halide perovskites the reference structure is identical to the monomorphous structure. The generation of a reference structure in hybrid systems is also rationalized by the mostly distinct timescales and dynamics of the organic and inorganic components. The organic molecules exhibit, on majority, faster internal vibrations (energy scales >100 meV) and slower rotational and librational motions (energy scales $<$ 4 meV) compared to the inorganic lattice, whose phonon dynamics typically occur at intermediate energy scales of 4–35 meV [42]. Starting from random molecular orientations allows the molecules to explore their local potential energy landscape, where their dipoles adjust to the electrostatic environment created by the interplay with the fixed inorganic lattice. Relaxing the molecules first ensures that these slower rotational and librational modes settle into stable local minima without interference from the lattice dynamics. Additionally, it allows to mimic the effects of experimentally observed slow and stochastic molecular librational relaxations [23], which can not be deduced from the unstable lattice modes of the monomorphous structure using Eq. (6). In the subsequent step, the whole structure is relaxed together, enabling the inorganic lattice to adjust and couple with the pre-optimized molecular orientations. This two-step approach captures the polymorphous nature of the cubic phase, where local distortions and dynamic interactions between the organic and inorganic sublattices coexist, in a quasistatic manner. Additionally, it provides a reference structure that serves as a well-defined baseline for subsequent phonon quasiparticle calculations, such as those performed within the framework of the SCP theory.

Overall, we consider the following cases, as shown in Fig. 4:

(i) *monomorphous structures* that exhibit a ferroelectric arrangement of the molecules;

(ii) *reference structures* that account for correlated local disorder in the organic sublattice by relaxing molecules from random initial orientations;

(iii) maximally symmetrized supercells (MSS) that are used as reference structures which adopt specific space group symmetries, while remaining constrained by the supercell size;

(iv) *polymorphous structures* that account for correlated local disorder in both the organic and inorganic sublattices;

(v) *ZG reference structures* which incorporate thermal vibrations throughout the network, with static-equilibrium atomic positions of the reference structure;

(vi) *ZG polymorphous structures* which incorporate thermal vibrations throughout the network, with static-equilibrium atomic positions of the polymorphous structure.

B. Polymorphous structures, total energy lowering, and electronic structure correlations

We first apply steps 1–4 in the main methodology for generating 10 different reference and their corresponding polymorphous structures to account for configurational entropy effects in 12 materials. All calculations refer to $2\times2\times2$ supercells using the PBEsol functional; more computational details are available in Sec. VI. Figure 2(b) presents the

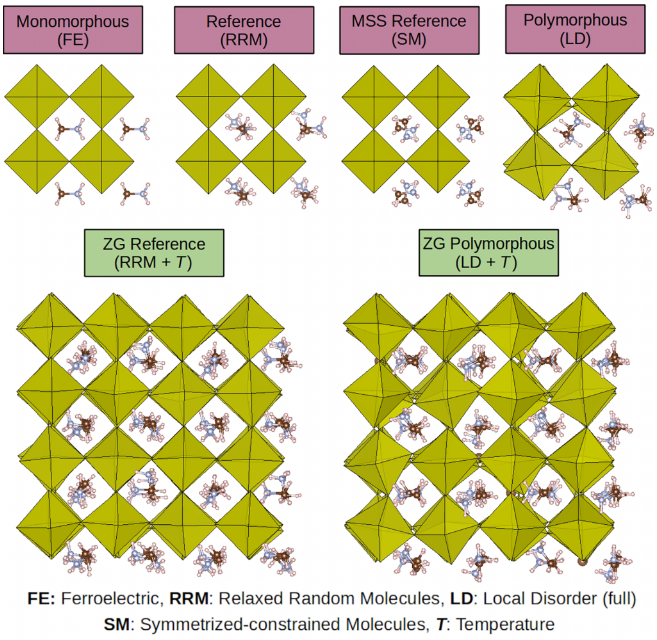

FIG. 4. Structures considered throughout this study using the example of $MAPbBr_3$. Reference structures can contain symmetrized-constrained or relaxed random molecular orientations. These structures lead to distinct polymorphous structures after geometry optimization. The ZG structures, labeled as green, incorporate electron-phonon coupling effects at finite temperatures (T). For the ZG structures, we considered a 4×4×4 supercell (768 atoms) to accommodate a broader sampling of vibrational modes.

Boltzmann-weighted average [Eq. (11)] of the total energy lowering (ΔU) calculated for the polymorphous structures relative to the reference structures, assuming a temperature $T = 300\,\mathrm{K}$. We note that testing different temperatures from 30 to 1000 K affects the values by no more than 4 meV per formula unit. On average, we find that the potential well depth, ΔU, is shallower in FA-based compounds compared to MA-based compounds, which in turn exhibit a shallower potential well than Cs-based compounds. The observed trend arises from differences in correlated local disorder in the inorganic network, where, FA-based compounds exhibit the least structural distortions, MA-based compounds show moderate disorder, and Cs-based compounds experience the highest degree of octahedral tilting and bond length fluctuations, leading to a deeper potential well. This behavior is mainly explained by the size of the A-site cation. Larger organic molecules, such as FA, create a more sterically constrained environment that limits structural flexibility, whereas smaller cations like MA and Cs permit greater lattice distortions and allow local disorder to emerge more readily. This trend is consistent with the tolerance factor [110,141–143], where lower values, associated with smaller A-site cations, favor increased positional polymorphism.

We quantify the degree of local disorder in the inorganic network by calculating the average B-X bond length ($\Delta l_{\mathrm{B-X}}$) and B-X-B bond angle variations ($\Delta\theta_{\mathrm{B-X-B}}$) relative to the idealized reference structures and demonstrate their correlations with the induced band gap increase (ΔE_g) and hole/electron effective mass enhancements ($\Delta m_h^*/\Delta m_e^*$), as shown in Figs. 2(c)–2(h). In all cases we obtain strong correlations indicated by the Pearson correlation, r, and R^2 coefficients, ranging from 0.84 to 0.96. Consistent with our findings on the potential well depth [Fig. 2(a)], the data categorize into three distinct groups. FA-based compounds, lying on the left side of the plot, exhibit $\Delta l_{\mathrm{B-X}}$ between 0.013–0.024 Å and $\Delta\theta_{\mathrm{B-X-B}}$ ranging from 8.2–13.0°. MA-based compounds, located in the middle, show $\Delta l_{\mathrm{B-X}}$ from 0.027–0.060 Å and $\Delta\theta_{\mathrm{B-X-B}}$ between 12.1–20.2°. On the right, Cs-based compounds display the largest structural deviations, with $\Delta l_{\mathrm{B-X}}$ spanning 0.057–0.085 Å and $\Delta\theta_{\mathrm{B-X-B}}$ ranging from 21.1–26.5°. Notably, MA-based compounds cover the widest range of structural variations, which we attribute to the larger dipole moments of the MA cations that can significantly influence the electronic structure [36,144].

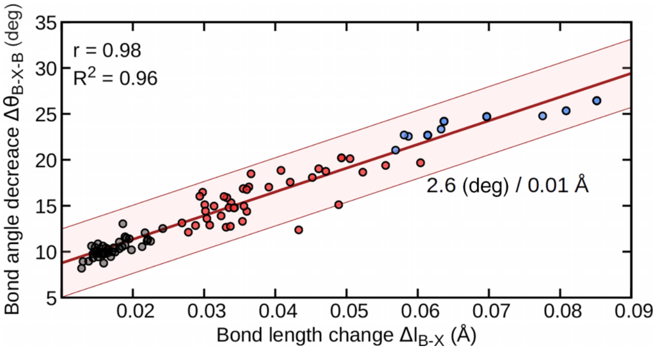

FIG. 5. Dependence of the average B-X-B bond angle decrease on the average B-X bond length variation. The 120 data points correspond to 10 polymorphous configurations generated for 4 FA (black), 4 MA (red), and 4 Cs (blue)-based compounds. The straight thick line represents the least-squares regression fit to the data, with the slope indicated on the plot. The shaded region represents three standard deviations on either side of the lines.

In view of Figs. 2(c)–2(h), it is clear that both bond length and bond angle variations correlate closely with the band gap and effective mass enhancements, indicating that these structural distortions are mutually related. Indeed, Fig. 5 shows an almost perfect correlation ($r = 0.98$) between the two distortion measures, suggesting that only one of these two features is sufficient to explain changes in the electronic properties induced by local disorder.

The strong correlation between local disorder and electronic properties arises from orbital hybridization effects, where distortions in B-X-B angles modify the degree of overlap between the B-site cation and X-site halide orbitals [3]. In the ideal cubic reference structure, the B-X-B connectivity facilitates strong metal-halide sp-p hybridization, leading to smaller band gaps, highly dispersive electronic bands with very low effective masses. However, when local disorder is present, such as octahedral tilting and bond-length fluctuations, the overlap between B-p/s orbitals and X-p orbitals is reduced, decreasing the bandwidth and thus increasing both the band gap and effective masses [110]. The stereochemical activity of the ns^2 lone pair emerges as a consequence of this disorder, with symmetry-breaking distortions inducing an asymmetrical electron density around the B-site metal, which is more prominent in Sn-based compounds [27,33].

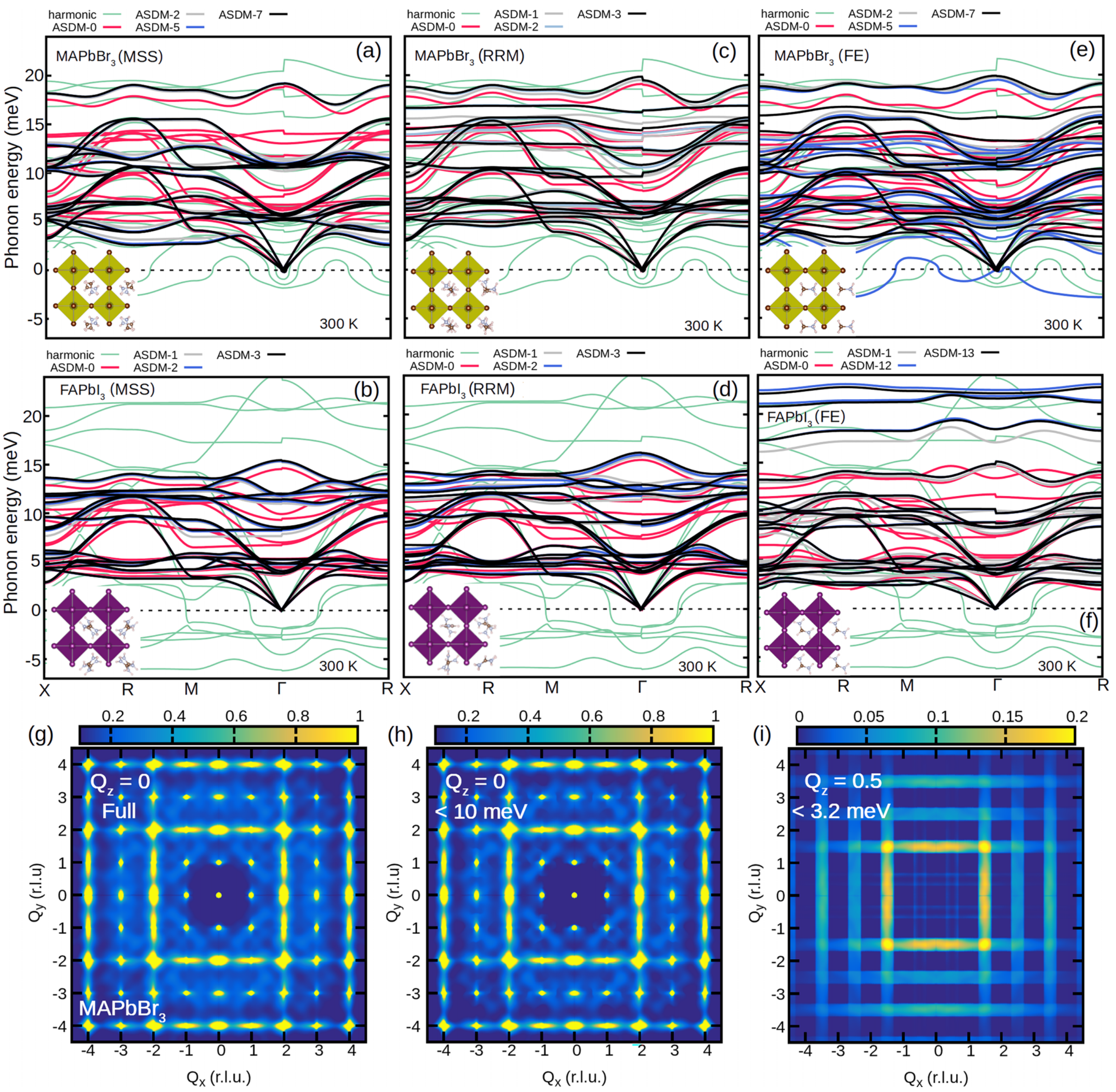

FIG. 6. (a)–(f) Convergence of the ASDM anharmonic phonon dispersions at 300 K calculated for MAPbBr$_3$ and FAPbI$_3$ using 2×2×2 supercells and the PBEsol approximation. In panels (a) and (b), we use maximally symmetrized structures (MSS) with space group P422 as the reference. In panels (c) and (d), we use reference structures with relaxed random molecular (RRM) orientations. In panels (e) and (f), the molecules adopt a single ferroelectric (FE) orientation. The structures are displayed in the bottom left corner of each plot. The green and red curves represent harmonic phonon dispersions calculated for the monomorphous and polymorphous (ASDM-0) structures, respectively. Subsequent ASDM-*i* steps, where *i* represents an integer index for the iteration, are shown as gray and blue. The converged ASDM phonon dispersion is shown as black. (g), (h) One-phonon diffuse scattering intensity of MAPbBr$_3$ at 300 K calculated for $[Q_x Q_y 0]$ plane using phonons across the full energy range (g) and phonons with energies below 10 meV (h). (f) One-phonon diffuse scattering intensity of MAPbBr$_3$ at 300 K calculated for $[Q_x Q_y 0.5]$ plane using phonons with energies below 3.2 meV. The components of the scattering wave vectors are given in reciprocal lattice units (r.l.u.) of the minimal cubic unit-cell.

C. Phonon anharmonicity and diffuse scattering

Figures 6(a)–6(f) show the convergence of the phonon dispersion of MAPbBr$_3$ and FAPbI$_3$ calculated for three different reference structures using the ASDM through the steps 1-7 in the main methodology (Sec. III A). All ASDM calculations are for 2×2×2 supercells. In all plots, we focus in the energy range 0–25 meV related mostly to lattice vibrations of the inorganic network; high energy flat phonon bands representing molecular vibrations are not shown for clarity. In Sec. VI, we further show the percentage contribution of molecular vibrations in the energy range 0–25 meV. In all plots, we also include the phonon dispersion of the monomorphous structure calculated within the harmonic approximation (green curve), which reveals instabilities across the reciprocal space.

In Figs. 6(a) and 6(b), we present symmetrized anharmonic phonon dispersions, obtained by arranging the MA or FA molecules in the reference structure to respect specific space group symmetries, while remaining constrained by the supercell size, i.e., the MSS structure. The symmetrized reference structure is constructed such that the molecules are positioned to preserve 8 symmetries of the $Pm\bar{3}m$ (No. 221) space group. Those eight symmetries represent the tetragonal subgroup P422 (No. 89) which is a subgroup of $Pm\bar{3}m$. All ASDM steps, yield stable anharmonic phonons across the entire reciprocal space, with reasonable convergence achieved as early as the second iteration (ASDM-2) for both $MAPbBr_3$ and $FAPbI_3$. Notably, the symmetrized phonons calculated for the polymorphous structure (ASDM-0) successfully capture the key features of the converged anharmonic phonon dispersion. However, the ASDM-0 fail to capture the low-frequency flat band of $MAPbBr_3$ along the R-M path, which undergoes a significant softening upon inclusion of phonon self-energy corrections, reaching a minimum energy as low as 2.5 meV [Fig. 6(a)]. This branch is the most sensitive feature of the phonon dispersion due to the ultraslow dynamical hopping of the system between different minima in the PES which cannot be captured by the quasistatic polymorphous framework. As shown below, the starting orientation of the molecules in the reference structure can impact profoundly these low energy phonons.

In Figs. 6(c) and 6(d), we present the ASDM convergence performance when starting random orientations of the molecules are chosen, effectively eliminating all rotational symmetries in the $MAPbBr_3$ and $FAPbI_3$ reference structures. We readily observe that all ASDM iterations produce dynamically stable phonons, with the translationally symmetrized phonons for the polymorphous structure at ASDM-0 closely approximating those obtained from the fully converged phonon dispersion at ASDM-3. In contrast to the results shown in Figs. 6(a) and 6(b), where certain rotational symmetries are preserved in the MSS structure, the phonon dispersion shown in Figs. 6(c) and 6(d) reveals degeneracy splittings. This confirms that the molecular orientations influence the lattice vibrations of the inorganic network.

As shown in Figs. 6(e) and 6(f), the effect of molecular orientation on the phonon dispersion becomes even more pronounced when the reference structure corresponds to the monomorphous structure, characterized by a single ferroelectric orientation of the MA or FA molecules. Unlike the symmetric and random reference structures of $MAPbBr_3$, the ASDM procedure fails to achieve convergence in the ferroelectric case, exhibiting persistent phonon instabilities [Fig. 6(e)], indicated by negative phonon energies, at various iterations (e.g., ASDM-5). Notably, as the ASDM procedure progresses, certain flat phonon bands associated with the orientations of the organic molecules become imaginary (not shown), highlighting the inherent instability of the ferroelectric MA-based configurations. The phonon instabilities observed in the ferroelectric orientation arise because the MA molecule's intrinsic dipole conflicts with the lattice's tendency to minimize electrostatic energy and maintain mechanical stability. The phonon instabilities also suggest that MA-based hybrid halide perovskites do not support a stable ferroelectric state for the molecules, favoring alternative configurations (i.e., antiferroelectric or random molecular orientations) that better accommodate the coupling between the lattice dynamics of the organic and inorganic framework. Our results for ferroelectric $FAPbI_3$ up to ASDM-13 indicate that a ferroelectric fluctuation of the molecules may be dynamically stable in FA-based compounds. This stability is likely due to the minimal net dipole moment of the FA molecule, which reduces internal electric fields that could destabilize the ferroelectric phase. This result is also consistent with studies on solution-processed $FAPbI_3$ layers, suggesting that substituting MA with FA cations enhances lattice robustness and contribute to material durability [145]. In Sec. VI, we show that the phonon modes with energies above 15 meV are primarily associated with vibrations of the organic sublattice, demonstrating that the ferroelectric state leads to further decoupling between the vibrational dynamics of the inorganic and organic sublattices.

To validate our approach for calculating the phonon dispersions of hybrid halide perovskites we report diffuse scattering maps of $MAPbBr_3$ at 300 K. In Fig. 6(g), we show the phonon-induced diffuse scattering map of $MAPbBr_3$ calculated for the $[Q_xQ_y0]$ plane, where Q_α represent Cartesian components of the scattering wave vector $\mathbf{Q}$. The scattering map is computed using the phonons calculated for the MSS structure [Fig. 6(a)], neglecting multi-phonon contributions [146]. Our computed scattering map exhibits excellent qualitative agreement with the experimental maps reported in Ref. [35], reproducing all main features, including the vertical and horizontal diffuse scattering rods that connect high intensity Bragg peaks, formed when Q_x and Q_y are integers. In Fig. 6(h), we present the phonon-induced diffuse scattering map of $MAPbBr_3$ in the same plane, considering now only phonons with energies below 10 meV. A comparison of the maps in Figs. 6(g) and 6(h) clearly reveals that all major features are reproduced, demonstrating that low-energy phonons dominate diffuse scattering in $MAPbBr_3$. In Fig. 6(i), we show the phonon-induced scattering map of $MAPbBr_3$ calculated for the $[Q_xQ_y0.5]$ plane, focusing now on ultralow energy phonons with energies below 3.2 meV driving dynamical octahedral tilting and hopping between different minima in the PES. These structural fluctuations are primarily associated with the low-energy flat phonon band along the R-M path in Fig. 6(a) and give rise to diffuse scattering rods connecting equivalent wave vectors at the M and R points, consistent with calculations for the high-symmetry cubic phase of $CsPbBr_3$ [30,147]. We note that we exclude any quasielastic contributions to diffuse scattering arising from polymorphism in the inorganic sublattice, as this is beyond the scope of the present work. However, in Sec. V D, we examine the influence of local disorder on phonons, leading to strongly overdamped vibrational dynamics.

D. Free energies, temperature-dependent band gaps, and effective masses

We remark that the 10 polymorphous structures explored for each cubic hybrid halide perovskite in 2×2×2 supercells yield distinct DFT total energy lowerings and phonon spectra.

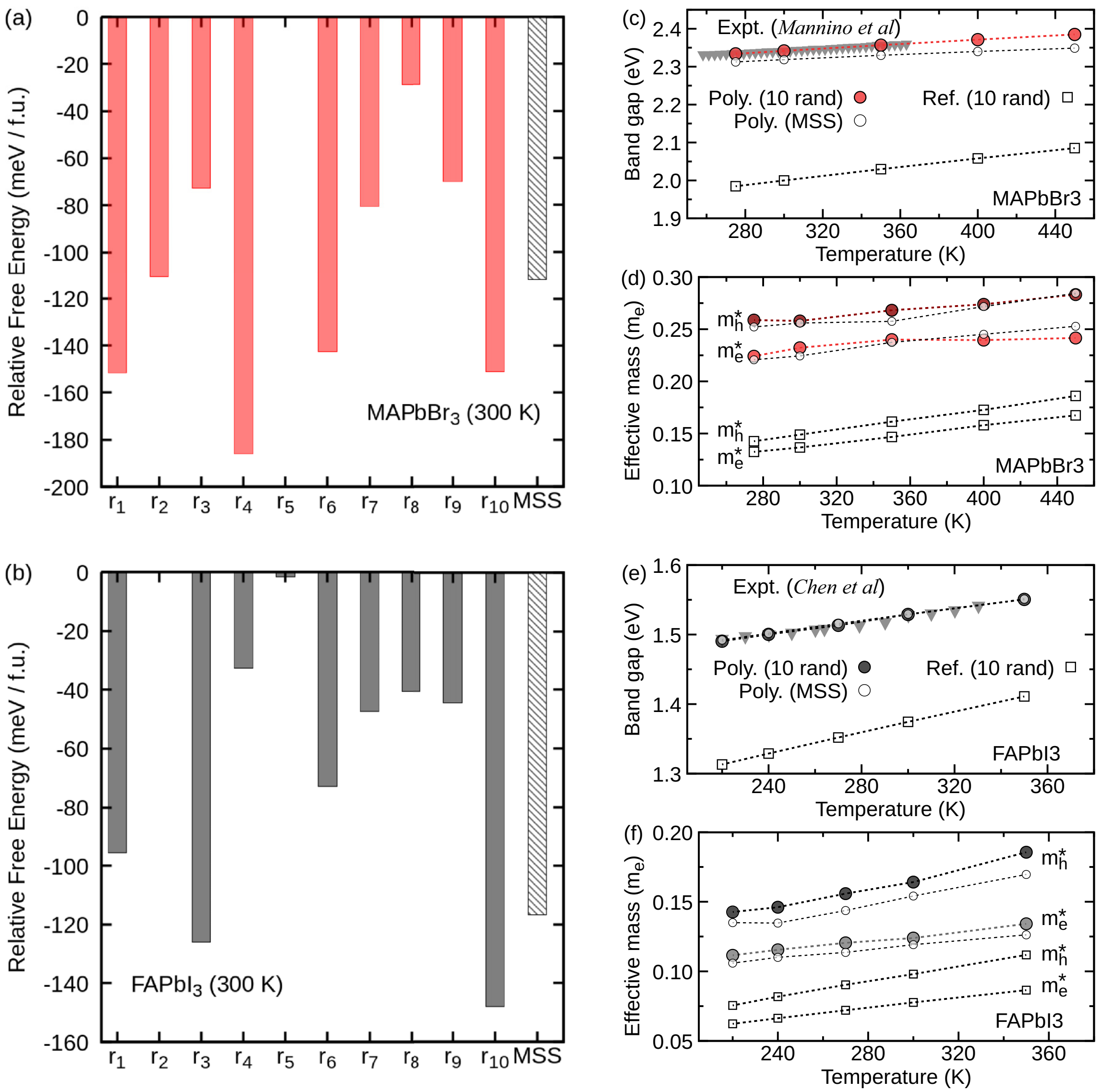

FIG. 7. (a), (b) Relative free energy at 300 K for 10 ZG polymorphous configurations (r_1-r_{10}) of cubic MAPbBr$_3$ (a) and FAPbBr$_3$ (b), referenced to the least stable configuration, calculated using Eq. (8) and 2×2×2 supercells. The ZG polymorphous configurations are obtained starting from geometry optimization of the reference structures with random molecular orientations and then through ASDM. ASDM converged phonons calculated for each structure [e.g., black lines in Figs. 6(c) and 6(d)] are used to compute the free energy. The relative free energy of the ZG polymorphous configuration starting from the maximally symmetrized supercell (MSS) is shown for comparison. (c)–(f) Band gaps and electron/hole effective masses ($m^*_\mathrm{e}/m^*_\mathrm{h}$) calculated for MAPbBr$_3$ and FAPbI$_3$ using ZG polymorphous (filled discs) and ZG reference (open squares) configurations in 4×4×4 supercells accounting for both electron-phonon coupling and thermal lattice expansion. The effect of spin-orbit coupling is also included. Boltzmann-weighted averages [Eq. (11)] are obtained for 10 structures. Open circles represent calculations using the ZG polymorphous configuration of the MSS. All calculated temperature-dependent band gaps are shifted by 1.44 and 1.10 eV to match experimental data of MAPbBr$_3$ and FAPbI$_3$ at 300 K, respectively. These corrections are consistent with the PBE0 values for the band gaps reported in Table I. Experimental gaps (gray triangles) are from Refs. [56] and [58].

These variations arise from the sensitivity of local disorder to molecular orientations as discussed previously. To account for the influence of local disorder, configurational entropy, and thermal effects on the electronic structure across various ZG polymorphous configurations, we compute the free energy of each configuration and use it to obtain Boltzmann-weighted averages [Eq. (11)]. Figures 7(a)–7(f) show calculations for the relative free energies of each ZG polymorphous configuration and Boltzmann averaged band gaps and effective masses of cubic MAPbBr$_3$ and FAPbI$_3$. The free energies in Figs. 7(a) and 7(b) are evaluated with respect to the least stable configurations, r_2 and r_5. We also include the relative free energy calculated for the ZG polymorphous configuration obtained by combining the ASDM with geometry optimization for the MSS structure. Although starting from the MSS structure yields one of the most stable configurations, it does not lead to the absolute minimum in stability. Other random molecular orientations facilitate local disorder within 2×2×2 supercells more effectively, leading to lower energy ZG polymorphous structures.

TABLE I. Lattice constants (L), DFT band gaps (E_g), PBE0 band gaps ($E_\mathrm{g}^\mathrm{PBE0}$), DFT hole ($m_\mathrm{h}^*$), and electron ($m_\mathrm{e}^*$) effective masses, and reduced effective masses (μ) of the reference (r) and polymorphous (p) structures of inorganic and hybrid halide perovskites. Band gaps and effective masses are calculated using 2×2×2 supercells (40 and 96 atoms), 3×3×3 uniform **k** grids, and a plane wave cutoff of 120 Ry, including the effect of spin-orbit coupling. DFT corrections to the band gaps [$\Delta E_\mathrm{g}(T)$] and effective masses [$\Delta m_\mathrm{h}^*(T)$] due to electron-phonon coupling and thermal expansion at temperatures T are calculated with the ASDM using 4×4×4 ZG supercells (320 and 768 atoms), 1×1×1 uniform **k** grids, and a plane wave cutoff of 60 Ry, including the effect of spin-orbit coupling. Values were obtained as averages over 10 distinct configurations of the reference and polymorphous structures. Experimental band gaps of the cubic phases, $E_\mathrm{g}^\mathrm{expt.}$, and experimental reduced effective masses of the low-temperature phases ($\mu^\mathrm{expt.}$) are reported for comparison. Δ_s represents an empirical correction to the calculated band gaps to match $E_\mathrm{g}^\mathrm{expt.}$, which is consistent with the PBE0 correction $E_\mathrm{g}^\mathrm{PBE0} - E_\mathrm{g}$.

	L Å	E_g (eV)	$E_\mathrm{g}^\mathrm{PBE0}$ (eV)	$\Delta E_\mathrm{g}(T)$ (eV)	$E_\mathrm{g}^\mathrm{expt.}$ (eV)	Δ_s (eV)	m_h^* (m_0)	$\Delta m_\mathrm{h}^*(T)$ (m_0)	m_e^* (m_0)	$\Delta m_\mathrm{e}^*(T)$ (m_0)	μ (m_0)	$\mu^\mathrm{expt.}$ (m_0)
r-CsPbI$_3$	6.25	−0.05	1.15	0.39 (650 K)	–	1.02	−0.02	–	−0.02	0.22 (650 K)	−0.010	–
p-CsPbI$_3$	6.25	0.60	1.84	0.13 (650 K)	1.78[a]	1.02	0.21	0.16 (650 K)	0.17	0.08 (650 K)	0.094	0.114 ± 0.01[k]
r-CsPbBr$_3$	5.87	0.24	1.52	0.41 (430 K)	–	1.38	0.04	0.17 (430 K)	0.04	0.14 (430 K)	0.020	–
p-CsPbBr$_3$	5.87	0.85	2.30	0.16 (430 K)	2.39[b]	1.38	0.23	0.11 (430 K)	0.23	0.10 (430 K)	0.115	0.126 ± 0.01[k]
r-CsSnI$_3$	6.14	−0.27	0.67	0.52 (500 K)	–	0.86	−0.07	0.20 (500 K)	−0.10	0.18 (500 K)	−0.041	–
p-CsSnI$_3$	6.14	0.28	1.30	0.20 (500 K)	1.35[c]	0.86	0.07	0.05 (500 K)	0.09	0.08 (500 K)	0.039	–
r-CsPbCl$_3$	5.60	0.59	2.16	0.33 (330 K)	–	1.77	0.12	0.16 (330 K)	0.13	0.14 (330 K)	0.062	–
p-CsPbCl$_3$	5.60	1.19	2.79	0.10 (330 K)	3.02[d]	1.77	0.29	0.07 (330 K)	0.31	0.08 (330 K)	0.150	0.202 ± 0.01[l]
r-MAPbI$_3$	6.31	0.03	1.23	0.26 (315 K)	–	1.00	0.02	0.09 (315 K)	0.02	0.07 (315 K)	0.010	–
p-MAPbI$_3$	6.31	0.52	1.75	0.09 (315 K)	1.61[e]	1.00	0.16	0.06 (315 K)	0.13	0.04 (315 K)	0.072	0.104[m]
r-MAPbBr$_3$	5.97	0.39	1.82	0.17 (300 K)	–	1.44	0.09	0.06 (300 K)	0.09	0.05 (300 K)	0.045	–
p-MAPbBr$_3$	5.97	0.83	2.27	0.08 (300 K)	2.34[b]	1.44	0.19	0.07 (300 K)	0.18	0.05 (300 K)	0.092	0.106[n], 0.117[m]
r-MASnI$_3$	6.23	−0.09	0.88	0.22 (300 K)	–	1.02	-0.05	0.09 (300 K)	−0.03	0.09 (300 K)	−0.019	–
p-MASnI$_3$	6.23	0.28	1.30	0.13 (300 K)	1.31[f]	1.02	0.06	0.03 (300 K)	0.09	0.04 (300 K)	0.036	–
r-MAPbCl$_3$	5.68	0.72	2.34	0.13 (300 K)	–	1.73	0.15	0.05 (300 K)	0.16	0.04 (300 K)	0.077	–
p-MAPbCl$_3$	5.68	1.24	2.88	0.12 (300 K)	3.07[g]	1.73	0.26	0.08 (300 K)	0.27	0.08 (300 K)	0.132	–
r-FAPbI$_3$	6.36	0.10	1.33	0.18 (300 K)	–	1.10	0.03	0.07 (300 K)	0.03	0.05 (300 K)	0.015	–
p-FAPbI$_3$	6.36	0.34	1.59	0.09 (300 K)	1.53[h]	1.10	0.10	0.06 (300 K)	0.09	0.04 (300 K)	0.047	0.09, 0.095[m]
r-FAPbBr$_3$	5.99	0.46	1.89	0.13 (300 K)	–	1.50	0.10	0.04 (300 K)	0.10	0.03 (300 K)	0.050	–
p-FAPbBr$_3$	5.99	0.70	2.13	0.10 (300 K)	2.29[b]	1.50	0.16	0.05 (300 K)	0.15	0.04 (300 K)	0.077	0.115, 0.13[m]
r-FASnI$_3$	6.33	0.11	1.13	0.18 (300 K)	–	0.85	0.03	0.04 (300 K)	0.03	0.05 (300 K)	0.015	–
p-FASnI$_3$	6.33	0.42	1.48	0.08 (300 K)	1.38[i]	0.85	0.08	0.03 (300 K)	0.11	0.04 (300 K)	0.046	–
r-FAPbCl$_3$	5.74	0.89	2.51	0.09 (300 K)	–	1.71	0.17	0.04 (300 K)	0.18	0.04 (300 K)	0.087	–
p-FAPbCl$_3$	5.74	1.17	2.79	0.03 (300 K)	2.91[j]	1.71	0.23	0.05 (300 K)	0.25	0.05 (300 K)	0.120	–

[a]Ref. [44]; [b]Ref. [56]; [c]Ref. [54]; [d]Ref. [59]; [e]Ref. [52]; [f]Ref. [61]; [g]Ref. [55]; [h]Ref. [58]; [i]Ref. [57]; [j]Ref. [111]; [k]Ref. [152]; [l]Ref. [153]; [m]Ref. [154]; [n]Ref. [81].

In Figs. 7(c) and 7(e), we compare our calculated temperature-dependent band gaps using ZG polymorphous (filled discs) and ZG reference (open squares) structures of cubic MAPbBr$_3$ and FAPbI$_3$ with experimental data from Refs. [56,58]. Accounting for local disorder in our calculations significantly improves agreement with experiment. This improvement arises from two key effects: (i) positional polymorphism influences the electronic structure, leading to a substantial band gap increase of 0.44 eV for MAPbBr$_3$ and 0.24 eV for FAPbI$_3$ relative to the reference structures (see Table I), and (ii) it reduces the temperature coefficient of the band gap, quantified by a decrease in dE_g/dT of 51% for MAPbBr$_3$ and 62% for FAPbI$_3$. A quantitative comparison of dE_g/dT extracted from experiments and calculations, along with the respective contributions of electron-phonon coupling and thermal lattice expansion, is presented in Sec. IV. Importantly, we demonstrate in Figs. 7(c)–7(f) that a single ZG polymorphous configuration obtained from the MSS structure can yield accurate results for MAPbBr$_3$ and FAPbI$_3$, comparable to those obtained using 10 ZG polymorphous configurations.

In Figs. 7(d) and 7(f), we present the temperature dependence of the hole and electron effective masses in cubic MAPbBr$_3$ and FAPbI$_3$, exhibiting a linear relationship with temperature. Compared to calculations for the reference structures, the effective masses obtained using ZG polymorphous configurations are almost twice as large. In fact, for the ZG reference structure of cubic MAPbBr$_3$ we obtain $m^*_\mathrm{h,ref} = 0.15$, $m^*_\mathrm{e,ref} = 0.14$, and a reduced effective masses of $\mu_\mathrm{ref} = 0.07$ at $T = 300\,\mathrm{K}$ in units of the free electron mass m_0. In contrast, for the ZG polymorphous structure of cubic MAPbBr$_3$, these values increase substantially to $m^*_\mathrm{h,poly} = 0.26$, $m^*_\mathrm{e,poly} = 0.23$, and $\mu_\mathrm{poly} = 0.12$ at the same temperature. The corresponding values at $T = 300\,\mathrm{K}$ for cubic FAPbI$_3$ are $m^*_\mathrm{h,ref} = 0.10$, $m^*_\mathrm{e,ref} = 0.08$, $\mu_\mathrm{ref} = 0.04$, $m^*_\mathrm{h,poly} = 0.16$, $m^*_\mathrm{e,poly} = 0.13$, and $\mu_\mathrm{poly} = 0.07$. We note that our calculations are at the DFT-level and can be further improved by considering quasiparticle corrections within the *GW* approximation, which are known to enhance the effective masses [95,99–101,106,148–151] In Sec. IV, we provide a more detailed discussion how the reduced effective masses of poly-

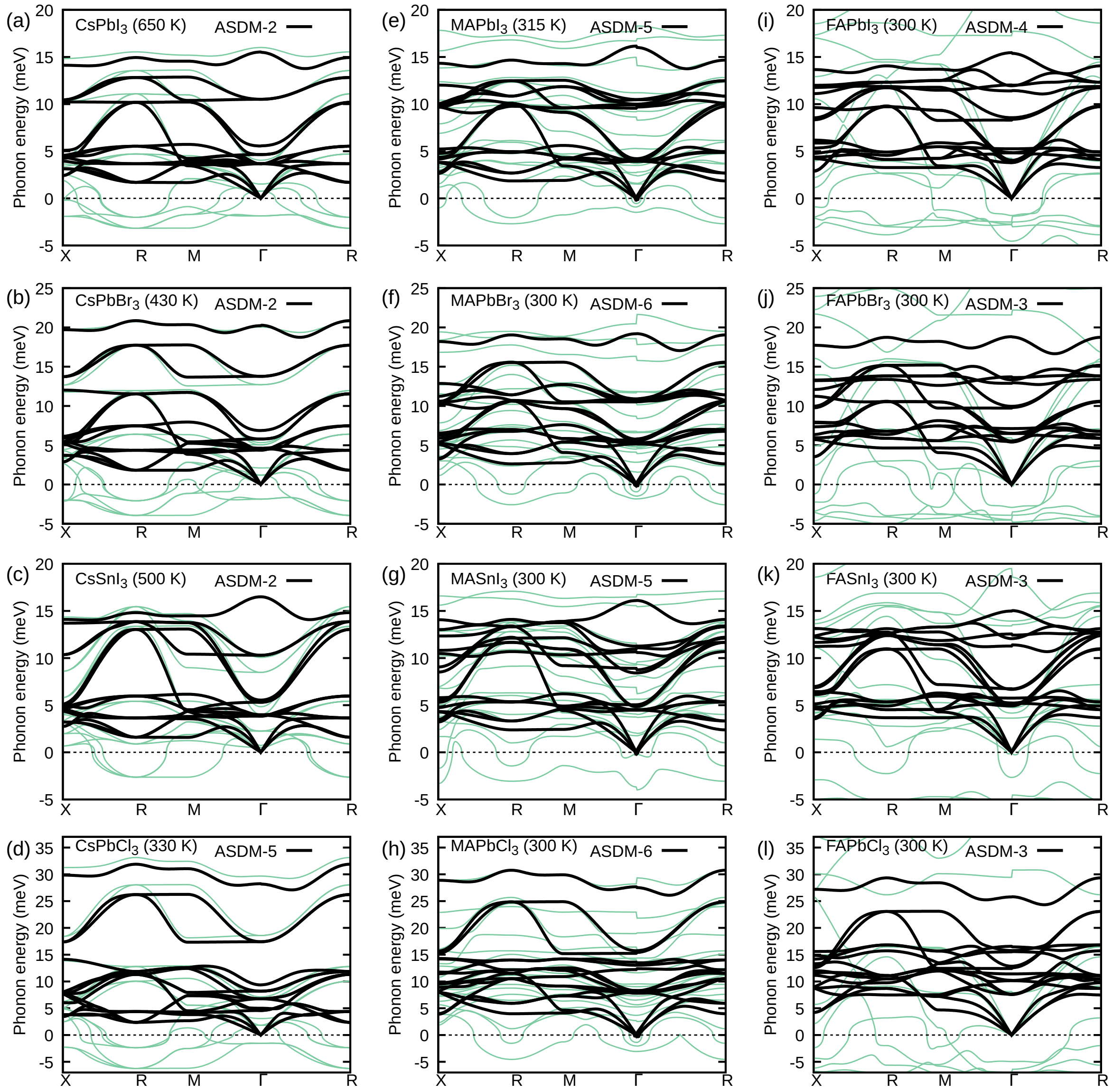

FIG. 8. Anharmonic phonon dispersions at finite temperatures (black curves) calculated for the cubic phases of each material with the ASDM. On each plot we indicate the ASDM-*i* iteration for which convergence is achieved. The green curve represents the harmonic phonon dispersion obtained for the monomorphous structure. All phonon dispersions include long-range dipole-dipole interaction corrections, leading to LO-TO splitting.

morphous structures compare to experimental measurements and *GW* calculations.

IV. CASE-BY-CASE ANALYSIS OF 12 MATERIALS

In this section, we discuss our results for each cubic halide perovskite considered in this study: $CsPbI_3$, $CsPbBr_3$, $CsSnI_3$, $CsPbCl_3$, $MAPbI_3$, $MAPbBr_3$, $MASnI_3$, $MAPbCl_3$, $FAPbI_3$, $FAPbBr_3$, $FASnI_3$, and $FAPbCl_3$. We follow this specific order to maintain consistency with the companion paper [110], which focuses on $APbI_3$, $APbBr_3$, and $ASnI_3$. In this work, we provide further analysis and results on these systems and also include findings for Cl-based compounds. We present first-principles calculations of the band gaps and effective masses at the DFT level for both reference and polymorphous structures (Table I). For the band gaps, we additionally report results obtained using the PBE0 hybrid functional [155], which has been found to reliably describe the band gaps of three-dimensional halide perovskites [30,156]. All reported effective masses and reduced effective masses are in units of the free electron mass m_0. Temperature-dependent anharmonic phonon dispersions are shown in Fig. 8. TO and LO phonon frequencies are reported in Table II, which are compared against experimental results from various techniques. Furthermore, in Fig. 9, we report temperature-dependent band gaps and effective masses computed using the ASDM. A comparative analysis between the reference and polymorphous structures is provided in Table I as well as in Figs. 9 and 10, highlighting the impact of local disorder on electron-phonon coupling and thermal lattice expansion contributions to band gap renormalization. In Sec. V D, we also investigate the influence of positional polymorphism on vibrational dynamics through calculations of phonon spectral functions, shown in Fig. 11. We validate our computational methodol-

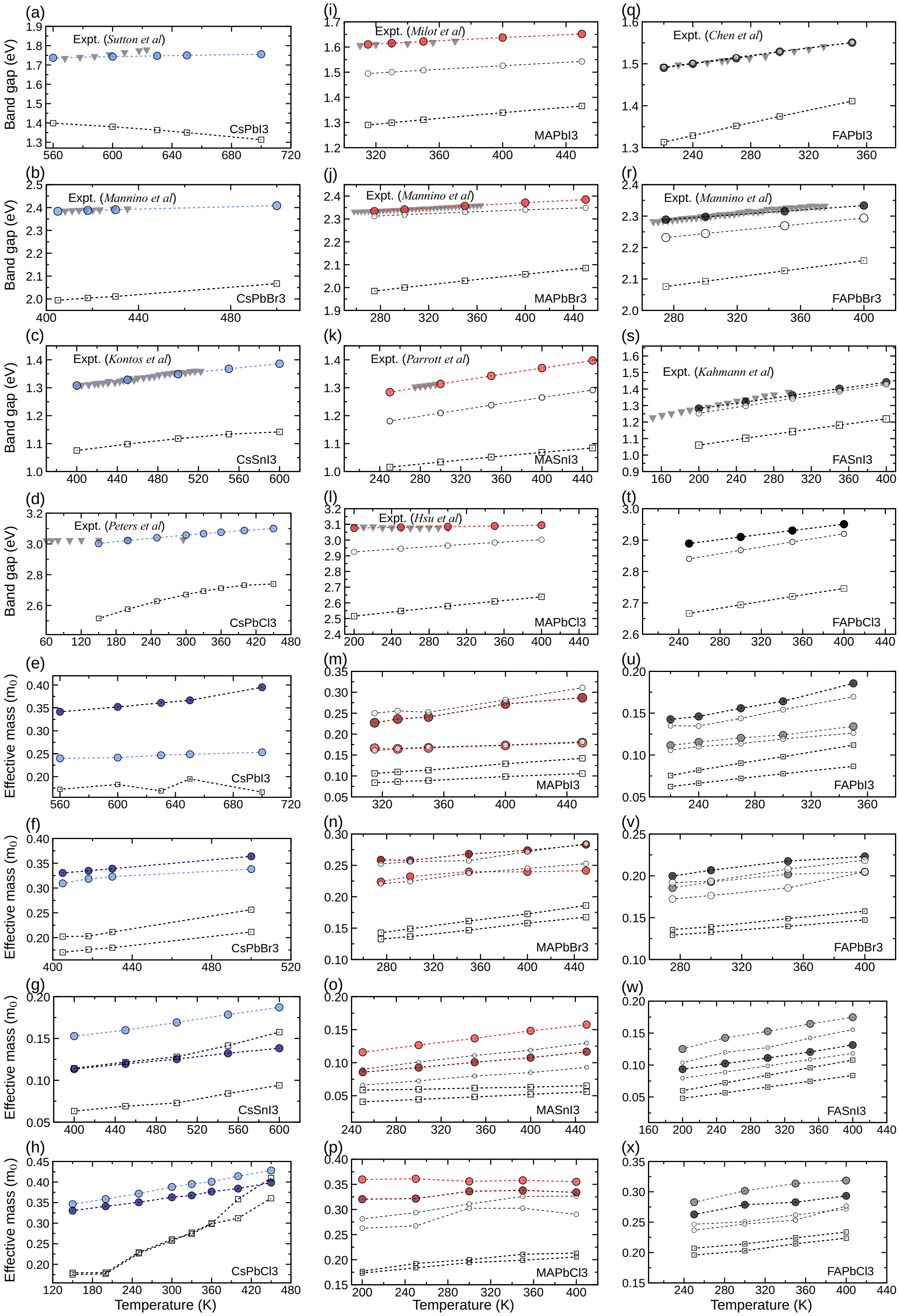

FIG. 9. Temperature-dependent band gaps and carrier effective masses calculated with the ASDM and Boltzmann averages [Eq. (11)] over 10 ZG polymorphous (coloured) and 10 ZG reference (open squares) structures. For hybrid compounds, we show the result using one ZG polymorphous configuration derived from the MSS structure (open circles). Experimental band gaps (gray triangles) are from Refs. [44,52,54–59,61,111]. Dark blue, dark red, and black in panels (e)–(h), (m)–(p), and (u)–(x) indicate the hole effective masses. Light blue, light red, and gray in panels (e)–(h), (m)–(p), and (u)–(x) indicate the electron effective masses.

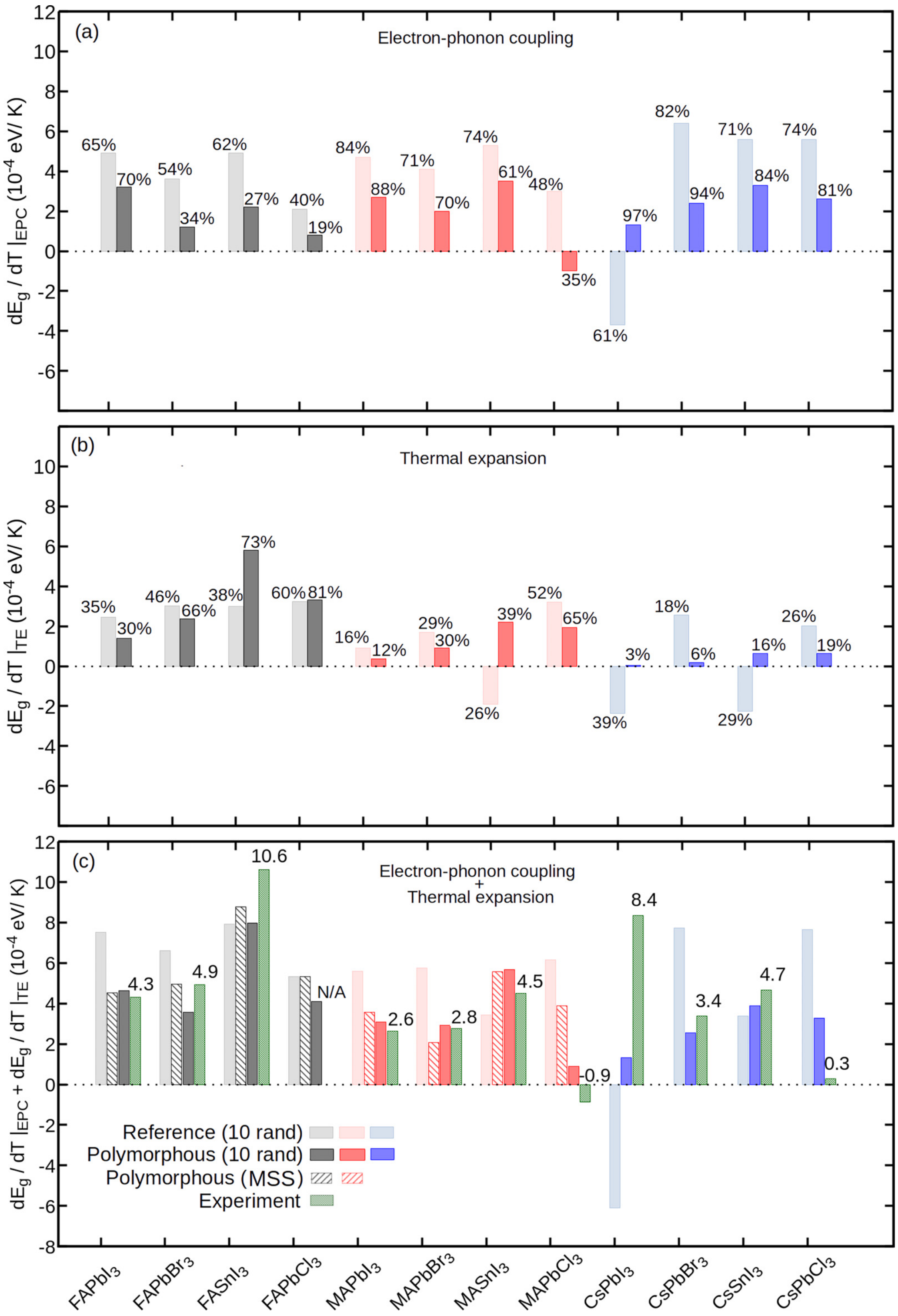

FIG. 10. (a)–(c) Contributions of electron-phonon coupling $dE_g/dT|_{\mathrm{EPC}}$ (a) and thermal lattice expansion $dE_g/dT|_{\mathrm{TE}}$ (b) to the total temperature coefficient of the band gap dE_g/dT (c). The total dE_g/dT values correspond to slopes obtained from linear fits to the calculated band gaps shown in Fig. 9. Light red, light blue, and light gray bars represent average data obtained for 10 ZG reference structures. Red, blue, and gray bars represent average data obtained for 10 ZG polymorphous structures. In panel (c), we also include data obtained for a single ZG polymorphous configuration of the MSS structure (patterned bar). Experimental data (green bars) are extracted by linear fits to the measurements [44,52,54–59,61,111] reported in Fig. 9. The percentages in panels (a) and (b) indicate the contributions of $dE_g/dT|_{\mathrm{EPC}}$ and $dE_g/dT|_{\mathrm{TE}}$ to their total. In panel (c), the numbers indicate the experimental values in units of 10^{-4} eV/K.

TABLE II. Optical phonon energies (in meV) at the Γ point. In parenthesis, we give values of the LO phonons before LO-TO splitting. For Cs-based compounds, ω_{TO_2} is a silent triply degenerate mode, and the other TO modes are infrared-active and doubly degenerate. Experimental data on single crystals (SCs), polycrystalline pellets (PCPs), thin films (TFs), nanocrystals (NCs), and NC films (NCFs) with temperatures are reported. Experiments refer to the following spectroscopy and scattering techniques: Photoluminescence (PL), THz Kerr, Raman, infrared (IR), inelastic neutron scattering (INS), and terahertz time-domain spectroscopy (THz-TDS). The temperature range used for fitting the PL linewidth (LW) is also indicated.

	ω_{TO_1}	ω_{TO_2}	ω_{TO_3}	ω_{TO_4}	ω_{TO_5}	ω_{TO_6}	ω_{TO_7}	ω_{TO_8}	ω_{LO_1}	ω_{LO_2}	ω_{LO_3}	ω_{LO_4}
$CsPbI_3$, 650 K	3.68	3.72	4.7	10.7	–	–	–	–	3.71 (3.68)	5.6 (4.7)	15.6 (10.7)	–
THz-TDS, NCF, 300 K [157]	4.1	5.9	8.8	11.2	–	–	–	–	4.8	6.9	9.3	15.2
PL replica, NC, 3 K [158]									3.3	5.3		
$CsPbBr_3$, 430 K	4.4	4.6	5.8	13.8	–	–	–	–	4.5 (4.4)	6.9 (5.8)	20.3 (13.8)	–
THz Kerr, SC, 80 K [160]	3.7		5.4									
PL LW, NC, 15–295 K [161]											20.0	
PL LW, SC, 10–295 K [162]											16.0	
THz-TDS, PCP, 300 K [168]											18.9	
$CsSnI_3$, 500 K	3.9	4.0	5.3	10.3	–	–	–	–	4.0 (3.9)	5.6 (5.3)	16.5 (10.3)	–
$CsPbCl_3$, 330 K	4.6	6.8	8.2	17.4	–	–	–	–	5.0 (4.6)	9.4 (8.2)	28.2 (17.4)	–
PL LW, SC, 185–295 K [162]									4.3			
Raman, NC, 170 & 2 K [165]	3.1	6.0	8.4	9.8	13.5	14.5				14.2	25.0	
$MAPbI_3$, 315 K	3.9	3.94	3.94	4.0	9.6	9.98	10.0	10.4	3.93 (3.9)	4.2 (3.94)	10.4 (10.0)	16.2 (10.4)
IR, TF/SC, 300 K [166]		4.0				7.8			5.0			16.5
IR, SC, 300 K [169]		4.2				8.3			4.6			16.2
THz-TDS, SC, 300 K [168]									3.8			16.2
INS, SC, 5 K [41]	2.3								3.8		11.7	15.5
PL LW, TF, 150–370 K [53]											11.5	
$MAPbBr_3$, 300 K	5.1	5.3	5.6	5.7	10.5	10.6	10.8	10.9	5.2 (5.1)	5.8 (5.5)	10.9 (10.6)	19.2 (10.9)
IR, TF/SC, 300 K [166]		5.6				9.1			6.3			20.1
IR, SC, 300 K [170]		5.9				9.7			6.0			20.7
IR, SC, 300 K [171]		5.5			8.3		11.9		6.3		12.0	21.0
THz-TDS, SC, 300 K [168]									5.7		9.1	20.1
INS, SC, 5 K [41]									5.1		11.6	16.9
Raman, SC, 20 K [41]									4.1	5.9	11.9	16.3
THz Kerr, SC, 80 K [160]		4.7										
PL LW, TF, 100–370 K [53]											15.3	
$MASnI_3$, 300 K	4.47	4.54	4.85	5.0	8.4	8.9	10.7	11.3	4.48 (4.47)	4.92 (4.85)	11.0 (8.4)	16.1 (11.3)
$MAPbCl_3$, 300 K	7.81	7.99	8.05	8.3	12.2	13.0	15.3	15.7	7.82 (7.81)	8.3 (8.05)	13.6 (13.0)	27.7 (15.7)
IR, TF/SC, 300 K [166]		8.2				11.0			8.7			27.9
THz-TDS, SC, 300 K [168]									8.2		12.4	
$FAPbI_3$, 300 K	3.79	3.80	4.8	5.3	8.3	8.6	11.9	12.0	4.0 (3.8)	4.9 (4.8)	11.4 (8.6)	15.5 (11.9)
PL replica, NC, 3.6 K [40]									3.2		11.1	15.4
INS, SC, 5 K [41]									3.9		9.8	15.1
PL LW, TF, 10–370 K [53]											11.5	
$FAPbBr_3$, 300 K	5.4	5.5	6.5	7.1	9.7	10.0	13.3	13.7	5.5 (5.4)	6.53 (6.50)	12.9 (10.0)	18.8 (13.3)
INS, SC, 5 K [41]									5.5		13.1	22.2
PL replica, NC, 5.5 K [172]									4.4			18.8
PL LW, TF, 10–370 K [53]											15.3	
$FASnI_3$, 300 K	4.93	4.95	5.21	5.8	6.7	6.8	12.1	12.6	4.98 (4.95)	5.24 (5.21)	11.3 (6.7)	15.0 (12.1)
$FAPbCl_3$, 300 K	7.56	7.62	10.1	11.4	12.4	12.9	15.8	16.6	7.64 (7.56)	10.2 (10.1)	15.5 (12.9)	25.8 (15.8)

ogy and findings by comparing our results with experimental measurements.

A. $CsPbI_3$

We first describe our results for cubic $CsPbI_3$ without considering thermal effects. Our DFT-PBEsol calculations for the reference (monomorphous) structure reveal a semimetallic behavior, characterized by a spurious exchange in orbital character between the conduction and valence band extrema [Fig. 12(a)]. We thus assign a negative value to the band gap of −0.05 eV, as reported in Table I. Accounting for positional polymorphism resolves the orbital exchange problem [Fig. 12(b)] and yields a band gap widening of 0.65 eV relative to the monomorphous structure. This band gap increase is the largest among all compounds studied in this work, consistent with the largest energy lowering reported for $CsPbI_3$ in Fig. 2(b). Going beyond DFT and using the PBE0 functional to improve the description of electronic correlations, we obtain a band gap of 1.15 eV for the monomorphous structure. This value is notably lower than the experimental value of 1.78 eV at 650 K [44]. However, for the locally disordered network, the theoretical value improves significantly, yielding 1.84 eV, showing agreement with the experimental value.

At the DFT-PBEsol level, the sign of the effective masses is also reversed due to the orbital exchange character in the monomorphous structure, leading to extremely small hole and electron effective masses of $m^*_{\mathrm{h,ref}} = -0.02$ and $m^*_{\mathrm{e,ref}} = -0.02$. As with the band gap, incorporating local disorder corrects this issue leading to $m^*_{\mathrm{h,poly}} = 0.21$ and $m^*_{\mathrm{e,poly}} = 0.17$. These corrections correspond to hole and electron effective mass enhancement factors due to polymorphism of $\lambda_{\mathrm{h}} = 11.5$ and $\lambda_{\mathrm{e}} = 9.5$, respectively; for the definition of λ refer to Sec. VI E. We note that a more meaningful comparison is with the effective masses reported for the orthorhombic structure at the DFT level, which are $m^*_{\mathrm{h,ortho}} = 0.12$ and $m^*_{\mathrm{e,ortho}} = 0.14$ [44], as this structure accommodates octahedral tilting, which is absent in the monomorphous cubic phase. In this case, the effective mass enhancements captured by polymorphism are $\lambda_{\mathrm{h}} = 0.75$ and $\lambda_{\mathrm{e}} = 0.21$. Furthermore, our calculated effective masses $m^*_{\mathrm{h,poly}} = 0.21$ and $m^*_{\mathrm{e,poly}} = 0.17$ agree well with *GW* values reported for the orthorhombic $\mathrm{CsPbI_3}$ of $m^*_{\mathrm{h},GW} = 0.24$ and $m^*_{\mathrm{e},GW} = 0.23$ [44]. Our value for the reduced effective mass of polymorphous $\mathrm{CsPbI_3}$ is $\mu_{\mathrm{poly}} = 0.094$ which is close to the experimental value [152] of $\mu = 0.114 \pm 0.01$ at $T = 2$ K. Our value also agrees with previous *GW* calculations for orthorhombic $\mathrm{CsPbI_3}$ reporting a reduced effective mass of 0.093 [150] and 0.12 [44].

We now examine the anharmonic phonon dispersion. The cubic phase of $\mathrm{CsPbI_3}$ stabilizes above 539 K [25,44] and thus we focus on temperatures around this value. In Fig. 8(a), we present the calculated ASDM phonon dispersion at 650 K, which converges as early as the second iteration, fully alleviating the instabilities present in the harmonic approximation for the monomorphous structure. Our calculations for the TO modes yield $\omega_{\mathrm{TO_1}} = 3.68$, $\omega_{\mathrm{TO_3}} = 4.7$, and $\omega_{\mathrm{TO_4}} = 10.7$ meV, each of which is doubly degenerate, while $\omega_{\mathrm{TO_2}} = 3.72$ meV remains triply degenerate corresponding to the silent mode. For the LO modes, we obtain $\omega_{\mathrm{LO_1}} = 3.71$, $\omega_{\mathrm{LO_2}} = 5.6$, and $\omega_{\mathrm{LO_3}} = 15.6$ meV. Our values compare well with THz-TDS measurements on thin films containing cubic shaped $\mathrm{CsPbI_3}$ nanocrystals of about 15 nm [157] reported in Table I. Our values for $\omega_{\mathrm{LO_1}}$ and $\omega_{\mathrm{LO_2}}$ also agree well with the experimental values of 3.3 and 5.3 meV obtained from exciton-phonon sidebands in the PL spectra of $\mathrm{CsPbI_3}$ nanocrystals of size 9.31 nm at 3 K [158]. Deviations between our calculations, which are based on single-crystal reference structures, and experimental results on nanocrystals are expected due to size confinement effects, surface ligand interactions, and structural disorder. The latter is addressed in Sec. V D. These factors can alter the lattice dynamics, leading to shifts or broadening of phonon modes.

Now we consider the impact of thermal effects, arising from electron-phonon coupling and thermal expansion, on the band gap and effective masses. Accounting for the extra renormalization on the electronic structure due to thermal effects we obtain a band gap opening of $\Delta E_{\mathrm{g,ref}}(650\,\mathrm{K}) = 0.39$ eV and $\Delta E_{\mathrm{g,poly}}(650\,\mathrm{K}) = 0.13$ eV for the ZG reference and ZG polymorphous structures, respectively (see Table I). The corresponding electron and hole thermal effective mass enhancements are $\lambda_{\mathrm{e,ref}}(650\,\mathrm{K}) = 11$, $\lambda_{\mathrm{h,poly}}(650\,\mathrm{K}) = 0.76$, and $\lambda_{\mathrm{e,poly}}(650\,\mathrm{K}) = 0.47$. We note that we were not able to extract a hole effective mass enhancement for monomorphous cubic $\mathrm{CsPbI_3}$ due to numerical instabilities related to the orbital exchange character at the DFT level. The large reductions due to positional polymorphism in ΔE_{g} and λ_{e} at 650 K show effectively that the thermal-induced renormalization is strongly reduced at the presence of local disorder.

In Fig. 9(a) we compare our calculations for the band gap of cubic $\mathrm{CsPbI_3}$ as a function of temperature using ZG polymorphous (blue discs) and ZG reference (open squares) networks with experimental data from Ref. [44] (gray triangles). To match the experimental data, we shift our DFT values by $\Delta_s = 1.02$ eV close to our PBE0 correction of 1.24 eV (Table I); notably, the shift of 1.02 eV is also consistent with the *GW* correction to DFT of 1.08 eV for orthorhombic $\mathrm{CsPbI_3}$ [44]. From Fig. 9(a), we observe that using the ZG reference structure not only underestimates the experimental values but also results in a band gap closure with increasing temperature, yielding a slope of $dE_{\mathrm{g}}/dT = -6.1\times10^{-4}$ eV/K. This incorrect trend is also reflected in previous electron-phonon calculations for cubic $\mathrm{CsPbI_3}$ in Refs. [49,102]. As shown in Fig. 10, the negative variation of the band gap with temperature when employing a ZG reference structure is attributed to both electron-phonon coupling and thermal lattice expansion. In fact, both $dE_{\mathrm{g}}/dT|_{\mathrm{EPC}}$ and $dE_{\mathrm{g}}/dT|_{\mathrm{TE}}$ indicate a closing of the band gap with temperature. Importantly, employing ZG polymorphous networks recovers the correct trend and reverses the signs of $dE_{\mathrm{g}}/dT|_{\mathrm{EPC}}$ and $dE_{\mathrm{g}}/dT|_{\mathrm{TE}}$, leading to the band gap widening with temperature, consistent with experiments. Our analysis suggests that the electron-phonon coupling dominates thermal-induced band gap renormalization, contributing 97% as shown in Figs. 10(a) and 10(b). The total $dE_{\mathrm{g}}/dT = 1.3\times10^{-4}$ eV/K, however, still underestimates the extracted slope from experimental data, which is 8.3×10^{-4} eV/K. We attribute this discrepancy to (i) the DFT treatment of electron-phonon coupling [122], (ii) the neglect of thermal lattice expansion in phonon calculations, and (iii) insufficient experimental data above 540 K, which limits the accuracy of the extracted slope.

In Fig. 9(e), we also report the temperature variation of the hole and electron effective masses in the range 560–700 K. Using a ZG reference network, we are unable to extract hole effective masses, while the electron effective masses exhibit numerical instabilities, fluctuating around 0.18 m_0 without displaying a clear trend. Using ZG polymorphous networks instead, yields an almost linear variation for both electron (light blue) and hole (dark blue) effective masses with slopes $\lambda^T_{\mathrm{h,poly}} = 3.7\times10^{-4}\ m_0/\mathrm{K}$ and $\lambda^T_{\mathrm{e,poly}} = 1.0\times10^{-4}\ m_0/\mathrm{K}$. We note that as for the band gap, electron-phonon coupling dominates the thermal-induced effective masses enhancements, contributing 95% to $\lambda^T_{\mathrm{h,poly}}$ and 89% to $\lambda^T_{\mathrm{e,poly}}$. The reduced effective mass computed for the ZG polymorphous structures varies linearly from $\mu_{\mathrm{poly}}(560\ \mathrm{K}) = 0.141$ to $\mu_{\mathrm{poly}}(700\ \mathrm{K}) = 0.154$.

B. $\mathrm{CsPbBr_3}$

Here, we describe our calculations for cubic $\mathrm{CsPbBr_3}$. The DFT-PBEsol calculations for the monomorphous structure yield a band gap of 0.24 eV, as reported in Table I. Similar to $\mathrm{CsPbI_3}$, polymorphism leads to a large band gap opening of

0.59 eV relative to the monomorphous structure, compatible with the relative large energy lowering shown in Fig. 2(b). Combining the PBE0 functional for exchange-correlation and the monomorphous structure, we obtain a band gap of 1.52 eV. This value is significantly below the experimental value of 2.39 eV at 430 K [56]. The theoretical value improves significantly when using the locally disordered network, yielding 2.30 eV, which aligns more closely with the experimental value.

At the DFT-PBEsol level, the effective masses are quite small, with $m^*_{\mathrm{h,ref}} = 0.04$ and $m^*_{\mathrm{e,ref}} = 0.04$. Incorporating local disorder through our polymorphous networks increase the effective masses, resulting to $m^*_{\mathrm{h,poly}} = 0.23$ and $m^*_{\mathrm{e,poly}} = 0.23$ which compare well with the hole effective masses of 0.226 and 0.203 ± 0.016 obtained from *GW* calculations for the orthorhombic phase and angle-resolved photoelectron spectroscopy measurements [151]. The hole and electron effective mass enhancement factors due to corrections arising from local disorder are $\lambda_{\mathrm{h}} = 4.75$ and $\lambda_{\mathrm{e}} = 4.75$. These large enhancement factors yield excellent agreement between the reduced effective mass of polymorphous $\mathrm{CsPbBr_3}$ of $\mu_{\mathrm{poly}} = 0.115$ and the experimental value [152] of 0.126 ± 0.01 at $T = 2\,\mathrm{K}$. Furthermore, our calculated value compares well with the *GW* value of 0.102 m_0 reported for orthorhombic $\mathrm{CsPbBr_3}$ in Ref. [150].

Now we study the anharmonic phonon dispersion and subsequently the impact on the band gap and effective masses arising from electron-phonon coupling and thermal expansion. We focus on temperatures above 403 K, where the cubic phase of $\mathrm{CsPbBr_3}$ becomes stable [56,159]. In Fig. 8(b), we show the converged ASDM phonon dispersion at 430 K (second iteration) in excellent agreement with those reported in Refs. [30,147]. For the TO modes, our calculations yield $\omega_{\mathrm{TO_1}} = 4.4$, $\omega_{\mathrm{TO_3}} = 5.8$, and $\omega_{\mathrm{TO_4}} = 13.8\,\mathrm{meV}$ which are doubly degenerate, and $\omega_{\mathrm{TO_2}} = 4.6\,\mathrm{meV}$, which is triply degenerate. For the LO modes, we obtain $\omega_{\mathrm{LO_1}} = 4.5$, $\omega_{\mathrm{LO_2}} = 6.9$, and $\omega_{\mathrm{LO_3}} = 20.3\,\mathrm{meV}$. These values compare well with THz Kerr measurements [160] for orthorhombic $\mathrm{CsPbBr_3}$ single crystals at 80 K, which reveal strongly coupled TO modes of 3.7 and 5.4 meV. We note that the overestimation in theoretical values is largely attributed to the different structural phases considered, as the phonon dispersions of the cubic and orthorhombic phases are known to differ [42]. Our calculated value of $\omega_{\mathrm{LO_3}}$ agrees with the 20 meV obtained from fits of the one-phonon Fröhlich coupling model to PL linewidth measured for $\mathrm{CsPbBr_3}$ nanocrystals [161] with cubic symmetry and size 9.3 nm in the 15–295 K range. Corresponding fits to PL measurements for orthorhombic $\mathrm{CsPbBr_3}$ single crystals in the 10–295 K range yield a value of 16.0 meV [162]. Our computed $\omega_{\mathrm{LO_3}}$ also compares well with 18.9 meV obtained by THz-TDS measurements for a $\mathrm{CsPbBr_3}$ pellet at room temperature.

As show in Table I, the thermal-induced renormalization on the electronic structure of reference and polymorphous networks yields a band gap widening of $\Delta E_{\mathrm{g,ref}}(430\,\mathrm{K}) = 0.41$ and $\Delta E_{\mathrm{g,poly}}(430\,\mathrm{K}) = 0.16\,\mathrm{eV}$. The corresponding hole and electron effective mass enhancements are $\lambda_{\mathrm{h,ref}}(430\,\mathrm{K}) = 4.25$, $\lambda_{\mathrm{e,ref}}(430\,\mathrm{K}) = 3.5$, $\lambda_{\mathrm{h,poly}}(430\,\mathrm{K}) = 0.48$ and $\lambda_{\mathrm{e,poly}}(430\,\mathrm{K}) = 0.43$. The large reductions due to positional polymorphism in ΔE_{g} and λ at 430 K can be explained by the strong reduction in electron-phonon self-energy corrections arising from the weaker response of electrons to lattice vibrations in a disordered environment [110].

In Fig. 9(b) we compare our temperature-dependent band gap calculations using ZG polymorphous (blue discs) and ZG reference (open squares) cubic $\mathrm{CsPbBr_3}$ with experiments from Ref. [56] (gray triangles). Our DFT calculations are shifted by $\Delta_s = 1.38\,\mathrm{eV}$ to match the experimental data; Δ_s compares well with our PBE0 correction of 1.45 eV obtained for the polymorphous structure (see Table I). Our calculations reveal that using the ZG reference structure yields a band gap opening with temperature but underestimates the experimental values by more than 0.35 eV, which cannot be explained by more accurate treatments to exchange-correlation or electron-phonon corrections. Furthermore, our calculated slope of $dE_{\mathrm{g}}/dT = 7.7\times10^{-4}\,\mathrm{eV/K}$ overestimates the experimental value [56] of $3.4\times10^{-4}\,\mathrm{eV/K}$ by approximately 125%. As illustrated in Fig. 10, both $dE_{\mathrm{g}}/dT|_{\mathrm{EPC}}$ and $dE_{\mathrm{g}}/dT|_{\mathrm{TE}}$ computed for the ZG reference structure contribute to the band gap widening with temperature, with the electron-phonon contribution accounting for 82%, as shown in Figs. 10(a) and 10(b). In contrast, the use of ZG polymorphous networks significantly suppresses both the electron-phonon coupling and thermal expansion contributions, with electron-phonon coupling dominating eventually by 94%. The total $dE_{\mathrm{g}}/dT = 2.6\times10^{-4}\,\mathrm{eV/K}$ calculated using ZG polymorphous structures is in good agreement with the experimental slope of $3.4\times10^{-4}\,\mathrm{eV/K}$, as illustrated in Fig. 10(c).

Figure 9(f) shows the variation of the hole and electron effective masses with temperature in the range 400–500 K calculated for the ZG reference (open squares) and ZG polymorphous (blue discs) networks. Our analysis for the slopes yields $\lambda^T_{\mathrm{h,ref}} = 6.0\times10^{-4}$ and $\lambda^T_{\mathrm{e,ref}} = 4.3\times10^{-4}$, $\lambda^T_{\mathrm{h,poly}} = 3.5\times10^{-4}$, and $\lambda^T_{\mathrm{e,poly}} = 2.7\times10^{-4}\ m_0/\mathrm{K}$, showing that the presence of local disorder decreases the slopes by approximately 40%. We also note here that electron-phonon coupling contributes to more than 90% to the thermal-induced effective masses enhancements for both the monomorphous and polymorphous structures. The reduced effective mass obtained for ZG polymorphous cubic $\mathrm{CsPbBr_3}$ varies from $\mu_{\mathrm{poly}}(405\,\mathrm{K}) = 0.159$ to $\mu_{\mathrm{poly}}(500\,\mathrm{K}) = 0.175$.

C. $\mathrm{CsSnI_3}$

In this section, we discuss our results for cubic $\mathrm{CsSnI_3}$. Similar to $\mathrm{CsPbI_3}$, our DFT-PBEsol calculations yield a semimetallic behavior for monomorphous $\mathrm{CsSnI_3}$, due to the spurious exchange in orbital character between the band extrema. We thus assign a negative value to the band gap of $-0.27\,\mathrm{eV}$, as reported in Table I. Taking into account positional polymorphism addresses the band inversion issue and results in a 0.56 eV widening of the band gap compared to the monomorphous structure. By using the PBE0 functional for improved treatment of electronic correlations, we obtain a band gap of 0.67 eV for the monomorphous structure. This value is significantly lower than the experimental value of 1.35 eV at 500 K [54]. Accounting for local disorder yields a PBE0 value of 1.30 eV, which matches the experimental result.

The DFT-PBEsol effective masses exhibit a reversal in sign due to the orbital exchange characteristics of the monomorphous structure, resulting in hole and electron effective masses of $m^*_{\rm h,ref} = -0.07$ and $m^*_{\rm e,ref} = -0.10$. As with the band gap, the incorporation of local disorder corrects this problem, yielding hole and electron effective masses of $m^*_{\rm h,poly} = 0.07$ and $m^*_{\rm e,poly} = 0.09$. These values compare well with quasiparticle self-consistent *GW* calculations for the monomorphous cubic structure, yielding $m^*_{{\rm h},GW} = 0.069$ and light-electron effective mass $m^*_{{\rm e},GW} = 0.068$ [95]. However, this agreement is fortuitous, as the *GW* results do not include SOC, whose omission introduces a significant error together with the neglect of local disorder. In general, SOC effects significantly influence the effective masses in both the monomorphous and polymorphous phases of cubic halide perovskites [30]. Our corrections due to local disorder in cubic $\rm CsSnI_3$ correspond to effective mass enhancement factors of $\lambda_{\rm h} = 1$ and $\lambda_{\rm e} = 0.9$, respectively, and result in a reduced effective mass of $\mu_{\rm poly} = 0.04$, the smallest among all inorganic compounds studied here.

Here, we examine the ASDM phonon dispersion and how electron-phonon coupling and thermal expansion affect the band gap and effective masses of cubic $\rm CsSnI_3$. The cubic phase of $\rm CsSnI_3$ is observed above 440 K [54] and as such, we perform calculations using temperatures around this value. Figure 8(c) shows the anharmonic phonon dispersion at 500 K, which converges at the second ASDM iteration and agrees well with previous calculations within the SCP theory [42,47]. The zone-centered modes lie at $\omega_{\rm TO_1} = 3.9$, $\omega_{\rm TO_2} = 4.0$, $\omega_{\rm TO_3} = 5.3$, and $\omega_{\rm TO_4} = 10.3$ meV, $\omega_{\rm LO_1} = 4.0$, $\omega_{\rm LO_2} = 5.6$, and $\omega_{\rm LO_3} = 16.5$ meV, close to those reported for $\rm CsPbI_3$ at 650 K. Moreover, our values of $\omega_{\rm LO_1}$, $\omega_{\rm LO_2}$ compare well with the PL phonon sidebands of 3.3 and 5.3 meV obtained for $\rm CsPbI_3$ nanocrystals at 3 K [158].

The electronic structure renormalization due to electron-phonon coupling and thermal expansion leads to an overall band gap opening of $\Delta E_{\rm g,ref}(500\,{\rm K}) = 0.52\,{\rm eV}$ and $\Delta E_{\rm g,poly}(500\,{\rm K}) = 0.20\,{\rm eV}$ as reported for the reference and polymorphous structures in Table I. The effective mass enhancements are $\lambda_{\rm h,ref}(500\,{\rm K}) = 2.86$, $\lambda_{\rm e,ref}(500\,{\rm K}) = 1.8\lambda_{\rm h,poly}(500\,{\rm K}) = 0.71$, and $\lambda_{\rm e,poly}(500\,{\rm K}) = 0.89$, showing again a large impact of positional polymorphism on thermal-induced corrections.

In Fig. 9(c), we report the band gap of cubic $\rm CsSnI_3$ as a function of temperature computed using ZG polymorphous (blue discs) and ZG reference (open squares) structures. We compare our calculations with measurements from Ref. [54] (gray triangles). Our DFT values are shifted by $\Delta_s = 0.86$ eV, which compares well with the PBE0 correction of 1.02 eV obtained using the polymorphous structure (Table I). The temperature-dependent band gaps calculated for the reference structure exhibit a band gap widening with increasing temperature, but underestimate the experimental values by over 0.2 eV. The calculated band gap temperature coefficient is $dE_{\rm g}/dT = 3.4\times10^{-4}$ eV/K for the reference structure which compares well with the corresponding coefficient extracted from experimental data of 4.7×10^{-4} eV/K. However, this agreement is fortuitous, as electron-phonon coupling and thermal expansion contribute with opposite sign, as shown in Figs. 10(a) and 10(b). In fact, the computed band gap reduction with lattice expansion is due to the artificial orbital exchange character in reference cubic $\rm CsSnI_3$. Reversing the sign of this contribution yields $dE_{\rm g}/dT = 7.9\times10^{-4}$ eV/K which overestimates the experimental value by 68%. Importantly, the use of polymorphous networks results in a positive $dE_{\rm g}/dT_{\rm TE}$ and an overall $dE_{\rm g}/dT = 3.9\times10^{-4}$ eV/K, which is in close agreement with experiments. Similar to the other Cs-based compounds, our analysis shows a dominant electron-phonon coupling contribution of 84%.

In Fig. 9(g), we show the temperature dependence of the hole and electron effective masses of cubic $\rm CsSnI_3$ in the range 400–600 K. The slopes obtained for the data of the reference (open squares) and polymorphous (blue discs) structures are $\lambda^T_{\rm h,ref} = 2.1\times10^{-4}$, $\lambda^T_{\rm e,ref} = 1.5\times10^{-4}$ and $\lambda^T_{\rm h,poly} = 1.2\times10^{-4}$, $\lambda^T_{\rm e,poly} = 1.7\times10^{-4}$ m_0/K. Similar to the other polymorphous compounds, electron-phonon coupling is the dominant effect contributing to more than 90% to the thermal-induced effective masses enhancements. For polymorphous cubic $\rm CsSnI_3$, we evaluate a reduced effective mass of $\mu_{\rm poly}(400\,{\rm K}) = 0.065$ and $\mu_{\rm poly}(600\,{\rm K}) = 0.080$.

D. $\mathbf{CsPbCl_3}$

Here, we present our findings for cubic $\rm CsPbCl_3$. The DFT-PBEsol calculations for the monomorphous structure yield a band gap of 0.59 eV, as shown in Table I. Similar to other inorganic Pb-based compounds, polymorphism induces a substantial band gap widening of 0.60 eV compared to the monomorphous structure. By applying the PBE0 functional for exchange-correlation to the monomorphous structure, we obtain a band gap of 2.16 eV which underestimates the experimental value of 3.02 eV at 295 K, obtained from PL measurements of the free exciton peak [59]. However, when local disorder is taken into account, the PBE0 band gap opens to 2.79 eV, improving agreement with the experimental result.

The effective masses calculated for the monomorphous structure are $m^*_{\rm h,ref} = 0.12$ and $m^*_{\rm e,ref} = 0.13$. Using locally disordered structures, the effective masses increase to $m^*_{\rm h,poly} = 0.29$ and $m^*_{\rm e,poly} = 0.31$ which correspond to effective mass enhancement factors of $\lambda_{\rm h} = 1.42$ and $\lambda_{\rm e} = 1.38$. The corrections arizing from polymorphism improve considerably the agreement with the experimental reduced effective mass of 0.202 ± 0.01 at $T = 2$ K [153], increasing the calculated value for $\rm CsPbCl_3$ from $\mu_{\rm ref} = 0.062$ to $\mu_{\rm poly} = 0.150$. Despite this important improvement, our computed $\mu_{\rm poly}$ still underestimates experiment by 25%, which we attribute to neglecting quasiparticle and excitonic effects [150,163] from our calculations.

We now examine the anharmonic phonon dispersion and subsequently the thermally induced renormalization of the band gap and effective masses. The cubic phase of $\rm CsPbCl_3$ stabilizes above 325 K [164]. In Fig. 8(d), we present the converged ASDM phonon dispersion at 330 K, achieved at the fifth iteration, where phonon energies extend up to 30 meV. This range is broader compared to other inorganic halide perovskites, owing to the small mass of Cl. The energies of the degenerate TO modes at the Γ point are $\omega_{\rm TO_1} = 4.6$, $\omega_{\rm TO_2} = 6.8$, $\omega_{\rm TO_3} = 8.2$, and $\omega_{\rm TO_4} = 17.4$ meV and of the LO modes are $\omega_{\rm LO_1} = 5.0$, $\omega_{\rm LO_2} = 9.4$, and $\omega_{\rm LO_3} = 28.2$ meV. The value of $\omega_{\rm LO_1}$ compares well with the LO phonon frequency of 4.3 meV, obtained from an one-phonon model fit to the PL linewidths of single crystals in the 185–295 K range, as reported in Ref. [162]. Our data is also compared with Raman measurements [165] of TO modes at 170 K and for LO modes at 2 K for cubic-shaped $CsPbCl_3$ nanocrystals of 8 nm, as shown in Table II. Deviations between theory and experiment can be attributed to various factors, including quantum confinement, surface effects, the dielectric screening environment, and variations in locally disordered domains, as well as the computational setup, such as the choice of functional and lattice parameters. Notably, our calculated phonon energies compare better with data obtained from infrared spectroscopy data on thin films and single crystals of $MAPbCl_3$ at 300 K [166], which report TO phonon energies of 8.2 and 11.0 meV and LO phonon energies of 8.7 and 27.9 meV.

As reported in Table I, the thermal-induced renormalization on the electronic structure of monomorphous and polymorphous networks yields a band gap widening of $\Delta E_{\mathrm{g,ref}}(330\,\mathrm{K}) = 0.33\,\mathrm{eV}$ and $\Delta E_{\mathrm{g,poly}}(330\,\mathrm{K}) = 0.10\,\mathrm{eV}$. The corresponding hole and electron effective mass enhancements are $\lambda_{\mathrm{h,ref}}(330\,\mathrm{K}) = 1.33$, $\lambda_{\mathrm{e,ref}}(330\,\mathrm{K}) = 1.08$, $\lambda_{\mathrm{h,poly}}(330\,\mathrm{K}) = 0.24$, and $\lambda_{\mathrm{e,poly}}(330\,\mathrm{K}) = 0.26$, showing the local disorder suppresses thermal-induced corrections at 330 K.

Figure 9(d) shows the band gap of cubic $CsPbCl_3$ in the temperature range 150–450 K obtained using the ZG polymorphous (blue discs) and ZG reference (open squares) structures. While the cubic phase of $CsPbCl_3$ stabilizes above 325 K [164], we also conduct calculations at temperatures as low as 150 K, where temperature-dependent PL measurements of the free exciton peak (gray triangles) are available [59]. DFT calculations are shifted by $\Delta_s = 1.77\,\mathrm{eV}$ to facilitate comparison with experiment, close to the PBE0 correction of 1.60 eV obtained for the polymorphous structure (see Table I). Our data for the ZG reference structure show a band gap widening with temperature, where the rate of change gradually decreases. Fitting a straight line to our data within the temperature range of 150–450 K yields a slope of $dE_{\mathrm{g}}/dT = 7.6\times10^{-4}\,\mathrm{eV/K}$, which significantly overestimates $0.3\times10^{-4}\,\mathrm{eV/K}$ extracted from experimental data in the range 60–295 K. As illustrated in Fig. 10, both $dE_{\mathrm{g}}/dT|_{\mathrm{EPC}}$ and $dE_{\mathrm{g}}/dT|_{\mathrm{TE}}$ computed using the ZG reference structure contribute to the band gap widening with temperature, with the electron-phonon contribution accounting for 74%, as illustrated in Figs. 10(a) and 10(b). When we employ ZG polymorphous networks both effects become less pronounced, with electron-phonon coupling contributing 81% to the total $dE_{\mathrm{g}}/dT = 3.2\times10^{-4}\,\mathrm{eV/K}$. Although this value shows better agreement, it still significantly overestimates the experimental slope of $0.3\times10^{-4}\,\mathrm{eV/K}$, unlike in the case of $CsPbBr_3$ where our calculated slope matches closely experiments. We attribute this different behavior to the fact that excitonic effects, which are neglected from our calculations, play a more important role in $CsPbCl_3$, as evidenced by its higher binding energy and stronger exciton interactions [150,167].

In Fig. 9(h), we present hole and electron effective masses as a function of temperature calculated for the ZG reference (open squares) and ZG polymorphous (blue discs) structures. We observe that the effective masses of the polymorphous structure follow a clear linear trend, which is more physically consistent, in contrast to the behavior observed for the reference structure. Fitting a straight line to the data yields the slopes $\lambda^T_{\mathrm{h,ref}} = 8.0\times10^{-4}$, $\lambda^T_{\mathrm{e,ref}} = 6.2\times10^{-4}$, $\lambda^T_{\mathrm{h,poly}} = 2.2\times10^{-4}$, and $\lambda^T_{\mathrm{e,poly}} = 2.7\times10^{-4}\ m_0/\mathrm{K}$, showing that local disorder decreases significantly the variation of the effective masses with temperature. Similar to our analysis for the band gap, electron-phonon coupling contribution dominates thermal-induced renormalization of the effective masses being more than 90%. Finally, we report that the reduced effective mass calculated for polymorphous cubic $CsPbCl_3$ varies linearly from $\mu_{\mathrm{poly}}(150\,\mathrm{K}) = 0.169$ to $\mu_{\mathrm{poly}}(450\,\mathrm{K}) = 0.206$.

E. $MAPbI_3$

We now describe our results for MA-based compounds, starting with cubic $MAPbI_3$. The DFT-PBEsol calculations for both the monomorphous and reference structures give a semimetallic behavior with a band gap of 0.06 and 0.03 eV. Unlike in the case of $CsPbI_3$, no electronic band edge inversion is observed [see Figs. 12(c) and 12(d)]. However, using reference structures helps alleviating the problem of an asymmetric charge distribution induced by the net dipole moment of the MA molecule in the monomorphous structure. Incorporating local disorder through polymorphous networks yields an average band gap widening of 0.49 eV relative to the reference structures. As reported in Table I, our PBE0 calculation yields a band gap of 1.23 eV for the reference structure which underestimates the experimental value of 1.61 eV at 315 K [52]. Using polymorphous networks, the theoretical value improves significantly, as we find a band gap of 1.75 eV, close to previous *GW* calculations on the orthorhombic [149] and tetragonal [99] phases, reporting 1.57 and 1.67 eV, respectively. *GW* band gaps of 1.67 eV for the cubic phase were reported in Refs. [101] and [148], based on a ferroelectrically distorted monomorphous structure. However, this symmetry-broken configuration does not reflect the correct macroscopic $Pm\bar{3}m$ symmetry of cubic $MAPbI_3$, leading to unphysical results such as artificial Rashba splitting.

Similar to monomorphous cubic $CsPbI_3$, the DFT-PBEsol hole and electron effective masses are extremely small: $m^*_{\mathrm{h,ref}} = 0.02$ and $m^*_{\mathrm{e,ref}} = 0.02$. Using locally disordered structures increases the effective masses considerably to $m^*_{\mathrm{h,poly}} = 0.16$ and $m^*_{\mathrm{e,poly}} = 0.13$ amounting to hole and electron effective mass enhancement factors of $\lambda_{\mathrm{h}} = 7$ and $\lambda_{\mathrm{e}} = 5.5$, respectively. The large mass enhancements lead to the increase of the reduced effective mass from $\mu_{\mathrm{ref}} = 0.01$ to $\mu_{\mathrm{poly}} = 0.072$ improving significantly the comparison with the experimental value [154] of $\mu = 0.104$ at $T = 2\,\mathrm{K}$ and the calculated value for orthorhombic $MAPbI_3$ of 0.11 obtained within the *GW* approximation [149].

We now focus on the anharmonic phonon dispersion and then on the impact of thermal effects on the band gap and effective masses. Since the cubic phase of $MAPbI_3$ is stable only above 315 K [52,173], our analysis is performed above this temperature regime. In Fig. 8(e), we present the ASDM phonon dispersion of the $MAPbI_3$ reference structure at 315 K, focusing on the energy range associated with the phonon dynamics of the inorganic network. The ASDM converges by the fifth iteration, effectively mitigating the instabilities across the reciprocal space obtained in the harmonic approximation for the ferroelectric monomorphous structure. In addition, the harmonic phonon dispersion exhibits discontinuities at the Γ point, such as a splitting of 1 meV at an energy of approximately 15 meV. These discontinuities originate from anisotropies in the Born effective charge and high-frequency dielectric tensors, which are calculated for the ferroelectric monomorphous structure. These anisotropies, in turn, arise from the net dipole moment of the MA molecule, which breaks the macroscopic symmetry of the lattice and alters the long-range dipole-dipole interactions. As a result, the nonanalytical contribution to the dynamical matrix is affected, leading to direction-dependent LO-TO splitting and discontinuities in the dispersion [42]. The discontinuities at the Γ point are alleviated in the ASDM phonon dispersion, which correctly reflects the isotropic cubic lattice. This is achieved by using average Born effective charge and high-frequency dielectric tensors calculated for the polymorphous structures. This demonstrates that, although local disorder is present in polymorphous structures, on average, those structures reflect the isotropy of the lattice. The ASDM phonon dispersion of $MAPbI_3$ spans a similar energy range (0–15 meV) as that of $CsPbI_3$ shown in Fig. 8(a), and exhibits comparable features, such as the ultrasoft flat band along the R-M direction and the phonon frequencies at the Γ point. The differences between the two dispersions are primarily attributed to the contributions of the Cs atom and the MA molecule and secondarily to the different temperatures used. Our calculated transverse optical and longitudinal optical phonon frequencies at the Γ point for 315 K are $\omega_{\mathrm{TO}_{1-4}} = 3.9 - 4.0$, $\omega_{\mathrm{TO}_{5-8}} = 9.6 - 10.4$, $\omega_{\mathrm{LO}_1} = 3.93$, $\omega_{\mathrm{LO}_2} = 4.2$, $\omega_{\mathrm{LO}_3} = 10.4$, and $\omega_{\mathrm{LO}_4} = 16.2\,\mathrm{meV}$, as reported in Table II. These values compare well with infrared spectroscopy measurements on single crystals at room temperature, reporting TO modes of 4.0 and 7.8 meV and LO modes of 5.0 and 16.5 meV as in Ref. [166], and TO modes of 4.2 and 8.3 meV along with LO modes of 4.6 and 16.2 meV as in Ref. [169]. Similarly, our calculated LO phonon energies agree with THz time-domain spectroscopy measurements at room temperature [168], which find values of 3.8 and 16.2 meV, as well as neutron scattering measurements at 5 K [41] of 3.8, 11.7, and 15.5 meV. We note that our value of $\omega_{\mathrm{LO}_3} = 10.4\,\mathrm{meV}$ compares well with the effective LO phonon frequency of 11.5 meV used to fit temperature-dependent PL linewidth data in Ref. [53]. Small deviations between theory and experiment are attributed to the functional used for the DFT calculations, different lattice constants, as well as to the fact that, due to supercell size constraints, our reference structure preserves only a subgroup of the full $Pm\bar{3}m$ symmetry.

Accounting for the renormalization on the electronic structure due to electron-phonon coupling and thermal expansion, we obtain a band gap opening of $\Delta E_{\mathrm{g,ref}}(315\,\mathrm{K}) = 0.26\,\mathrm{eV}$ and $\Delta E_{\mathrm{g,poly}}(315\,\mathrm{K}) = 0.09\,\mathrm{eV}$ for the reference and polymorphous structures, respectively (see Table I). The corresponding effective mass enhancements are $\lambda_{\mathrm{h,ref}}(315\,\mathrm{K}) = 4.5$, $\lambda_{\mathrm{e,ref}}(315\,\mathrm{K}) = 3.5$, $\lambda_{\mathrm{h,poly}}(315\,\mathrm{K}) = 0.38$, and $\lambda_{\mathrm{e,poly}}(315\,\mathrm{K}) = 0.31$. The pronounced reductions in ΔE_{g}, λ_{h}, and λ_{e} due to polymorphism demonstrate that thermally induced renormalization effects are significantly suppressed in the presence of local positional disorder. Furthermore, our calculations at 315 K suggest an increase of 37% and 31% due to electron-phonon coupling of the hole and electron effective masses, respectively, which compares well with the 28% increase at 300 K calculated for both hole and electron effective masses in the orthorhombic phase using many-body perturbation theory [174].

In Fig. 9(i), we present the temperature-dependent band gaps of cubic $MAPbI_3$ calculated using Boltzmann-weighted averages over 10 ZG polymorphous configurations (red discs) and their corresponding ZG reference structures (open squares) at each temperature. We also report temperature-dependent band gaps computed using only one ZG polymorphous network obtained by geometry optimization of the MSS structure (open circles). We compare our results with the experimental data from Ref. [52] (gray triangles). To match the experimental data, we shift our DFT values by $\Delta_s = 1.00\,\mathrm{eV}$ close to our PBE0 correction of 1.23 eV (Table I); notably, the 1.00 eV shift aligns with the *GW* correction to the DFT value reported for orthorhombic $MAPbI_3$ [149]. Our analysis on data obtained for the reference structures yields a slope of $dE_{\mathrm{g}}/dT = 5.6\times10^{-4}\,\mathrm{eV/K}$ which overestimates the experimental value of $2.6\times10^{-4}\,\mathrm{eV/K}$ by 115%. This overestimation is also observed in electron-phonon calculations performed on ferroelectric monomorphous cubic $MAPbI_3$ in Ref. [102]. Accounting for positional polymorphism suppresses both electron-phonon and thermal-expansion-induced band gap renormalization leading to a slope of $dE_{\mathrm{g}}/dT = 3.1\times10^{-4}\,\mathrm{eV/K}$, which significantly improves the agreement with experiment. Importantly, even when a single ZG polymorphous configuration is used, starting from the MSS structure, the extracted slope of $3.6\times10^{-4}\,\mathrm{eV/K}$ remains in excellent agreement with experiment, as illustrated also by the bar plot in Fig. 10(c). Our analysis shown in Figs. 10(a) and 10(b) suggests that electron-phonon coupling in both reference and polymorphous structures dominates thermal band gap renormalization, contributing to 84% and 88%, respectively.

In Fig. 9(m), we report the temperature variation of the hole and electron effective masses in the range 315–450 K. Using both ZG reference and ZG polymorphous networks, we obtain a linear variation of the effective masses with temperature. Our analysis for the slopes yields $\lambda^T_{\mathrm{h,ref}} = 2.7\times10^{-4}$ and $\lambda^T_{\mathrm{e,ref}} = 1.6\times10^{-4}$, $\lambda^T_{\mathrm{h,poly}} = 4.6\times10^{-4}$, and $\lambda^T_{\mathrm{e,poly}} = 1.0\times10^{-4}\,m_0/\mathrm{K}$, showing that the presence of local disorder increase/decrease the slopes $\lambda^T_{\mathrm{h}}/\lambda^T_{\mathrm{e}}$ by 70%/38%. As for the band gap renormalization, using a single ZG polymorphous configuration obtained from the MSS structure results in excellent agreement with Boltzmann-weighted averages over 10 polymorphous configurations. We remark that in all cases electron-phonon coupling dominates the thermal-induced effective masses enhancements contributing, for example, 97% to $\lambda^T_{\mathrm{h,poly}}$ and 99% to $\lambda^T_{\mathrm{e,poly}}$. The reduced effective mass computed for the ZG polymorphous structure varies linearly from $\mu_{\mathrm{poly}}(315\text{ K}) = 0.096$ to $\mu_{\mathrm{poly}}(450\text{ K}) = 0.110$.

F. $MAPbBr_3$

Now we present our calculations for cubic $MAPbBr_3$. The DFT-PBEsol band gap calculated for the reference structure is

0.39 eV, as reported in Table I. Compared to $\mathrm{CsPbBr_3}$, polymorphism leads to a similar, but smaller, band gap opening of 0.44 eV relative to the reference structure. Using the PBE0 functional, we obtain an average band gap for the reference structures of 1.82 eV. This value underestimates the experimental band gap of 2.34 eV at 300 K [56]. Using locally disordered networks, our theoretical value shows significant improvement, yielding 2.27 eV which considerably enhances the agreement with the experiment. Our value also compares well with the *GW* band gap of 2.56 eV obtained for the tetragonal phase of $\mathrm{MAPbBr_3}$ [100]. The *GW* overestimation of the band gap by 0.22 eV is attributed to the use of a phase other than cubic and to the scalar relativistic treatment of the screened Coulomb interaction W.

At the DFT-PBEsol level, the hole and electron effective masses are $m^*_{\mathrm{h,ref}} = 0.09$ and $m^*_{\mathrm{e,ref}} = 0.09$. Incorporating local disorder through our polymorphous networks increase the effective masses to $m^*_{\mathrm{h,poly}} = 0.19$ and $m^*_{\mathrm{e,poly}} = 0.18$. The effective mass enhancement factors due to these corrections are $\lambda_{\mathrm{h}} = 1.11$ and $\lambda_{\mathrm{e}} = 1.00$. These mass enhancements lead to the increase of the reduced effective mass of cubic $\mathrm{MAPbBr_3}$ from $\mu_{\mathrm{ref}} = 0.045$ to $\mu_{\mathrm{poly}} = 0.092$ improving considerably the comparison with the experimental values [81,154] of 0.106 and 0.117 at $T = 2$ K. As with the band gap, the *GW* calculations of Ref. [100] yield an overestimated value of 0.144 for tetragonal $\mathrm{MAPbBr_3}$, likely due to the scalar relativistic treatment of the screened Coulomb interaction W.

Now we examine ASDM phonon dispersion and subsequently the effect of electron-phonon coupling and thermal expansion on the band gap and effective masses. We study temperatures above 250 K, where the cubic phase of $\mathrm{MAPbBr_3}$ is stable [56,175]. Figure 8(f) shows the ASDM phonon dispersion of the $\mathrm{MAPbBr_3}$ reference structure at 300 K, focusing on phonons energies related to the inorganic network. The ASDM converges by the sixth iteration, alleviating the harmonic phonon instabilities calculated for the ferroelectric monomorphous structure. As for the case of $\mathrm{MAPbI_3}$, the discontinuities at the Γ point are alleviated in the ASDM phonon dispersion by using average Born effective charge and dielectric tensors computed for the polymorphous structures, reflecting the isotropy of the cubic lattice. The anharmonic phonons related to the inorganic network of $\mathrm{MAPbBr_3}$ lie within the energy range of 0–20 meV, similar to that of $\mathrm{CsPbBr_3}$ shown in Fig. 8(b). Apart from the contributions related to the Cs atom and MA molecule [see Figs. 14(a) and 14(b)] and the different temperature used, both phonon dispersions exhibit similar characteristics, including the ultrasoft flat band along the R-M direction. However, the frequency of the high-energy TO mode at the Γ point of $\mathrm{MAPbBr_3}$ is about 3 meV lower in energy compared to that of $\mathrm{CsPbBr_3}$. Particularly, our anharmonicity calculations for $\mathrm{MAPbBr_3}$ at 300 K yield $\omega_{\mathrm{TO_{1\text{–}4}}} = 5.1$–$5.7$, $\omega_{\mathrm{TO_{5\text{–}8}}} = 10.5$–$10.9$, $\omega_{\mathrm{LO_1}} = 5.2$, $\omega_{\mathrm{LO_2}} = 5.8$, $\omega_{\mathrm{LO_3}} = 10.9$, and $\omega_{\mathrm{LO_4}} = 19.2$ meV, as reported in Table II. These values are in good agreement with PL, inelastic neutron scattering, infrared, Raman, or other THz spectroscopy measurements for $\mathrm{MAPbBr_3}$ [41,53,160,166,168,170,171]. In particular, focusing on room temperature measurements, the following values are reported: (i) TO modes of 5.6 and 9.1 meV and LO modes of 6.3 and 20.1 meV [166], (ii) TO modes of 5.9 and 9.7 meV and LO modes of 6.0 and 20.7 meV [170], (iii) TO modes of 5.5 and 8.3, and 11.9 meV and LO modes of 6.3, 12.0, and 21.0 meV [171], and (iv) LO modes of 5.7, 9.1, and 20.1 meV [168]. We note that an effective LO phonon frequency of 15.3 meV was used in Ref. [53] to fit an one-phonon Fröhlich coupling model to PL linewidths in the 100–370 K range. This value lies nearly midway between our computed $\omega_{\mathrm{LO_3}} = 10.9$ meV and $\omega_{\mathrm{LO_4}} = 19.2$ meV. Discrepancies between theory and experiment are related to the choice of functional used in the DFT calculations, differences between the lattice constants, and to the supercell size used, in which our reference structure preserves only a subgroup of the full $\mathrm{Pm\bar{3}m}$ symmetry.

As show in Table I, the thermal-induced renormalization on the electronic structure of reference and polymorphous networks yields a band gap widening of $\Delta E_{\mathrm{g,ref}}(430\,\mathrm{K}) = 0.17$ and $\Delta E_{\mathrm{g,poly}}(430\,\mathrm{K}) = 0.08$ eV. The corresponding hole and electron effective mass enhancements are $\lambda_{\mathrm{h,ref}}(430\,\mathrm{K}) = 0.66$, $\lambda_{\mathrm{e,ref}}(430\,\mathrm{K}) = 2.8$, $\lambda_{\mathrm{h,poly}}(430\,\mathrm{K}) = 0.37$, and $\lambda_{\mathrm{e,poly}}(430\,\mathrm{K}) = 0.28$. It is clear that both ΔE_{g} and λ are diminished due to positional polymorphism; this is attributed to the reduced coupling of electrons to lattice vibrations in a distorted octahedral network, which in turn decreases the Fan-Migdal electron-phonon self-energy correction [110].

In Fig. 9(j), we present the band gap of cubic $\mathrm{MAPbBr_3}$ as function of temperature evaluated as Boltzmann-weighted average over 10 ZG polymorphous configurations (red discs) and their ZG reference structures (open squares). Temperature-dependent band gaps computed using a single ZG polymorphous network obtained through geometry optimization of the MSS structure are also reported (open circles). We compare our results with the experimental data from Ref. [56] (gray triangles). Our DFT calculations are shifted by our PBE0 correction of 1.44 eV (see Table I) to match the experimental data. Calculations indicate that using reference structures results in a band gap widening with temperature, but underestimates the experiment by more than 0.30 eV, a discrepancy that can be resolved by employing ZG polymorphous structures. In addition, our calculated slope of $dE_{\mathrm{g}}/dT = 5.8\times10^{-4}$ eV/K for the ZG reference structures overestimates the experimental value [56] of 2.8×10^{-4} eV/K by more than a factor of 2. As shown in Figs. 10(a) and 10(b) for the reference structures, both $dE_{\mathrm{g}}/dT|_{\mathrm{EPC}}$ and $dE_{\mathrm{g}}/dT|_{\mathrm{TE}}$ contribute to the temperature-induced band gap widening, with the electron-phonon contribution accounting for 71%. The use of polymorphous networks reduces both the electron-phonon coupling and thermal expansion contributions, with electron-phonon coupling remaining the dominant effect, accounting for approximately 70%. The total slope calculated using ZG polymorphous structures is $dE_{\mathrm{g}}/dT = 2.9\times10^{-4}$ eV/K which agrees with the experimental one of 2.8×10^{-4} eV/K. Remarkably, even when a single ZG polymorphous configuration is used, starting from the MSS structure, maintains excellent agreement with the experimental data, with the extracted slope being 2.1×10^{-4} eV/K.

Figure 9(n) shows temperature-dependent hole and electron effective masses in the range 275–450 K calculated using ZG reference (open squares) and ZG polymorphous (red discs) networks. Unlike the hole effective mass of 0.15 m_0 at 300 K obtained for the reference structures, our calculated value of 0.26 m_0 for the polymorphous structures at 300 K is in excellent agreement with angle-resolved photoemission measurements at room temperature, which report a value of 0.25 ± 0.05 m_0 [176]. Importantly, even when using a single ZG polymorphous configuration obtained from the MSS structure [open circles in Fig. 9(n)], the results compare well with our values obtained from Boltzmann-weighted averages over 10 polymorphous configurations, i.e., when including configurational entropy effects. Linear fits to the data give slopes of $\lambda^T_{\mathrm{h,ref}} = 2.5\times10^{-4}$, $\lambda^T_{\mathrm{e,ref}} = 2.0\times10^{-4}$ and $\lambda^T_{\mathrm{h,poly}} = 1.5\times10^{-4}$, $\lambda^T_{\mathrm{e,poly}} = 0.9\times10^{-4}$ m_0/K, showing that local disorder decreases the slopes by 40% and 55%, close to the values obtained for $\mathrm{CsPbBr_3}$. We note that in our calculations, electron-phonon coupling dominates by 85%–92% the thermal-induced effective masses enhancements for both the reference and polymorphous structures. The reduced effective mass obtained for polymorphous cubic $\mathrm{MAPbBr_3}$ varies linearly from $\mu_{\mathrm{poly}}(275\ \mathrm{K}) = 0.120$ to $\mu_{\mathrm{poly}}(450\ \mathrm{K}) = 0.130$.

G. $\mathbf{MASnI_3}$

In this section, we discuss our results for cubic $\mathrm{MASnI_3}$. Similar to $\mathrm{CsPbI_3}$ and $\mathrm{CsSnI_3}$, our DFT-PBEsol calculations yield a semimetallic behavior for the reference structures of $\mathrm{MASnI_3}$ and a spurious exchange in orbital character between the band extrema. We thus assign a negative value to the band gap of -0.09 eV, as reported in Table I. The band inversion issue is addressed when taking into account positional polymorphism which results in a band gap widening of 0.37 eV. Our PBE0 calculations for the reference structures give a band gap of 0.88 eV, which underestimates the experimental value of 1.31 eV at 300 K [61]. Employing locally disordered networks results in a band gap opening to 1.30 eV, which is in agreement with experiment and compares well with the *GW* value of 1.1 eV reported for tetragonal $\mathrm{MASnI_3}$ [99].

Similar to $\mathrm{CsPbI_3}$ and $\mathrm{CsSnI_3}$, the effective masses of the reference structures exhibit a reversal in sign due to orbital exchange at the DFT-PBEsol level. This results in hole and electron effective masses of $m^*_{\mathrm{h,ref}} = -0.05$ and $m^*_{\mathrm{e,ref}} = -0.03$. As with the band gap, local disorder corrects this problem and DFT-PBEsol hole and electron effective masses become $m^*_{\mathrm{h,poly}} = 0.06$ and $m^*_{\mathrm{e,poly}} = 0.09$. These effective masses are the smallest among all hybrid halide compounds studied here and expected to be at the origin of the high mobility reported for $\mathrm{MASnI_3}$ in Ref. [60]. The adjustments due to local disorder correspond to effective mass enhancement factors of $\lambda_{\mathrm{h}} = 1.2$ and $\lambda_{\mathrm{e}} = 3$, respectively, The reduced effective mass of cubic $\mathrm{MASnI_3}$ increase from $\mu_{\mathrm{ref}} = 0.019$ to $\mu_{\mathrm{poly}} = 0.036$.

Now we examine phonon anharmonicity in cubic $\mathrm{MASnI_3}$. The cubic phase of $\mathrm{MASnI_3}$ is observed above 275 K [61,177] and therefore we perform calculations using temperatures around this value. Figure 8(g) shows the anharmonic phonon dispersion at 300 K in the energy range 0–16 meV, which converges at the fifth ASDM iteration. The discontinuities at the Γ point present in the harmonic phonon dispersion arise from the use of a ferroelectric monomorphous structure, which induces anisotropy in the Born effective charge and dielectric tensors, and thus in the long-range contribution to the dynamical matrix. As with the other MA-based compounds, this issue is resolved in the anharmonic phonon dispersion by using averaged Born effective charges and dielectric tensors calculated from the polymorphous structures. The anharmonic phonon dispersion related to the inorganic network of $\mathrm{MASnI_3}$ exhibits similarities with the one reported for $\mathrm{CsSnI_3}$ [Fig. 8(c)], including an identical energy range of 0–16 meV and the low energy flat band along the R-M direction. The main differences are attributed to the contributions of the A-site cation, the different temperatures considered, and the choice of reference structure, which preserves only a subgroup of the full $Pm\bar{3}m$ symmetry. For $\mathrm{MASnI_3}$, the zone-center frequencies $\omega_{\mathrm{TO_1}} = 4.47$, $\omega_{\mathrm{TO_4}} = 8.4$, $\omega_{\mathrm{LO_2}} = 4.92$, and $\omega_{\mathrm{LO_4}} = 16.1$ meV, compare well with the spectroscopy data reported for $\mathrm{MAPbI_3}$ single crystals at room temperature: 4.0, 7.8, 5.0, and 16.5 meV [166], and 4.2, 8.3, 4.6, and 16.2 meV [169], respectively.

The thermal-induced electronic structure renormalization leads to an overall band gap opening of $\Delta E_{\mathrm{g,ref}}(300\ \mathrm{K}) = 0.22$ eV and $\Delta E_{\mathrm{g,poly}}(300\ \mathrm{K}) = 0.13$ eV as reported for the ZG reference and ZG polymorphous structures in Table I. The hole and electron effective mass enhancement factors are $\lambda_{\mathrm{h,ref}}(300\ \mathrm{K}) = 1.8$, $\lambda_{\mathrm{e,ref}}(300\ \mathrm{K}) = 3.0\lambda_{\mathrm{h,poly}}(300\ \mathrm{K}) = 0.5$, and $\lambda_{\mathrm{e,poly}}(300\ \mathrm{K}) = 0.4$, showing that local disorder reduces thermal-induced corrections.

Figure 9(k) shows the band gap of cubic $\mathrm{MASnI_3}$ as a function of temperature. Red discs and open squares represent Boltzmann-weighted averages over the band gaps computed for 10 ZG polymorphous configurations and their ZG reference structures, respectively. Open circles represent temperature-dependent band gaps computed using a single ZG polymorphous network obtained from the MSS structure. Gray triangles are experimental data from Ref. [61]. Our DFT values are shifted by $\Delta_s = 0.90$ eV, which aligns with our PBE0 correction of 1.02 eV obtained for the polymorphous structures. This shift also aligns with the *GW* correction of 0.79 eV reported in Ref. [99] for tetragonal $\mathrm{MASnI_3}$. The reference structures exhibit a band gap widening with increasing temperature, but they underestimate the experimental values by about 0.3 eV. The calculated temperature coefficient of the band gap for the reference structures is $dE_{\mathrm{g}}/dT = 3.4\times10^{-4}$ eV/K, which shows good agreement with the experimentally determined value of 4.5×10^{-4} eV/K. Similar to the case of $\mathrm{CsSnI_3}$, this agreement appears coincidental, since electron-phonon coupling and thermal expansion contribute with opposite signs, as illustrated in Figs. 10(a) and 10(b). Specifically, the negative thermal expansion contribution arises from the orbital exchange character in the reference structures of cubic $\mathrm{MASnI_3}$. Adjusting the sign of this contribution results in $dE_{\mathrm{g}}/dT = 7.2\times10^{-4}$ eV/K, which overestimates the experimental value by 60%. Using ZG locally disordered networks gives a positive $dE_{\mathrm{g}}/dT_{\mathrm{TE}}$ and an overall $dE_{\mathrm{g}}/dT = 5.7\times10^{-4}$ eV/K which is closer to experiment. Notably, even a single ZG polymorphous configuration, derived from the MSS structure, reproduces a nearly identical temperature coefficient of 5.6×10^{-4} eV/K. Similar to Cs-based and MA-based compounds, our analysis shows that electron-phonon coupling is the leading contribution, accounting for 61%.

Figure 9(o) shows the temperature dependence of the hole and electron effective masses of cubic $\mathrm{MASnI_3}$ in the range 250–450 K. Linear fits to the data obtained for the ZG reference (open squares) and ZG polymorphous (red discs) structures are $\lambda^T_{\mathrm{h,ref}} = 0.8\times10^{-4}$, $\lambda^T_{\mathrm{e,ref}} = 0.3\times10^{-4}$ and $\lambda^T_{\mathrm{h,poly}} = 1.5\times10^{-4}$, $\lambda^T_{\mathrm{e,poly}} = 2.1\times10^{-4}$ m_0/K. A single ZG polymorphous configuration derived from the MSS structure [open circles in Fig. 9(o)] yields similar slopes to those obtained from Boltzmann-weighted averages over 10 ZG polymorphous configurations but underestimates the values by about 0.02. Electron-phonon coupling is the leading thermal effect, contributing to more than 75% to the effective masses enhancements. For polymorphous cubic $\mathrm{MASnI_3}$, the reduced effective mass exhibits a linear temperature dependence, increasing from $\mu_{\mathrm{poly}}(250\ \mathrm{K}) = 0.049$ to $\mu_{\mathrm{poly}}(450\ \mathrm{K}) = 0.067$.

H. $\mathrm{MAPbCl_3}$

Here, we present our findings for cubic $\mathrm{MAPbCl_3}$. The DFT-PBEsol calculations for the reference structures yield a band gap of 0.72 eV, as shown in Table I. Local disorder induces a substantial band gap widening of 0.52 eV, which is the largest among all MA-based compounds studied in this work, consistent with the largest energy lowering reported for $\mathrm{MAPbCl_3}$ in Fig. 2(b). Our PBE0 calculations for the reference structures give a band gap of 2.34 eV which underestimates significantly the experimental values of 2.88 and 3.07 eV at 300 K, obtained from PL measurements of the major emission peak [51,55]. Significant improvements are observed when employing locally disordered networks in combination with the PBE0 approximation, yielding a band gap of 2.88 eV which is in excellent agreement with experiments. A *GW* band gap of 3.46 eV has been previously reported for tetragonal $\mathrm{MAPbCl_3}$ [100], which overestimates experiment by approximately 0.4–0.6 eV. This discrepancy has been primarily attributed to the use of a scalar relativistic approximation for the screened Coulomb interaction, neglecting spin-orbit coupling for W [22].

The effective masses calculated for the reference structures are $m^*_{\mathrm{h,ref}} = 0.15$ and $m^*_{\mathrm{e,ref}} = 0.16$. Using locally disordered structures, the effective masses increase to $m^*_{\mathrm{h,poly}} = 0.26$ and $m^*_{\mathrm{e,poly}} = 0.27$. The associated hole and electron effective mass enhancement factors due to polymorphism are $\lambda_{\mathrm{h}} = 0.73$ and $\lambda_{\mathrm{e}} = 0.63$. Corrections arising from polymorphism increase the reduced effective mass from $\mu_{\mathrm{ref}} = 0.077$ to $\mu_{\mathrm{poly}} = 0.132$. The latter value lies within the inherent accuracy of the *GW* value of 0.159 reported for tetragonal $\mathrm{MAPbCl_3}$ in Ref. [100] that neglects spin-orbit coupling in W.

The cubic phase of $\mathrm{MAPbCl_3}$ stabilizes above 180 K [55] and therefore we perform calculations using temperatures above this value. In Fig. 8(h), we present the converged ASDM phonon dispersion at 300 K, achieved at the sixth iteration, in the energy range associated with the vibrations of the inorganic sublattice (0–31 meV). Similar to other hybrid halide perovskites, the harmonic phonon dispersion displays phonon instabilities, lifted degeneracies, and discontinuities at the Γ point due to the fixed molecular orientation in the ferroelectric monomorphous structure. As for other hybrid halide perovskites, in our anharmonic phonon calculations we resolve these issues by including phonon self-energy corrections, taking the MSS structure as a reference, and computing the nonanalytic contribution to the dynamical matrix based on Born effective charge and high-frequency dielectric tensors of the polymorphous structures. The anharmonic phonon dispersions of $\mathrm{MAPbCl_3}$ and $\mathrm{CsPbCl_3}$ [Fig. 8(d)] have some similar characteristics, spanning comparable energy ranges and both exhibiting an ultrasoft, flat phonon band along the R-M direction. The primary differences arise from the contributions of the A-site cations and the selection of the MSS structure that retains only a subgroup of the full $Pm\bar{3}m$ symmetry. Table II reports the frequencies at the Γ point of $\mathrm{MAPbCl_3}$: $\omega_{\mathrm{TO}_{1-4}} = 7.8$–$8.3$, $\omega_{\mathrm{TO}_{5-6}} = 12.2$–$13.0$, $\omega_{\mathrm{TO}_{7-8}} = 15.3$–$15.7$, $\omega_{\mathrm{LO}_1} = 7.8$, $\omega_{\mathrm{LO}_2} = 8.3$, $\omega_{\mathrm{LO}_3} = 13.6$, and $\omega_{\mathrm{LO}_4} = 27.7$ meV. A good agreement is observed with experimental data from infrared and THz-TDS spectroscopy on $\mathrm{MAPbCl_3}$ at room temperature, which identify TO modes at 8.2 and 11.0 meV and LO modes at 8.2, 8.7, 12.4, and 27.9 meV [166,168].

We next investigate the renormalization of the band gap and effective masses due to electron-phonon coupling and thermal expansion. Figure 9(l) shows the band gap of cubic $\mathrm{MAPbCl_3}$ in the temperature range 200–400 K obtained using 10 ZG polymorphous (red discs) and 10 ZG reference (open squares) structures for each temperature. We also include temperature-dependent band gaps computed with the ZG polymorphous configuration of the MSS structure (open cirles). Experimental data (gray triangles) are from Ref. [55]. To enable direct comparison with experiment, the DFT data are rigidly shifted by $\Delta_s = 1.73$ eV. This value matches the PBE0 correction of 1.64 eV obtained for the polymorphous structures (see Table I). Our data for the ZG reference structures show a temperature-induced band gap widening, with a temperature coefficient of $dE_{\mathrm{g}}/dT = 6.2\times10^{-4}$ eV/K. This value significantly overestimates the experimentally derived coefficient of -0.9×10^{-4} eV/K, which indicates that the band gap remains nearly constant with temperature in the measured range. As illustrated in Figs. 10(a) and 10(b), both $dE_{\mathrm{g}}/dT|_{\mathrm{EPC}}$ and $dE_{\mathrm{g}}/dT|_{\mathrm{TE}}$ computed for the reference structures lead to band gap widening, with electron-phonon coupling accounting for 48%. Notably, this is the only case among Cs-based and MA-based compounds where thermal expansion is the leading contribution to the thermal-induced band gap renormalization. When ZG polymorphous networks are employed, electron-phonon coupling results in band gap narrowing, uniquely among all compounds studied, while thermal expansion continues to induce a band gap widening, though its contribution is reduced. The total temperature coefficient of the band gap for the polymorphous structures is $dE_{\mathrm{g}}/dT = 0.9\times10^{-4}$ eV/K, which closely matches the experimental value, as shown in Fig. 10(c). Overall, we attribute the nearly constant variation of the band gap with temperature to the opposing effects of electron-phonon coupling and thermal expansion. Unlike for the other MA-based compounds, a single ZG polymorphous configuration derived from the MSS structure does not provide a sufficiently accurate approximation for computing temperature-dependent band gaps, yielding a temperature coefficient of 3.8×10^{-4} eV/K.

In Fig. 9(p), we present the temperature dependence of the hole and electron effective masses calculated using the ASDM for both the reference (open squares) and polymorphous structures (red discs). The effective masses of the ZG reference structures exhibit a monotonic increase with temperature, whereas those in the ZG polymorphous structures remain nearly constant, mirroring the trend observed for the band gap. Fitting a straight line to the data yields the slopes $\lambda^T_{\rm h,ref} = 1.6\times10^{-4}$, $\lambda^T_{\rm e,ref} = 1.8\times10^{-4}$ and $\lambda^T_{\rm h,poly} = 0.9\times10^{-4}$, $\lambda^T_{\rm e,poly} = 0.2\times10^{-4}$ m_0/K, showing that local disorder affects significantly the variation of the effective masses with temperature. We remark that now electron-phonon coupling contribution dominates thermal-induced renormalization of the effective masses being more than 70%. We also report that the reduced effective mass calculated for polymorphous cubic $\mathrm{MAPbCl_3}$ remains linearly constant being $\mu_{\rm poly}(200\ \mathrm{K}) = 0.170$ and $\mu_{\rm poly}(400\ \mathrm{K}) = 0.172$. Finally, we note that as for the band gap, a single ZG polymorphous configuration derived from the MSS structure [open circles in Fig. 9(p)] is not a good approximation to explain the temperature variation of the effective masses.

I. $\mathrm{FAPbI_3}$

We next present our results for cubic $\mathrm{FAPbI_3}$. DFT-PBEsol calculations for the reference structure reveal a semimetallic behavior with a band gap of 0.10 eV. However, unlike $\mathrm{CsPbI_3}$ [Figs. 12(a) and 12(b)], our charge density plots [Figs. 12(f) and 12(g)] do not display any spurious exchange in orbital character between the conduction and valence band extrema. Accounting for positional polymorphism leads to a relatively small band gap widening of 0.24 eV, consistent with the relatively small degree of polymorphism in FA-based compounds (Fig. 2). Going beyond DFT, PBE0 calculations give a band gap of 1.33 eV for the reference structures. Although this underestimates the experimental value of 1.53 eV at 300 K [58], it remains in reasonable agreement. Employing polymorphous networks results in a band gap of 1.59 eV, aligning better with experiment and again highlighting the importance of local disorder in accurate band gap predictions. Our result also compares well with *GW* calculations for tetragonal $\mathrm{FAPbI_3}$, which report a band gap of 1.71 eV [107]. Previous *GW* calculations, based on idealized ferroelectric monomorphous structures that are not representative of the actual physical system yielding an artificial Rashba splitting, report a band gap of 1.47 and 1.48 eV [101,178]. We emphasize that band structures of polymorphous structures do not exhibit a Rashba band splitting of the doubly degenerate band extrema [30,110] as they reflect, on average, the system's centrosymmetricity.

At the DFT-PBEsol level, the spurious semimetallic behavior leads to extremely small hole and electron effective masses of $m^*_{\rm h,ref} = 0.03$ and $m^*_{\rm e,ref} = 0.03$. As with the band gap, incorporating local disorder increases the effective masses to $m^*_{\rm h,poly} = 0.10$ and $m^*_{\rm e,poly} = 0.09$, correpondig to effective mass enhancement factors of $\lambda_{\rm h} = 2.3$ and $\lambda_{\rm e} = 2.0$, respectively. Our calculated reduced effective mass increases significantly from $\mu_{\rm ref} = 0.015$ to $\mu_{\rm poly} = 0.047$ for polymorphous $\mathrm{FAPbI_3}$. However, this value still substantially underestimates the experimental measurements for orthorhombic and tetragonal $\mathrm{FAPbI_3}$, reported as 0.09 and 0.095, respectively [154]. This underestimation is attributed to the semilocal treatment of exchange-correlation effects within DFT and the relatively small degree of polymorphism exhibited by FA-based compounds. Previous *GW* calculations [106] on a ferroelectrically distorted monomorphous configuration of cubic $\mathrm{FAPbI_3}$, (though unphysical, exhibiting a relatively large $\mu_{GW} = 0.121$) report an increase in the DFT hole and electron effective masses of 72% and 93%, respectively. Applying these corrections to our DFT effective masses of polymorphous $\mathrm{FAPbI_3}$ yields a renormalized value of $\mu_{{\rm poly}+GW} = 0.086$, in excellent agreement with the experimental values.

In the following we present the anharmonic phonon dispersion. The cubic phase of $\mathrm{FAPbI_3}$ stabilizes above 285 K [179] and thus we perform calculations using temperatures around this value. In Fig. 8(i), we present the calculated ASDM phonon dispersion at 300 K, which converges by the fourth iteration. We focus on the energy range 0–16 meV, mostly associated with vibrations of the inorganic atoms. Accounting for anharmonicity with the ASDM fully alleviates the strong instabilities present in the harmonic phonon dispersion calculated for the ferroelectric monomorphous structure. The differences between the anharmonic phonon dispersions of cubic $\mathrm{MAPbI_3}$ [Fig. 8(e)] and $\mathrm{FAPbI_3}$ are primarily attributed to the distinct contributions of the MA and FA cations and the indirect coupling between the lattice dynamics of the organic and inorganic sublattices. The phonon frequencies at the Γ point for 300 K are $\omega_{\mathrm{TO}_{1-4}} = 3.79$–$5.3$, $\omega_{\mathrm{TO}_{5-6}} = 8.3$–$8.6$, $\omega_{\mathrm{TO}_{7-8}} = 11.9$–$12.0$, $\omega_{\mathrm{LO}_1} = 4.0$, $\omega_{\mathrm{LO}_2} = 4.9$, $\omega_{\mathrm{LO}_3} = 11.4$, and $\omega_{\mathrm{LO}_4} = 15.5$ meV, as reported in Table II. Analysis of phonon sidebands in PL spectra at 3.6 K of $\mathrm{FAPbI_3}$ nanocrystals [40], which have a cubic crystal structure and average sizes of 10–15 nm, yields LO phonons of 3.2, 7.8, and 15.4 meV. These values compare well with our calculations except the mode at 7.8 meV which differs from our calculated value of 11.4 meV. However, as reported in Ref. [40], high-energy excitations result in temporal fluctuations of the intermediate phonon, spanning an energy range from 7.2 to 15 meV. Therefore, in Table II, we adopt the mean value of this range, 11.1 meV, as the representative intermediate phonon energy. Close to this value, Refs. [40] and [53] report an effective LO phonon of 10.7 and 11.5 meV, respectively, obtained by one-phonon Fröhlich coupling model fits to temperature-dependent PL linewidths. Our calculations are also in good agreement with inelastic neutron scattering data [41] of 3.9, 9.8, and 15.1 meV, obtained for the low temperature phase of $\mathrm{FAPbI_3}$.

Now we move to the effect of thermal effects on the electronic structure. As reported in Table I, our calculations with the ASDM accounting for anharmonic electron-phonon coupling and thermal expansion yield a band gap opening of $\Delta E_{\rm g,ref}(300\,\mathrm{K}) = 0.39$ eV and $\Delta E_{\rm g,poly}(300\,\mathrm{K}) = 0.13$ eV for the ZG reference and ZG polymorphous structures. The corresponding electron and hole effective mass enhancements, derived using the renormalization Δm^* reported in Table I, are $\lambda_{\rm h,ref}(300\,\mathrm{K}) = 2.3$, $\lambda_{\rm e,ref}(300\,\mathrm{K}) = 1.7$ and $\lambda_{\rm h,poly}(300\,\mathrm{K}) = 0.6$, $\lambda_{\rm e,poly}(300\,\mathrm{K}) = 0.4$. These values show that local disorder leads to a considerable reduction to the thermal-induced renormalization of the electronic structure of $\mathrm{FAPbI_3}$.

In Fig. 9(q) we compare the band gap of cubic $\mathrm{FAPbI_3}$ as a function of temperature calculated for ZG polymorphous (black discs) and ZG reference (open squares) networks with measurements from Ref. [58] (gray triangles). The DFT data are shifted by $\Delta_s = 1.10\,\mathrm{eV}$ close to our calculated PBE0 correction of 1.25 eV (see Table I). A linear fit to the data obtained for the ZG reference structures yields a slope of $dE_\mathrm{g}/dT = 7.5\times10^{-4}\,\mathrm{eV/K}$ which overestimates the experimental value of $4.3\times10^{-4}\,\mathrm{eV/K}$ by 75%. Accounting for positional polymorphism improves significantly the agreement with experiment as it suppresses both electron-phonon coupling and thermal expansion leading to a temperature coefficient $dE_\mathrm{g}/dT = 4.6\times10^{-4}\,\mathrm{eV/K}$. Figure 9(q) also reports data calculated using only the ZG polymorphous network of the MSS structure (open circles). Remarkably, our values overlay with data obtained from Boltzmann-weighted averages over 10 ZG polymorphous structures, with the extracted coefficient being $4.5\times10^{-4}\,\mathrm{eV/K}$. As shown in Figs. 10(a) and 10(b), electron-phonon coupling contributes more significantly than thermal expansion, accounting for 65% and 70% in our calculated band gap renormalization for the ZG reference and ZG polymorphous structures, respectively.

In Fig. 9(u), we report hole and electron effective masses in the temperature range 220–350 K, revealing a thermal-driven increase for both the ZG reference (open squares) and ZG polymorphous structures (dark discs). The slopes extracted from linear fits to the data are $\lambda^T_\mathrm{h,ref} = 2.8\times10^{-4}$, $\lambda^T_\mathrm{e,ref} = 1.9\times10^{-4}$ and $\lambda^T_\mathrm{h,poly} = 3.3\times10^{-4}$, $\lambda^T_\mathrm{e,poly} = 1.7\times10^{-4}\ m_0/\mathrm{K}$. Similar to the band gap renormalization, more than 75% of λ^T arises from electron-phonon coupling in all cases. We also report that the reduced effective mass calculated for polymorphous cubic $\mathrm{FAPbI_3}$ varies linearly being $\mu_\mathrm{poly}(220\ \mathrm{K}) = 0.063$ to $\mu_\mathrm{poly}(350\ \mathrm{K}) = 0.078$. Applying the *GW* corrections [106] of 72% and 93% to the DFT hole and electron effective masses gives $\mu_{\mathrm{poly}+GW}(220\ \mathrm{K}) = 0.115$ to $\mu_{\mathrm{poly}+GW}(350\ \mathrm{K}) = 0.143$. Finally, we note that the temperature dependence of the effective masses is well reproduced by a single ZG polymorphous configuration derived from the MSS structure, as indicated by the open circles in Fig. 9(u).

J. $\mathrm{FAPbBr_3}$

In this section, we describe our calculations for cubic $\mathrm{FAPbBr_3}$. Table I reports a DFT-PBEsol average band gap of 0.46 eV for the reference structure. Similar to $\mathrm{FAPbI_3}$, positional polymorphism leads to a relatively small band gap opening of 0.24 eV, consistent with the relative small degree of structural disorder calculated for FA-based compounds, as shown in Figs. 2(c)–2(h). Combining the PBE0 functional and the reference structures, we obtain a band gap of 1.89 eV, which underestimates the experimental value of 2.29 at 300 K [56]. Using locally disordered polymorphous networks, the calculated band gap increases to 2.13 eV, matching closer the experimental value. Previous *GW* calculations on ferroelectric monomorphous structures that exhibit an artificial Rashba splitting on the electronic structure yield band gaps of 2.20 and 2.26 eV [101,178].

Our calculated DFT-PBEsol effective masses for the reference structure are $m^*_\mathrm{h,ref} = 0.10$ and $m^*_\mathrm{e,ref} = 0.10$. Local disorder enhances the effective masses, resulting to $m^*_\mathrm{h,poly} = 0.16$ and $m^*_\mathrm{e,poly} = 0.15$, and thus to $\lambda_\mathrm{h} = 0.6$ and $\lambda_\mathrm{e} = 0.5$. These enhancements increase the reduced effective mass of cubic $\mathrm{FAPbBr_3}$ from $\mu_\mathrm{ref} = 0.050$ to $\mu_\mathrm{poly} = 0.077$ improving the comparison with the experimental values for orthorhombic and tetragonal phases of 0.117 and 0.13 [154]. To further improve consistency with experimental values, we apply *GW* enhancements [106] of 72% and 93% to the DFT hole and electron effective masses, respectively, following the approach used for FAPbI3. This results in a reduced effective mass of $\mu_{\mathrm{poly}+GW} = 0.141$.

Now we study the anharmonic phonon dispersion of cubic $\mathrm{FAPbBr_3}$. We focus on temperatures around 270 K, where the cubic phase of $\mathrm{FAPbBr_3}$ becomes stable [56,180]. In Fig. 8(j), we present the converged ASDM phonon dispersion at 300 K (fourth iteration) in the energy range 0–20 meV. As shown in Fig. 14(b), this range is mostly associated with vibrations of the inorganic atoms. The phonons of the ferroelectric monomorphous structure exhibit strong instabilities [green in Fig. 8(j)], which are alleviated by using a reference structure and including self-energy corrections with the ASDM. The stabilized phonon frequencies at the Γ point are $\omega_{\mathrm{TO}_{1\text{–}4}} = 5.4\text{–}7.1$, $\omega_{\mathrm{TO}_{5\text{-}6}} = 9.7\text{–}10.0$, $\omega_{\mathrm{TO}_{7\text{–}8}} = 13.3\text{–}13.7$, $\omega_{\mathrm{LO}_1} = 5.5$, $\omega_{\mathrm{LO}_2} = 6.53$, $\omega_{\mathrm{LO}_3} = 12.9$, and $\omega_{\mathrm{LO}_4} = 18.8\,\mathrm{meV}$, as reported in Table II. These frequencies are comparable to those of $\mathrm{MAPbBr_3}$ and $\mathrm{CsPbBr_3}$ with main differences attributed to contributions from the A-site cations and their coupling with the inorganic sublattice. Our calculated LO phonon frequencies for cubic $\mathrm{FAPbBr_3}$ compare well with the experimental values: (i) 5.5, 13.1, and 22.2 meV, obtained from inelastic neutron scattering measurements on the orthorhombic phase [41], and (ii) 4.4 and 18.8 meV, derived from the analysis of PL sidebands of 4–17 nm nanocrystals at 5.5 K [172]. Additionally, Ref. [53] reports an effective phonon frequency of 15.3 meV, obtained by fitting an one-phonon Fröhlich coupling model to PL linewidths measured over the 10–370 K range. This value lies approximately midway between our calculated $\omega_{\mathrm{LO}_3} = 12.9\,\mathrm{meV}$ and $\omega_{\mathrm{LO}_4} = 18.8\,\mathrm{meV}$.

In Table I, we report for the ZG reference and ZG polymorphous structures a thermal-induced band gap renormalization of $\Delta E_\mathrm{g,ref}(300\,\mathrm{K}) = 0.13\,\mathrm{eV}$ and $\Delta E_\mathrm{g,poly}(300\,\mathrm{K}) = 0.10\,\mathrm{eV}$. Using the reported thermal-induced mass corrections, Δm^*, we obtain the following enhancements factors: $\lambda_\mathrm{h,ref}(300\,\mathrm{K}) = 0.4$, $\lambda_\mathrm{e,ref}(300\,\mathrm{K}) = 0.3$ and $\lambda_\mathrm{h,poly}(300\,\mathrm{K}) = 0.3$, $\lambda_\mathrm{e,poly}(300\,\mathrm{K}) = 0.3$. The small changes in both ΔE_g and λ are consistent with the relatively small degree of local disorder in cubic $\mathrm{FAPbBr_3}$.

In Fig. 9(r), we present temperature-dependent band gaps of the ZG reference (open squares) and ZG polymorphous (black discs) structures of cubic $\mathrm{FAPbBr_3}$ evaluated as Boltzmann-weighted averages over 10 configurations. Our DFT calculations are corrected by $\Delta_s = 1.50\,\mathrm{eV}$ to align with the experimental data from Ref. [56] (gray triangles); Δ_s is close our PBE0 correction of 1.43 eV obtained for the polymorphous structure (see Table I). Using ZG reference structures leads to a temperature-induced band gap widening, but the calculated values consistently underestimate the experimental band gap by more than 0.20 eV across all temperatures. This discrepancy is resolved by employing ZG polymorphous structures. The temperature coefficient of the band gap, calculated as $dE_\mathrm{g}/dT = 6.6\times10^{-4}\,\mathrm{eV/K}$ for the reference structures, overestimates the extracted experimental value of 4.9×10^{-4} eV/K by approximately 35%. As shown in Figs. 10(a) and 10(b), both $dE_g/dT|_{\text{EPC}}$ and $dE_g/dT|_{\text{TE}}$ contribute to the band gap opening with temperature, with electron-phonon coupling accounting for 54% of the total effect in the reference case. The use of ZG polymorphous networks reduces both contributions, particularly that from electron-phonon interactions, leading now to a dominant thermal expansion contribution of 66%. The total slope obtained with ZG polymorphous structures is improved to $dE_g/dT = 3.6\times10^{-4}$ eV/K, underestimating the experimental value by 27%. Notably, the single ZG polymorphous configuration of the MSS structure [open circles in Fig. 9(r)] yields excellent agreement with experiment, with an extracted slope of 4.9×10^{-4} eV/K.

Figure 9(v) presents the temperature dependence of hole and electron effective masses in the range 275–400 K, calculated for both the ZG reference (open squares) and ZG polymorphous (black discs) networks of FAPbBr_3. The extracted slopes are $\lambda^T_{\text{h,ref}} = 1.8\times10^{-4}$, $\lambda^T_{\text{e,ref}} = 1.5\times10^{-4}$ and $\lambda^T_{\text{h,poly}} = 1.9\times10^{-4}$, $\lambda^T_{\text{e,poly}} = 1.5\times10^{-4}$/K. These values indicate that local disorder has small influence on the temperature dependence of the effective masses. Unlike the case of the band gap, the temperature-induced enhancement of the effective masses is primarily driven by electron-phonon coupling, which accounts for over 75% of the total effect in both structural models. For polymorphous cubic FAPbBr_3, the reduced effective mass increases from $\mu_{\text{poly}}(275\text{ K}) = 0.096$ to $\mu_{\text{poly}}(400\text{ K}) = 0.107$. Applying *GW* correction factors of 72% and 93% to the DFT hole and electron effective masses [106] yields corrected values of $\mu_{\text{poly}+GW}(275\text{ K}) = 0.175$ and $\mu_{\text{poly}+GW}(400\text{ K}) = 0.195$. Finally, we note that a single ZG polymorphous configuration derived from the MSS structure [open circles in Fig. 9(v)] provides a reasonable approximation for estimating the effective masses of FAPbBr_3.

K. FASnI_3

We next discuss our results for cubic FASnI_3. Similar to CsSnI_3 and MASnI_3, our DFT-PBEsol calculations yield a semimetallic behavior for the reference structures of FASnI_3, with a band gap of 0.11 eV as reported in Table I. However, in this case we did not observe an exchange in orbital character between the band extrema. Including local disorder leads to a band gap opening of 0.31 eV of similar magnitude with other FA-based compounds. This value is consistent with the 0.22 eV band gap opening previously reported by some of us for a single locally disordered configuration of cubic FASnI_3, calculated without including spin-orbit coupling [29]. Experimental measurements on FASnI_3 nanocrystals with cubic symmetry (space group $Pm\bar{3}m$) have reported a band gap increase of 190 meV compared to the corresponding bulk cubic phase [29]. In addition to quantum confinement, this increase has been attributed to local structural disorder, specifically to an average Sn-I-Sn bond angle reduction of 13° relative to the idealized cubic configuration. This angular deviation is 3° larger than that found in our locally disordered bulk structures, corresponding to an additional band gap renormalization of approximately 72 meV, based on the 24 meV/° slope shown in Fig. 2(d). We therefore attribute roughly 72 meV of the total 190 meV band gap increase to enhanced local disorder in cubic FASnI_3 nanocrystals, with the remaining contribution arising from quantum confinement or other effects. Our PBE0 calculations for the bulk reference structures give a band gap of 1.13 eV which compares well with the experimental value of 1.38 eV at 300 K [57], both reported in Table I. Employing locally disordered networks results to a band gap of 1.48 eV, which agrees with the experimental value. We note that *GW* calculations using an unphysical distorted monomorphous structure [101] report a band gap of 1.24 eV.

The DFT-PBEsol hole and electron effective masses of the reference structures are extremely small: $m^*_{\text{h,ref}} = 0.03$ and $m^*_{\text{e,ref}} = 0.03$. Local disorder increase the hole and electron effective masses to $m^*_{\text{h,poly}} = 0.08$ and $m^*_{\text{e,poly}} = 0.11$, which remain small close to those reported for MASnI_3. The adjustments due to local disorder correspond to effective mass enhancement factors of $\lambda_{\text{h}} = 1.7$ and $\lambda_{\text{e}} = 2.7$ and an increase in the reduced effective mass from $\mu_{\text{ref}} = 0.015$ to $\mu_{\text{poly}} = 0.046$.

Now we examine the anharmonic phonon dispersion of cubic FASnI_3. The cubic phase of FASnI_3 is observed above 250 K [57,180] and therefore we perform calculations around this value. In Fig. 8(k), we show the anharmonic phonon dispersion at 300 K in the energy range of 0–15 meV, which is found to converge by the third ASDM iteration, alleviating all phonon instabilities present in the monomorphous structure. The stabilized phonon frequencies at the Γ point are $\omega_{\text{TO}_{1-4}} = 4.93$–$5.8$, $\omega_{\text{TO}_{5-6}} = 6.7$–$6.8$, $\omega_{\text{TO}_{7-8}} = 12.1$–$12.6$, $\omega_{\text{LO}_1} = 4.98$, $\omega_{\text{LO}_2} = 5.24$, $\omega_{\text{LO}_3} = 11.3$, and $\omega_{\text{LO}_4} = 15.0$ meV, as reported in Table II. The calculated frequencies are comparable to those obtained for CsSnI_3 and MASnI_3 [Figs. 8(c) and 8(g)], with the primary differences arising from the influence of the A-site cations and their interactions with the inorganic sublattice. Furthermore, the phonon dispersions of FASnI_3 [Fig. 8(k)] and FAPbI_3 [Fig. 8(i)] are qualitatively and even quantitatively similar across large regions of the Brillouin zone. We attribute this to the fact that many vibrational modes are dominated by the motion of I atoms, despite the difference in B-site cations. This also supports the good agreement between our calculated phonon frequencies for cubic FASnI_3 and experimental measurements reported for FAPbI_3 [40,41,53], reported in Table II.

In Fig. 9(s), we show the band gap of cubic FASnI_3 as a function of temperature. The black discs and open squares correspond to Boltzmann-averaged band gaps calculated from 10 distinct ZG polymorphous configurations and their respective ZG reference structures. Temperature-dependent band gaps obtained from a single ZG polymorphous configuration, derived from the MSS structure, are shown as open circles. Our DFT values are shifted by $\Delta_s = 0.85$ eV to match the experimental data [57] (gray triangles). This shift is close to our computed PBE0 correction of 1.06 eV obtained for the polymorphous structures and the *GW* correction of 0.79 eV obtained for tetragonal MASnI_3 in Ref. [99]. The band gaps of the ZG reference structures increase with temperature, yielding a temperature coefficient of $dE_g/dT = 7.9\times10^{-4}$ eV/K. This value compares reasonably well with the experimental coefficient of 10.6×10^{-4} eV/K but underestimates it by approximately 25%. A similar level of underestimation is observed when ZG polymorphous structures are used, with the extracted coefficient being $dE_g/dT = 8.0\times10^{-4}$ eV/K. Notably, a single ZG polymorphous configuration derived from the MSS structure yields results nearly identical to those obtained by averaging over 10 ZG configurations.

As shown in Figs. 10(a) and 10(b), both $dE_g/dT|_{\mathrm{EPC}}$ and $dE_g/dT|_{\mathrm{TE}}$ contribute to the temperature-induced band gap widening, with electron-phonon coupling being the dominant mechanism in the reference structures, accounting for 62%. Interestingly, local disorder reverses this trend, suppressing the electron-phonon coupling contribution while enhancing that of thermal expansion, which now dominates with 73%. An enhancement of thermal expansion contribution is also observed for $\mathrm{MASnI_3}$. Although thermal expansion leads to an overall increase in average bond lengths, which is associated with the band gap opening in halide perovskites [Fig. 2(c)], its effect is modulated by changes in the metal-halide-metal bond angles due to local disorder. For example, in cubic $\mathrm{FAPbI_3}$, our analysis suggests that local disorder leads to the increase of the Pb-I-Pb angles toward 180° with thermal expansion, partially offsetting the band gap opening expected from bond length increase. In contrast, in cubic $\mathrm{FASnI_3}$, local disorder leads to a larger deviation of Sn-I-Sn angles away from 180°, enhancing the band gap opening and, thus the thermal expansion contribution. This contrasting behavior can be attributed to the more pronounced stereochemical activity of the Sn $5s^2$ lone pairs [27,33], which favors asymmetric bonding under lattice expansion.

Figure 9(w) shows the temperature dependence of the hole and electron effective masses of cubic $\mathrm{FASnI_3}$ in the range 140–400 K. Linear fits to the data for the ZG reference (open squares) and ZG polymorphous (red discs) structures are $\lambda^T_{\mathrm{h,ref}} = 1.8\times10^{-4}$, $\lambda^T_{\mathrm{e,ref}} = 2.4\times10^{-4}$ and $\lambda^T_{\mathrm{h,poly}} = 1.9\times10^{-4}$, $\lambda^T_{\mathrm{e,poly}} = 2.4\times10^{-4}$ m_0/K. A single ZG polymorphous configuration obtained from the MSS structure [open circles in Fig. 9(w)] yields similar slopes but underestimates the values obtained from Boltzmann-weighted averages by about 0.01–0.02 m_0. Electron-phonon coupling in reference structures is the leading thermal effect, contributing to about 72% to the effective masses enhancements. This contribution is reduced to 50% when local disorder is taken into account with thermal expansion contributing equally. Similar to the band gap behavior, the increased thermal expansion contribution to the effective mass enhancement in locally disordered structures is attributed to the enhanced lone pair activity in Sn-based compounds, promoting greater Sn-I-Sn bond angle bending under lattice expansion. Finally we report that for ZG polymorphous structures, the reduced effective mass exhibits a linear temperature dependence, increasing from $\mu_{\mathrm{poly}}(200\ \mathrm{K}) = 0.053$ to $\mu_{\mathrm{poly}}(400\ \mathrm{K}) = 0.075$.

L. $\mathrm{FAPbCl_3}$

Here, we present our findings for cubic $\mathrm{FAPbCl_3}$. As reported in Table I, the average DFT-PBEsol band gap for the reference structures is 0.89 eV. Incorporating local disorder results in a moderate band gap widening of 0.28 eV. Hybrid functional calculations using PBE0 yield a band gap of 2.51 eV for the reference structures, which underestimates the experimental value of 2.91 eV [111]. The use of locally disordered networks improves the agreement, yielding a PBE0 band gap of 2.79 eV. Assuming also that the band gap of $\mathrm{FAPbCl_3}$ is similar to that of $\mathrm{MAPbCl_3}$ [101], our calculated value of 2.79 eV compares well with the experimental band gaps of 2.88 and 3.07 eV at 300 K reported for $\mathrm{MAPbCl_3}$ in Refs. [51,55].

The effective masses calculated for the reference structures are $m^*_{\mathrm{h,ref}} = 0.17$ and $m^*_{\mathrm{e,ref}} = 0.18$. Using locally disordered structures, the effective masses increase to $m^*_{\mathrm{h,poly}} = 0.23$ and $m^*_{\mathrm{e,poly}} = 0.25$. The associated hole and electron effective mass enhancement factors due to local disorder are $\lambda_{\mathrm{h}} = 0.35$ and $\lambda_{\mathrm{e}} = 0.39$, which are slightly lower than those of $\mathrm{MAPbCl_3}$ due to the reduced degree of local disorder in $\mathrm{FAPbCl_3}$. Corrections arising from polymorphism increase the reduced effective mass from $\mu_{\mathrm{ref}} = 0.087$ to $\mu_{\mathrm{poly}} = 0.120$. The latter value compares well with the average *GW* value of 0.159 reported for tetragonal $\mathrm{MAPbCl_3}$, falling within the expected accuracy of the calculations [100].

We next investigate phonon anharmonicity in $\mathrm{FAPbCl_3}$. The cubic phase of $\mathrm{FAPbCl_3}$ is stable above 200 K [181]; accordingly, all calculations are performed at temperatures above this value. Figure 8(l) presents the ASDM phonon dispersion at 300 K, converged by the third iteration, within the 0–30 meV energy range characteristic of vibrations in the inorganic lattice framework. The anharmonic phonon dispersion of $\mathrm{FAPbCl_3}$ has some similar features to those reported for $\mathrm{MAPbCl_3}$ [Fig. 8(h)] and $\mathrm{CsPbCl_3}$ [Fig. 8(d)]; for example, all span comparable energy ranges and exhibit an LO-TO splitting above 10 meV (see $\omega_{\mathrm{LO_4}}$ values in Table II). Differences primarily stem from A-site cations contributions and how they modulate the lattice dynamics through interactions with the metal-halide network. Table II reports the frequencies at the Γ point of $\mathrm{FAPbCl_3}$: $\omega_{\mathrm{TO_{1-2}}} = 7.56$–$7.62$, $\omega_{\mathrm{TO_{3-4}}} = 10.1$–$11.4$, $\omega_{\mathrm{TO_{5-6}}} = 12.4$–$12.9$, $\omega_{\mathrm{TO_{7-8}}} = 15.8$–$16.6$, $\omega_{\mathrm{LO_1}} = 7.64$, $\omega_{\mathrm{LO_2}} = 10.2$, $\omega_{\mathrm{LO_3}} = 15.5$, and $\omega_{\mathrm{LO_4}} = 25.8$ meV. These values are in good agreement with room-temperature infrared and THz-TDS spectroscopy measurements for $\mathrm{MAPbCl_3}$ [166,168], which report TO modes at 8.2 and 11.0 meV and LO modes at 8.7 and 27.9 meV, as well as LO modes at 8.2 and 12.4 meV.

Now we examine the effect of electron-phonon coupling and thermal expansion on the electronic structure. Table I reports the band gap renormalization calculated using ZG reference and ZG polymorphous networks which are $\Delta E_{g,\mathrm{ref}}(300\ \mathrm{K}) = 0.09$ eV and $\Delta E_{g,\mathrm{poly}}(300\ \mathrm{K}) = 0.03$ eV. The reported thermal-induced mass corrections, Δm^*, lead to the following enhancements factors: $\lambda_{\mathrm{h,ref}}(300\ \mathrm{K}) = 0.24$, $\lambda_{\mathrm{e,ref}}(300\ \mathrm{K}) = 0.22$ and $\lambda_{\mathrm{h,poly}}(300\ \mathrm{K}) = 0.22$, $\lambda_{\mathrm{e,poly}}(300\ \mathrm{K}) = 0.20$, slightly smaller than those reported for $\mathrm{MAPbCl_3}$.

In Fig. 9(t), we present temperature-dependent band gaps of cubic $\mathrm{FAPbCl_3}$ in the range 250–400 K calculated using 10 ZG reference (open squares) and their corresponding ZG polymorphous (black discs) structures. We also include band gaps computed with a single ZG polymorphous configuration obtained from the MSS structure (open cirles). To match the experimental value of 2.91 eV [111] at room temperature, we shift all DFT data by about $\Delta_s = 1.71$ eV, similar to the PBE0 correction of 1.82 eV obtained for the polymorphous structures (see Table I). Our data for the ZG reference structures show a band gap widening with temperature, with a temperature coefficient of $dE_g/dT = 5.3\times10^{-4}$ eV/K. Figures 10(a) and 10(b) show that both electron-phonon coupling and thermal expansion lead to an opening of the band gap of the ZG reference structures, with the thermal expansion being the leading contribution with 60%. When ZG polymorphous networks are employed, electron-phonon coupling is suppressed, consistent with trends observed in other FA-based compounds, while the thermal expansion contribution remains nearly unchanged. As a result, thermal expansion contribution to the total band gap renormalization is increased to 81%. The calculated temperature coefficient of the band gap for the ZG polymorphous structures is $dE_g/dT = 4.1\times10^{-4}$ eV/K, which aligns well with the experimental value of 3.2×10^{-4} eV/K reported for $CsPbCl_3$ [164]. In contrast, our calculations for $FAPbCl_3$ do not reproduce the nearly temperature independent band gap behavior observed in $MAPbCl_3$. Direct experimental measurements for $FAPbCl_3$ are needed to validate our predictions. We remark that using a single ZG polymorphous structure offers a reasonable approximation for evaluating the temperature dependence of the band gap in $FAPbCl_3$, giving a temperature coefficient of 5.3×10^{-4} eV/K.

Figure 9(x) shows the temperature dependence of the hole and electron effective masses of the ZG reference (open squares) and ZG polymorphous structures (black discs). In both cases, the effective masses exhibit a linear increase with temperature with gradients: $\lambda^T_{\mathrm{h,ref}} = 1.9\times10^{-4}$, $\lambda^T_{\mathrm{e,ref}} = 1.8\times10^{-4}$ and $\lambda^T_{\mathrm{h,poly}} = 1.9\times10^{-4}$, $\lambda^T_{\mathrm{e,poly}} = 2.4\times10^{-4}$ m_0/K, indicating that local disorder has little impact on the temperature variation of the effective masses. We remark that now electron-phonon coupling contribution dominates thermal-induced renormalization in all cases, being more than 63%. We also report that the reduced effective mass calculated for polymorphous cubic $FAPbCl_3$ varies linearly with temperature, being $\mu_{\mathrm{poly}}(250\text{ K}) = 0.136$ and $\mu_{\mathrm{poly}}(400\text{ K}) = 0.153$. Finally, we note that unlike the band gap, the ZG polymorphous configuration of the MSS structure is not a good approximation to explain the temperature variation of the effective masses [open circles in Fig. 9(x)].

V. GENERAL COMPARISON AND DISCUSSION

A. Electronic structure

In general, we find that the electronic structure modifications induced by polymorphism are critical for improving agreement between calculated and experimental values of band gaps and effective masses across all compounds. This conlusion aligns with previous work by Zhao *et al.* [26,85,94], who emphasized that, in perovskite systems, including oxides, variations in band gap often arise from structural polymorphism rather than strong electronic correlations alone. Furthermore, our findings suggest that accounting for local disorder in cubic phases is essential to prevent spurious semimetallic behavior in DFT calculations, especially for Pb- and Sn-based iodide perovskites, where such artifacts severely hinder electronic structure properties. Depending on the size of the A-site cation, which governs the available steric environment, local disorder induces an average band gap opening of 0.27, 0.46, and 0.61 eV; hole effective mass increase of 0.06, 0.12, and 0.18 m_0; electron effective mass increase of 0.07, 0.11, and 0.19 m_0 in FA-, MA-, and Cs-based compounds, respectively. We, thus, identify local disorder as one of the main factors determining the band gap and effective mass ordering in $APbI_3$ and $APbBr_3$ halide perovskites, where Cs-based compounds exhibit the largest band gaps and effective masses, followed by MA- and FA-based systems. In contrast, for Sn-based and Cl-based compounds, additional factors, such as thermal expansion as well as lone pair expression and excitonic effects, respectively, play an important role.

Improved treatment of electronic correlations using PBE0 calculations combined with polymorphous structures yields overall good agreement with experimental band gap values, as shown in Table I. The calculated band gaps exhibit an average absolute deviation of 0.11 eV from experimental values. Including thermal-induced corrections $[\Delta E_{\mathrm{g,poly}}(T)]$ further improves agreement in some cases, but increases the discrepancy in others, resulting in a slightly higher average absolute deviation of 0.12 eV. Moreover, our PBE0 values compare well with *GW* calculations for the tetragonal and orthorhombic phases, which incorporate the effect of octahedral tilting. In future work, it would be interesting to explore how the combination of state-of-the-art *GW* calculations using cubic polymorphous structures and thermal-induced corrections compares with experiments. We emphasize that polymorphism is also essential for improving agreement with experimental values of the reduced effective masses, as shown in Table I. In this case, *GW* calculations are also expected to play an important role in achieving better quantitative accuracy. We observe that for the reduced effective masses of Pb-based compounds, the agreement with experiment decreases from Cs-based to MA-based, and further to FA-based compounds. For example, our values underestimate experimental data for $CsPbI_3$, $MAPbI_3$, and $FAPbI_3$ by 18%, 31%, and 48%, respectively. This trend aligns with the fact that compounds with larger cations exhibit smaller degree of polymorphism, and thus stronger electronic correlations.

B. Band gap across different polymorphs

As discussed in Secs. IV and V A, the band gaps obtained for the polymorphous cubic structures agree well with prior calculations on lower-symmetry polymorphs that explicitly incorporate octahedral tilts, i.e., the tetragonal and orthorhombic phases. Considering the monomorphous phases of $CsPbBr_3$, our calculations yield a DFT-PBEsol band gap of $E_g = 0.83$, 0.69, and 0.24 eV for the orthorhombic (Pnma), tetragonal (P4/mbm), and cubic ($Pm\bar{3}m$) phases, respectively. Assuming a monomorphous picture this trend is reasonable: larger octahedral tilts in the orthorhombic phase widen the gap relative to the tetragonal phase ($a^0a^0c^{\pm}$; no apical tilting) and, ultimately, to the untilted cubic phase. However, this ordering contradicts the measured band gap sequence in $CsPbBr_3$ [56], where $E_g(Pm\bar{3}m) > E_g(P4/mbm) > E_g(Pnma)$. The corresponding calculated band gaps using polymorphous structures are: $E_g = 0.83$, 0.86, and 0.85 eV for the orthorhombic, tetragonal, and cubic phases, respectively. This nearly recovers the expected trend (orthorhombic < tetragonal $\simeq$ cubic), compressing the spread to 0.03 eV. As shown in Ref. [30], adopting polymorphous rather than monomorphous structures and including thermal effects is crucial to capture the continuous increase of the band gap with temperature across different phases, avoiding spurious discontinuities at the phase boundaries. This suggests that reproducing the correct band gap ordering requires explicitly accounting for local structural disorder and finite-temperature effects, i.e., thermal lattice expansion and electron-phonon coupling.

A similar trend holds for $\mathrm{MAPbBr_3}$ [56]. Using monomorphous orthorhombic, reference tetragonal, and reference cubic structures of $\mathrm{MAPbBr_3}$, our DFT-PBEsol calculations yield $E_\mathrm{g} = 0.83$, 0.46, and 0.39 eV, respectively. In contrast, polymorphous tetragonal and cubic structures that capture local disorder give an almost phase-independent gap of $E_\mathrm{g} \simeq 0.83$ eV. Interestingly, representing the finite-temperature band gap with a ZG orthorhombic $\mathrm{MAPbBr_3}$ snapshot already provides a better description of the band gap at high temperatures than using ZG reference cubic cells [110].

For $\mathrm{MAPbI_3}$, the picture differs slightly. Monomorphous orthorhombic, reference tetragonal, and reference cubic structures give $E_\mathrm{g} = 0.61$, 0.29, and 0.03 eV, respectively, having a spread of 0.58 eV. Employing polymorphous tetragonal and cubic structures the corresponding band gaps are $E_\mathrm{g} = 0.61$, 0.51, and 0.52 eV, reducing the spread to 0.1 eV; this residual offset reflects the gap drop at the orthorhombic to tetragonal transition, not observed in $\mathrm{MAPbBr_3}$ [56]. This result is consistent with experimental observations for $\mathrm{MAPbI_3}$ [52,182] which report a band gap drop at the orthorhombic to tetragonal phase transition of about 0.1 eV and a nearly smooth evolution from the tetragonal to cubic phase transition.

C. LO-TO splitting

In the inorganic monomorphous $Pm\bar{3}m$ structures, the 12 optical phonons at the Brillouin zone center are grouped into four triply degenerate modes [183] prior to the inclusion of long-range dipole-dipole interactions. These comprise three infrared-active modes (Γ_4^-) and one silent mode (Γ_5^-). When LO-TO splitting is taken into account, our calculations show that three TO modes are doubly degenerate, while ω_{TO_2} retains its triply degenerate character, consistent with its assignment as the silent mode.

In Table II, we report in parenthesis the frequency of LO modes before LO-TO splitting for all compounds, each matching a value of the TO modes. Since the LO-TO splitting scales inversely with the atomic mass, materials incorporating lighter halides, such as Cl instead of Br or I, exhibit a more pronounced splitting related to the high energy LO mode. This effect arises from the stronger long-range restoring forces acting on the lighter ions, which elevate the LO frequency relative to the TO. As a result, compounds like $\mathrm{CsPbCl_3}$ show a larger LO-TO separation, e.g., 10.8 meV for ω_{LO_3}, compared to their heavier halide counterparts, such as $\mathrm{CsPbI_3}$, $\mathrm{CsPbBr_3}$, and $\mathrm{CsSnI_3}$, which show a splitting of 4.9, 6.5, and 6.2 meV, respectively. A similar picture holds for MA and FA-based compounds with different X-site anions.

The LO-TO splitting associated with the high energy LO mode is the smallest in FA-based perovskites. For example, the LO-TO splitting in $\mathrm{FAPbI_3}$ is 3.6 meV, in $\mathrm{MAPbI_3}$ is 5.8 meV, and in $\mathrm{CsPbI_3}$ is 4.9 meV. To rationalize this result we first use the simplified expression for the nonanalytic LO-TO splitting, $\Delta_{\mathrm{LO-TO}} \propto |Z^*|^2/L^3\epsilon^\infty$, where Z^* indicates the Born effective charges in units of elementary charge, ϵ^∞ is the high frequency dielectric constant, and L^3 is the volume of the cubic system. In view of the expression for $\Delta_{\mathrm{LO-TO}}$, one can expect $\mathrm{FAPbI_3}$ to exhibit a similar if not larger splitting among the A-site variants. This is based on the fact that $\mathrm{FAPbI_3}$ has relatively larger Born effective charges (e.g., $Z^*_{\mathrm{Pb}} = 4.72$, $Z^*_{\mathrm{I}} = 4.68$), a similar high-frequency dielectric constant ($\epsilon^\infty = 6.13$), and a similar lattice constant ($L = 6.36$ Å) compared to $\mathrm{MAPbI_3}$ (with $Z^*_{\mathrm{Pb}} = 4.59$, $Z^*_{\mathrm{I}} = 4.44$, $\epsilon^\infty = 5.87$, and $L = 6.31$ Å) and $\mathrm{CsPbI_3}$ (with $Z^*_{\mathrm{Pb}} = 4.49$, $Z^*_{\mathrm{I}} = 4.17$, $\epsilon^\infty = 5.75$, and $L = 6.25$ Å). Nonetheless, our density functional perturbation theory calculations show that $\mathrm{FAPbI_3}$ exhibits the smallest LO-TO splitting among the three compounds. This contradiction indicates that the simplified expression does not capture the full microscopic picture [184], as it neglects the phonon mode character, dipole directionality, and mode mixing. We ascribe the reduced LO-TO splitting in $\mathrm{FAPbI_3}$ to enhanced mode mixing between polar optical phonons and internal molecular vibrations [Fig. 14(c)], as well as directional coupling effects that diminish the effective dipole strength of the LO mode.

D. Overdamped phonon dynamics

In general, the calculated phonon energies at the zone center, reported in Table II, show good agreement with measurements obtained from various experimental techniques. However, our anharmonic phonon dispersions (Fig. 8) are based on reference structures and the quasiparticle approximation, and therefore neglect vibrational correlations arising from local structural disorder. As demonstrated in Ref. [30] for inorganic halide perovskites, local disorder gives rise to strongly overdamped and interacting vibrational modes, with only acoustic phonons near the Γ point remaining clearly identifiable. This picture, for example, aligns with several experimental observations: (i) inelastic neutron scattering measurements in hybrid halide perovskites revealing the absence of well-defined optical phonon modes across the entire energy range, attributed to strong overdamping at all momenta [41]; (ii) Raman spectra of both inorganic and hybrid halide perovskites displaying a pronounced central peak over a broad frequency range, indicative of correlated polar vibrations [38]; (iii) infrared transmission measurements showing highly overdamped vibrational modes lacking distinct quasiparticle features [170]; and (iv) THz time-domain spectroscopy pointing to damping of LO phonons due to mode coupling [168].

In Fig. 11, we present phonon spectral functions of all compounds calculated as an average over 10 polymorphous structures in 2×2×2 supercells in conjunction with the phonon unfolding technique; for more computational details see Sec. VI G. We focus on energy windows associated mostly with vibrations of the inorganic sublattice. Similar to findings of Ref. [30], the phonon spectral functions of all cubic phases reveal that acoustic phonons emerge from a sea of strongly correlated optical vibrations across the entire Brillouin zone. This picture, emerging from our quasistatic polymorphous

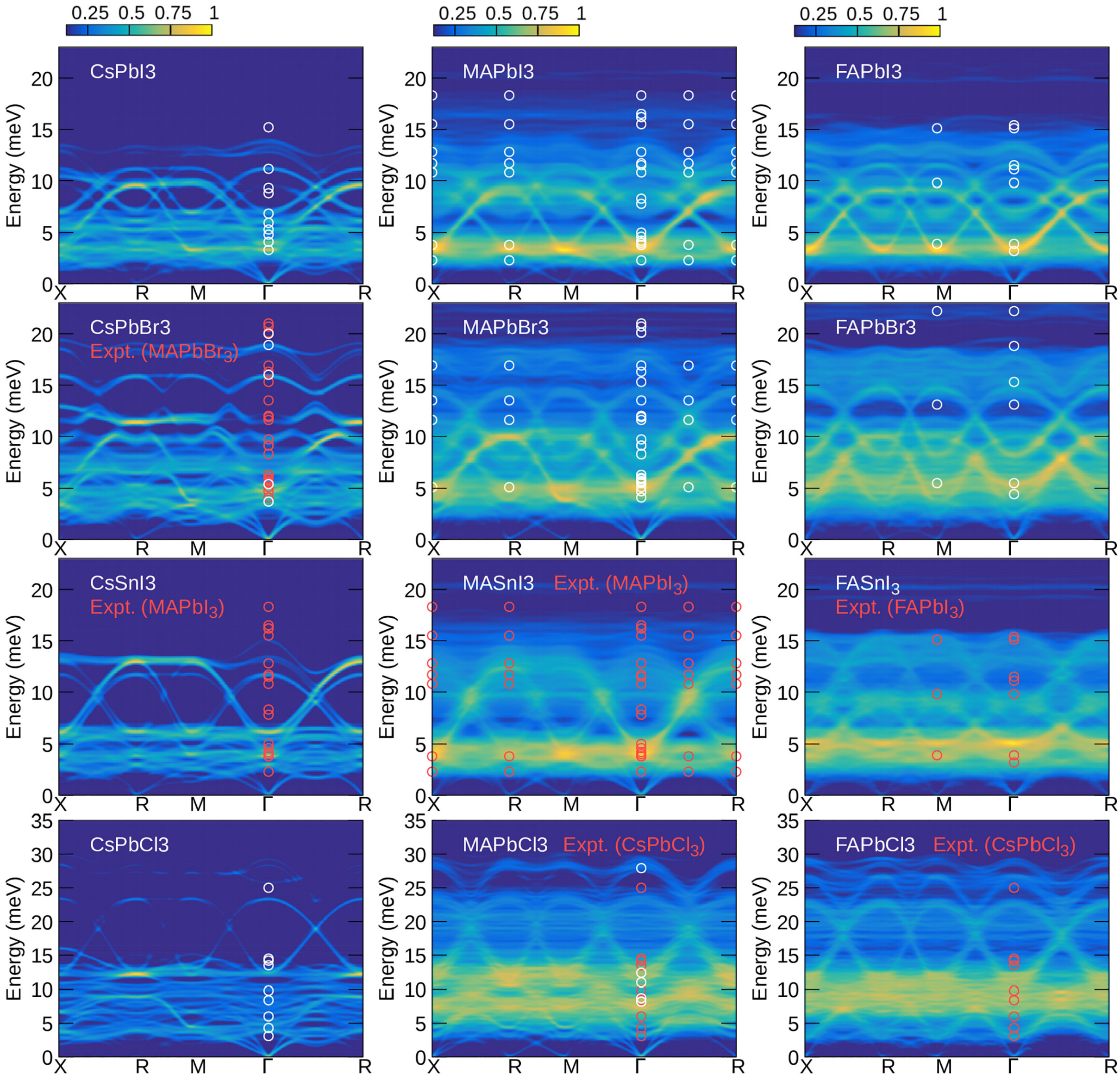

FIG. 11. Phonon spectral functions (color map) of inorganic and hybrid halide perovskites computed by phonon band unfolding [30]. Calculations represent averages over spectral functions computed for 10 polymorphous configurations of each compound. Open white circles denote experimental data from various techniques, as listed in Table II. Open red circles indicate experimental data from other compounds, as specified in each plot. For MAPbI$_3$, MAPbBr$_3$, FAPbI$_3$, and FAPbBr$_3$ we include phonon energies at the X, R, M, and mid Γ-R high-symmetry points obtained from neutron scattering measurements [41].

approach, is inconsistent with the translational diffusion characteristics of a liquid [185], as it preserves well-defined transverse acoustic phonons despite the presence of strong anharmonicity. Qualitatively, Fig. 11 shows that the degree of phonon overdamping varies with the A-site cation, being strongest in FA-based compounds, followed by MA-based, and weakest in Cs-based halide perovskites. This conclusion is also supported by low-frequency Raman spectra reported for CsPbBr$_3$ and MAPbBr$_3$ [38]. Furthermore, hybrid halide perovskites exhibit strongly correlated vibrational dynamics extending across a broad energy range, including high-energy optical modes. In contrast, overdamped phonons in Cs-based compounds are primarily confined to lower energies, typically below 10 meV. We attribute the greater extent of phonon overdamping in hybrid halide perovskites to the presence of molecular vibrational modes and their coupling to the vibrations of the inorganic sublattice accross a larger energy range.

In Fig. 11, we also compare our calculated phonon spectral functions with measurements of phonon energies at the Γ point from various techniques and samples, as reported in Table II. We additionally include neutron scattering data for MAPbI$_3$, MAPbBr$_3$, FAPbI$_3$, and FAPbBr$_3$ at the X, R, M, and mid Γ-R high-symmetry points from Ref. [41]. These data reveal nearly dispersionless optical vibrations with energies that remain constant across the Brillouin zone, an observation that is supported by our calculations. Furthermore, the highest spectral weights in the calculated phonon spectral functions are distributed around 5 meV for I-based and Br-based compounds, and around 10 meV for Cl-based compounds, in good agreement with various experimental phonon energies in this

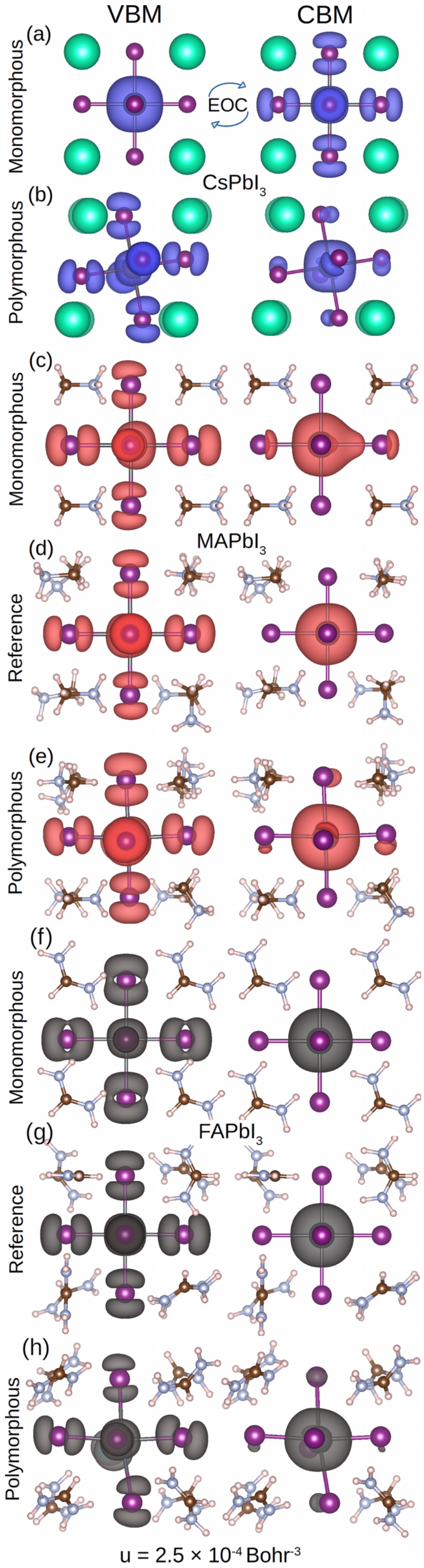

FIG. 12. (a)–(h) Charge densities at the valence band maximum (VBM) and conduction band minimum (CBM) of a single motif of the monomorphous, reference, and polymorphous $CsPbI_3$ (a), (b), $MAPbI_3$ (c)–(e), and $FAPbI_3$ (f)–(h). The isosurface value u is indicated at the bottom.

range. In general, we observe that incorporating structural disorder allows us to more accurately capture the variations observed in experimental data across different sample types, such as thin films, single crystals, polycrystalline pellets, nanocrystals, and nanocrystal films, where deviations from idealized reference structures, significantly influence phonon behavior leading to extensive broadening and phonon frequencies shifts. We remark that in some cases, especially for high energy modes, the spectral function peaks either overestimate or underestimate experimental data which we attribute to (i) the DFT functional used for computing IFCs, (ii) different lattice constants, (iii) the supercell size used to simulate local disorder, (iv) the temperature and perovskite phases considered in the experiment, and (v) the sample used for the measurements, e.g., thin films, single crystals, pellets, and nanocrystals. We note that, for example, in the case of nanocrystals other factors affect the phonon energy measurements, such as quantum confinement, dielectric screening, shape and surface effects, as well as the enhanced local disordered discussed in Sec. IV K.

E. Thermal-induced renormalization

We have seen that thermal-induced corrections are strongly modified for most cubic compounds in the presence of local disorder. As shown in Fig. 10(a), electron-phonon contribution is strongly suppressed for all compounds, with the largest reductions found for Cs-based compounds which exhibit the largest degree of local disorder. The only case where electron-phonon coupling contributes negatively to the temperature coefficient of the band gap leading to a band gap closing is $MAPbCl_3$. We attribute this to the fact that $MAPbCl_3$ exhibits one of the highest degrees of local disorder among the hybrid halide perovskites, reaching levels comparable to those of Cs-based compounds (Figs. 2(b) and 2(c) of Ref. [110]). The opposing effects of electron-phonon coupling and thermal expansion in polymorphous cubic $MAPbCl_3$ lead to the nearly constant variation of the band gap with temperature, consistent with experiments.

Thermal expansion contribution to the band gap renormalization is also reduced due to polymorphism for most compounds, especially for Cs-based compounds [Fig. 10(b)]. Thermal expansion increases the bond lengths, which tends to open the band gap in halide perovskites as shown in Fig. 2(c). However, this effect is also influenced by how the bond angles change upon allowing the structure to explore local disorder. For example, in cubic $FAPbI_3$ and most of the compounds studied here, local disorder causes the Pb-I-Pb angles to open toward 180°, which reduces the band gap opening due to thermal expansion. In contrast, in $FASnI_3$, the Sn-I-Sn angles bend more, enhancing the gap opening, as shown in Fig. 10(b). This difference comes from the stronger lone pair stereochemical expression of Sn as compared to Pb.

In general, we observe that the electron-phonon coupling percentage contribution depends on the choice of the A-site cation and decreases from Cs-based to MA-based, and further to FA-based compounds. In particular, electron-phonon coupling is the dominant contribution to the band gap renormalization in Cs-based and MA-based polymorphous compounds, except from $MAPbCl_3$, reaching as high as 97%.

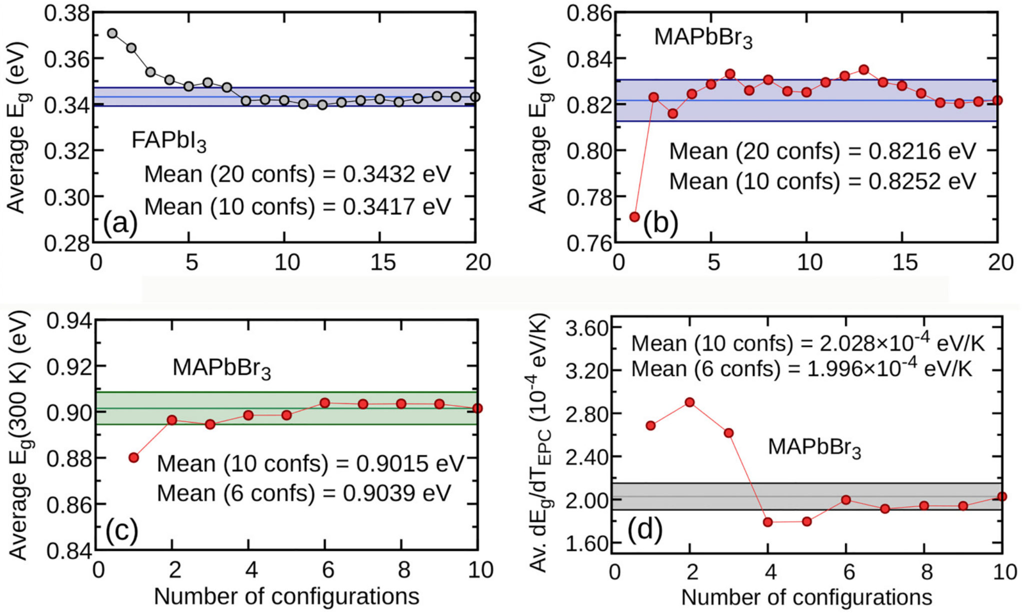

FIG. 13. (a), (b) Convergence test of the average DFT-PBEsol band gap of cubic $FAPbI_3$ (a) and $MAPbBr_3$ (b) as a function of the number of polymorphous configurations. (c) Convergence test of the average DFT-PBEsol band gap of cubic $MAPbBr_3$ at 300 K [Eq. (11)] as a function of the number of ZG polymorphous configurations. Average values for 10 configurations are converged within 5 meV. (d) Convergence test of the average band gap temperature coefficient due to electron-phonon coupling as a function of the number of ZG polymorphous configurations used to compute the band gap of $MAPbBr_3$ at each temperature. The temperature coefficient is calculated by fitting data points for the five temperatures shown in Fig. 7(c). The shaded regions represent the standard error of the mean on either side of the lines.

For FA-based compounds, except for $FAPbI_3$, the dominant contribution to the band gap renormalization is thermal expansion reaching as high as 81%. We attribute this to the relatively larger thermal expansion coefficients for the FA-based cubic phases [180,186,187] varying from $0.58–0.68\times10^{-4}\,K^{-1}$, while for MA-based compounds [175,180,186–189] from $0.33–0.54\times10^{-4}\,K^{-1}$ and for Cs-based compounds [25,54,164,188] from $0.29–0.51\times10^{-4}\,K^{-1}$.

Our results for the total temperature coefficients of the band gap using ZG polymorphous structures compare well with the experimental values, as shown quantitatively in Fig. 10(c) and Figs. 9(a)–9(d), 9(i)–9(l), and 9(q)–9(t). Importantly, we have seen that even using a single ZG polymorphous configuration obtained from the MSS structure is a good approximation for capturing the temperature variation of the band gap. We also find that thermal-induced corrections lead to a linear variation of the effective masses with temperature [Figs. 9(e)–9(h), 9(m)–9(p), and 9(u)–9(x)]. In $APbI_3$ and $APbBr_3$ compounds, the hole effective masses remain larger than the electron effective masses, whereas in $ASnI_3$ and $APbCl_3$ compounds, electron effective masses remain larger than hole effective masses. We note that our finite-temperature calculations: (i) rely on a constant temperature phonon approximation, (ii) neglect nonadiabatic effects in electron-phonon renormalization of the band structure [190–192], (iii) neglect many-body quasiparticle corrections to the electronic structure [122,193,194], and (iv) omit phonon renormalization due to thermal expansion. While including these effects may improve quantitative agreement with experiment, we do not expect them to alter the qualitative trends, as our current results already show good overall agreement.

VI. COMPUTATIONAL DETAILS

A. Electronic structure calculations

DFT calculations were performed using `Quantum ESPRESSO` (QE) [195,196]. We employed optimized norm-conserving Vanderbilt pseudopotentials from the PseudoDojo library [197,198] and the Perdew-Burke-Ernzerhof exchange-correlation functional revised for solids (PBEsol) [199]. The lattice constants (L) of all cubic phases, reported in Table I, were fixed close to their experimental values [25,54,164,175,180,186–189]. Calculations for the monomorphous structures (5 atoms for inorganic and 12 atoms for hybrid halide perovskites) were performed using a plane wave cutoff energy of 120 Ry and 6×6×6 uniform **k** grids. For exploring reference and polymorphous cubic structures with the ASDM as described in Sec. II C, we performed geometry optimization in 2×2×2 supercells (40 atoms for inorganic and 96 atoms for hybrid halide perovskites), until residual forces per atom were below 3×10^{-4} eV/Å using a plane wave cutoff energy of 120 Ry and 3×3×3 uniform **k** grids. During geometry optimization the lattice constants were kept fixed. We note that for the reference structures of hybrid halide perovskites only the molecules were relaxed, while for the unique reference (monomorphous) structures of inorganic compounds no relaxation was performed as the residual forces were zero. For each inorganic halide perovskite, we generated 1 high-symmetry monomorphous structure and 10 polymorphous structures. For each hybrid halide perovskite, we generated 1 MSS reference structure and its corresponding polymorphous structure, as well as 10 reference structures obtained by relaxing molecules from random initial orientations and their corresponding polymorphous structures. To construct MSS structures for hybrid halide perovskites, we employed a 2×2×2 supercell and initially fixed the orientation of one molecular cation within a single unit cell. Under this supercell constraint, the remaining seven molecules were placed such that a subset of the original space group symmetries, corresponding to the P422 space group, was preserved. The band gap of each structure was obtained by including SOC effects via fully relativstic pseudopotentials and evaluating the energy difference between the conduction band minimum and valence band maximum at the R point. Convergence tests of the band gap of FAPbI_3 and MAPbBr_3 with respect to the number of polymorphous configurations are shown in Figs. 13(a) and 13(b).

To check whether DFT-SOC calculations for each structure yield an exchange of orbital character (EOC) we computed the charge densities of the band edges at the R point. In Figs. 12(a)–12(h), we present the computed charge densities for a single octahedron in the monomorphous, reference, and polymorphous cubic structures of CsPbI_3, MAPbI_3, and FAPbI_3. We find that using a monomorphous network of CsPbI_3 yields an EOC which is corrected upon using a polymorphous structure [Figs. 12(a) and 12(b)]. A similar behavior is observed for monomorphous CsSnI_3 as well as for monomorphous and reference MASnI_3. In Fig. 12(c), we observe for MAPbI_3 that using a monomorphous network with a single orientation for the MA cation results in an anisotropic charge density, especially around the Pb atom, in both the valence band maximum and conduction band minimum. This spurious directional distortion in the electronic charge density arises from the net dipole moment of the MA molecule. Using a reference structure within a 2×2×2 supercell and allowing the molecules to relax starting from random orientations alleviates the anisotropy in the charge density considerably, as shown in Fig. 12(d). The same picture is maintained when a polymorphous structure is used [Fig. 12(e)]. In Fig. 12(f), our calculations for monomorphous FAPbI_3 show a reduced anisotropy in the charge density compared to monomorphous MAPbI_3 due to the smaller dipole moment of the FA molecule. However, at the valence band maximum, the charge is more concentrated around the equatorial I atoms (those lying in the same plane as the FA molecules) compared to the apical ones. Using the reference and polymorphous structures [Figs. 12(g) and 12(h)], we observe a more uniform distribution of charge density around the I atoms.

PBE0 hybrid functional calculations [155,200] for the reference and polymorphous cubic structures were performed using the VASP code [201] within the projector augmented-wave formalism [202]. A plane-wave energy cutoff of 400 eV was used, and the Brillouin zone was sampled with a 2×2×2 uniform **k** grid.

Calculations for the monomorphous orthorhombic (Pnma) and tetragonal (P4/mbm) structures of CsPbBr_3 were performed using the unit cells containing 20 and 10 atoms, respectively, with uniform **k** grids of 3×3×2 and 4×4×6. We used lattice constants of ($a = 7.97$, $b = 8.40$, and $c = 11.64$ Å) and ($a = b = 5.73$, $c = 5.96$ Å) [30]. To obtain a polymorphous structure of tetragonal CsPbBr_3, we relaxed the atoms in a 2×2×2 supercell (80 atoms), which lowered the energy by 16 meV/f.u. relative to the monomorphous model. As shown in Ref. [30], exploring local disorder in the orthorhombic phase yields a negligible stabilization, consistent with the fact that the structure is already being at a minimum in the PES. Calculations for the orthorhombic (Pnma) MAPbI_3 and MAPbBr_3 were performed using the unit cell (48 atoms) and a 4×4×3 uniform **k** grid. We generated 10 reference and 10 polymorphous tetragonal structures of MAPbI_3 and MAPbBr_3 employing a 1×2×1 supercell (96 atoms) and a 3×2×3 uniform **k** grid. Lattice constants were fixed to their experimental values [203].

B. Phonon calculations

Harmonic phonons, high-frequency dielectric constants, and Born effective charges of the monomorphous structures in the unit cell were computed via density functional perturbation theory [114,195] using a 2×2×2 uniform **q** grid. To compute anharmonic effective IFCs within the SCP theory, we employed 2×2×2 MSS reference structures and the ASDM in conjunction with finite differences of 0.01 Å as implemented in `ZG.x` of `EPW` code [42,121]. We employed a plane wave energy cutoff of 100 Ry and a 3×3×3 uniform **k** grid. Full anharmonic phonon dispersions were obtained by diagonalizing the dynamical matrices at 400 equally spaced **q** points along the X-R-M-Γ-R path of the Brillouin zone, using Fourier-interpolated IFCs. To account for corrections on the anharmonic phonon dispersions due to long-range dipole-dipole interactions, we used high-frequency dielectric constants and Born effective charges computed for the polymorphous structures and the mixed-space approach described in Ref. [204]. The number of iterations at which fully converged ASDM phonon dispersions were obtained for the MSS reference structures are indicated in Fig. 8. Anharmonic phonons up to ASDM-2 were computed for the reference configurations of hybrid halide perovskites with random molecular orientations (80 configurations in total). These phonons were used to generate anharmonic special displacements in each reference and polymorphous structure for incorporating the effect of electron-phonon coupling (see Sec. VI E).

To determine the percentage contribution of the molecule (PCM) to the ASDM phonon dispersions shown in Fig. 14, we used the computed phonon polarization vectors at each **q** point and phonon branch ν with the following expression:

$$\text{PCM}(\nu, \mathbf{q}) = \sum_{\kappa \in \text{mol}, \alpha} |e_{\kappa\alpha,\nu}(\mathbf{q})|^2 \Bigg/ \sum_{\kappa, \alpha} |e_{\kappa\alpha,\nu}(\mathbf{q})|^2 \times 100. \quad (12)$$

We note that the orientation of the first molecule in the MSS structure affects the phonon dispersion, as certain high-symmetry points in the Brillouin zone become inequivalent. To assess this effect, Fig. 15 shows the phonon dispersion of MAPbI_3 along paths passing through the three inequivalent M points. While the overall dispersions are similar, subtle variations are observed, with the most pronounced differences occurring for the ultrasoft flat band along the R-M direction. We note that this low energy band does not play an important role in the electron-phonon renormalization of the band gap [110].

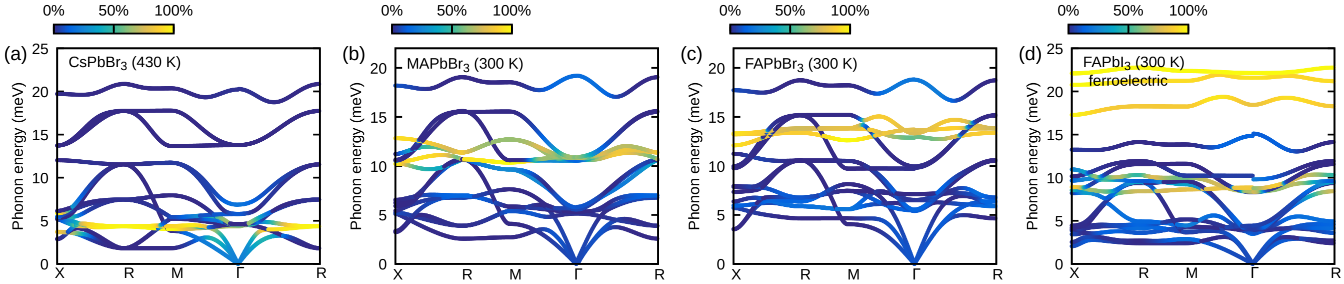

FIG. 14. (a) Percentage contribution of Cs atom to the ASDM phonon dispersion of CsPbBr$_3$ calculated using the high-symmetry monomorphous structure. (b), (c) Percentage contribution of the organic sublattice to the ASDM phonon dispersion of MAPbBr$_3$ (b) and FAPbBr$_3$ (c) in the range 0–20 meV calculated using MSS reference structures. (d) Percentage contribution of the organic sublattice to the ASDM phonon dispersion of FAPbI$_3$ in the range 0–25 meV calculated using the ferroelectric monomorphous network. All ASDM calculations refer to 2×2×2 supercells and the temperatures specified in each plot. All phonon dispersions include long-range dipole-dipole interaction corrections, leading to LO-TO splitting.

C. Diffuse scattering

One-phonon diffuse scattering maps of MAPbBr$_3$, shown in Fig. 6, were computed using `disca.x` of EPW [121,146,205]. The Debye-Waller factors at each scattering wave vector $\mathbf{Q}$ were evaluated for a $30\times30\times30$ $\mathbf{q}$ grid using phonon polarization vectors and frequencies obtained by Fourier interpolation of the effective IFCs computed at 300 K with ASDM for 2×2×2 supercells. A $30\times30\times1$ uniform $\mathbf{Q}$ grid per Brillouin zone together with the computed Debye-Waller factors were used to calculate the one-phonon diffuse scattering intensity in reciprocal lattice planes perpendicular to the Cartesian z axis. Parameters from Ref. [206] were used to model the atomic scattering amplitudes as a sum of Gaussians.

D. Effective masses

Effective masses were computed at the DFT level including SOC and by evaluating the diagonal components of the effective mass tensor via finite differences [207], followed by an isotropic average. That is we used the second-order finite difference formula based on the energies at the R point and nearby $\mathbf{k}$ points ($|\Delta\mathbf{k}| = 0.01\ 2\pi/\alpha$) along each Cartesian direction. The effective mass enhancement factors due to polymorphism were determined as $\lambda = m^*_{\rm poly}/m^*_{\rm ref} - 1$ and due to thermal effects as $\lambda(T) = [m^* + \Delta m^*(T)]/m^* - 1$. The reduced effective masses were evaluated as $\mu = m^*_{\rm h} m^*_{\rm e}/(m^*_{\rm h} + m^*_{\rm e})$. The slopes describing the temperature variation of the effective masses are denoted by λ^T.

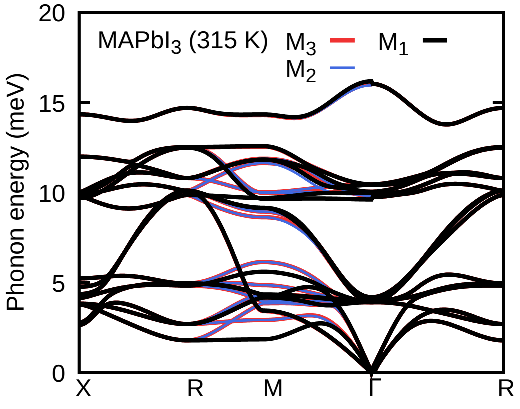

FIG. 15. ASDM phonon dispersion of the MSS reference structure of MAPbI$_3$ calculated for the three inequivalent M points: $M_1 = [0.5\ 0.5\ 0.0]$, $M_2 = [0.5\ 0.0\ 0.5]$, $M_3 = [0.0\ 0.5\ 0.5]$.

E. Electron-phonon calculations

To account for electron-phonon coupling effects at various temperatures, we employed special displacements (or ZG displacements) [109] generated via Eq. (6) for 4×4×4 supercells. We considered a constant temperature approximation for the phonons, i.e., anharmonic phonons computed at a specific temperature for each material (specified in Fig. 8), and the resulting vibrational modes were thermally populated at various temperatures to generate special displacements. We applied the special displacements on the nuclei of both the reference and polymorphous structures leading to the ZG reference and ZG polymorphous structures. We note that the initial 4×4×4 reference and polymorphous structures (containing 320 atoms for inorganic and 768 atoms for hybrid halide perovskites) were constructed by replicating the corresponding structures obtained in 2×2×2 supercells. SOC was included in all electron-phonon coupling calculations. To reduce computational cost, the plane wave energy cutoff was set to 60 Ry. Convergence tests performed on a subset of materials (MAPbBr$_3$, FAPbBr$_3$, FAPbI$_3$, and MASnI$_3$) using 2×2×2 supercells showed that the band gap values differ by less than 1 meV compared to calculations with a 120 Ry cutoff. Furthermore, the Brillouin zone of the 4×4×4 supercell was sampled using a 1×1×1 $\mathbf{k}$ grid. In this case, we found for the same subset of materials that the band gap varied by less than 10 meV and the thermal-induced renormalization by less than 1 meV. Figure 13(c) further shows that the band gap of MAPbBr$_3$ at 300 K is already well converged with 6 ZG polymorphous configurations.

To determine the contribution of electron-phonon coupling to the band gap renormalization and effective masses ($dE_{\rm g}/dT|_{\rm EPC}$ and $dm^*/dT|_{\rm EPC}$), we applied linear fits to the data points of each material computed at various temperatures without considering the effect of thermal expansion. Each data point was obtained as a Boltzmann-weighted average

[Eq. (11)] over the band gap of 10 ZG reference or 10 ZG polymorphous structures. Figure 13(d) shows the convergence of $dE_g/dT|_{\mathrm{EPC}}$ computed for MAPbBr$_3$ as a function of the number of ZG polymorphous configurations used to compute the band gap for each temperature.

Electron-phonon renormalized band gaps of MAPbBr$_3$ in the orthorhombic phase, reported in the companion paper [110], were computed using the special displacement method in conjunction with harmonic phonons. Calculations employed a 4×2×2 supercell of the orthorhombic unit cell (768 atoms), a cutoff of 80 Ry, and a 1×1×1 **k** grid, with SOC effects included.

F. Thermal expansion contribution

To evaluate the contribution of thermal expansion to the temperature dependence of the band gap, $dE_g/dT|_{\mathrm{TE}}$, and effective masses, $dm^*/dT|_{\mathrm{TE}}$, we employed the following strategy for each material: (i) The lattice constants of the initial 10 reference and 10 polymorphous 2×2×2 supercells were varied by $\Delta L = \pm 0.04$ Å. (ii) For each modified lattice, geometry optimizations were performed while keeping the lattice constants fixed, yielding new reference and polymorphous configurations. (iii) Band gaps and effective masses were computed for each individual structure, and averaged over the set of configurations corresponding to the same lattice constant. (iv) The derivatives dE_g/dL and dm^*/dL were estimated by fitting a linear function to the computed averaged values at $L - \Delta L$, L, and $L + \Delta L$, equivalent to a central finite difference approximation. (v) Experimental values of the linear thermal expansion coefficient, $\alpha = 1/L\, dL/dT$, of each material were taken from the literature [25,54,164,175,180,186–189]. Due to the absence of experimental data for FAPbCl$_3$, we used $\alpha = 0.6\times10^{-4}\ \mathrm{K}^{-1}$ close to the value reported for MAPbCl$_3$ [187]. (vi) Finally, the thermal expansion contributions for each material were evaluated using the relations

$$\left.\frac{dE_g}{dT}\right|_{\mathrm{TE}} = \frac{dE_g}{dL}\,\alpha L \quad \text{and} \tag{13}$$

$$\left.\frac{dm^*}{dT}\right|_{\mathrm{TE}} = \frac{dm^*}{dL}\,\alpha L. \tag{14}$$

G. Phonon spectral functions

Phonon spectral functions of the polymorphous structures shown in Fig. 11 were obtained by phonon unfolding using the approach described in Ref. [30] and the `ZG.x` code of EPW [121]. We used the IFCs calculated for the polymorphous structures without enforcing any translational or rotational symmetries of the unit cell or the reference structures. Based on the computed eigenvectors, which reflect spatial correlations introduced by local disorder, we determined the spectral weights of each configuration using 394 equally spaced **q** points along the the X-R-M-Γ-R path of the Brillouin zone. Convergence of the spectral weights was achieved by using a 12×12×12 **g** grid of reciprocal lattice vectors.

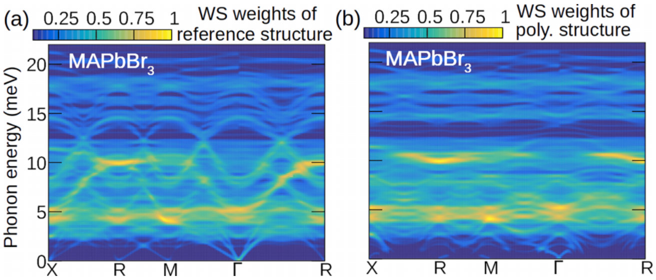

FIG. 16. (a), (b) Phonon spectral functions of one polymorphous configuration of MAPbBr$_3$ calculated using phonon unfolding in conjunction with Wigner-Seitz (WS) weights computed for the reference (a) and polymorphous (b) structures.

To obtain the phonon spectral functions of the polymorphous structures using the computed IFCs, we employed Wigner-Seitz (WS) weights calculated for the reference structures. These weights are used to determine whether a given interatomic vector lies within the WS cell, ensuring that each real-space interaction is counted once and contributes correctly to the phonon properties. Using the WS weights of the reference structure ensures that each atomic interaction is correctly weighted according to the macroscopic symmetry of the lattice. In Figs. 16(a) and 16(b), we compare the phonon spectral function of polymorphous cubic MAPbBr$_3$ calculated using WS weights of the reference and polymorphous structure, respectively. The results show that using the WS weights of the reference structure (i) maintains the overdamped and correlated character of the optical phonons and (ii) plays an important role in stabilizing the acoustic phonons, particularly near the Γ point, where long-wavelength behavior is sensitive to translational invariance. In other words, using the WS weights of the reference structure ensures that the acoustic sum rule is satisfied and accurately capture bulk-like lattice dynamics without compromising the overall behavior of the optical modes. This approach is particularly suitable for systems where disorder represents localized perturbations rather than fundamental changes to the macroscopic structure.

VII. CONCLUSIONS AND OUTLOOK

Based on the ASDM, we developed a unified methodology for electronic structure, anharmonicity, and electron-phonon coupling calculations in locally disordered inorganic and hybrid halide perovskites. We carried out a comparative high-throughput study of 12 cubic compounds and analyzed the modifications due to local disorder to their electronic structures with and without thermal effects. In addition to generating polymorphous structures, we also investigated reference configurations obtained by relaxing only the molecular sublattice, to minimize artifacts arising from net dipole moments, particularly relevant for MA-based compounds, and to enable systematic comparisons with the fully polymorphous structures. Our calculations reveal strong correlations between band gap widening and effective mass enhancement with structural distortions, such as changes in bond angles and lengths, induced by positional polymorphism. We further demonstrate that the extent of positional polymorphism is strongly influenced by the size of the A-site cation, a trend that correlates with the tolerance factor [110], where lower values typically indicate increased structural flexibility and a greater propensity for local distortions. We also show the critical role of local disorder in explaining the experimentally observed band gap variations across different phases.

We calculated phonon quasiparticle dispersions of MSS reference structures at finite temperatures within the SCP theory, and validated our results through comparison with experimental measurements of Γ point phonon frequencies and phonon-induced diffuse scattering. We examined the influence of A-site cation size on LO-TO splitting, showing that larger molecular cations, like FA, result in a less pronounced LO-TO splitting. This arises due to the enhanced coupling between the organic and inorganic sublattices. Furthermore, we demonstrated the breakdown of the phonon quasiparticle picture due to local disorder, leading to strongly correlated and dispersionless optical vibrations, consistent with state-of-the-art inelastic neutron scattering, Raman, and THz spectroscopy measurements [38,41,157,168,170]. Hybrid halide perovskites exhibit more strongly overdamped phonons over a broader energy range than their fully inorganic counterparts, which we attribute to the enhanced coupling between the molecular and inorganic network.

We evaluated the temperature dependence of band gaps and effective masses using both ZG reference structures and ZG polymorphous structures for all cubic compounds, taking into account configurational entropy effects. For the band gaps, we achieved excellent agreement with experimental values, highlighting the importance of incorporating corrections due to positional polymorphism, exchange-correlation treatments beyond standard DFT, anharmonic electron-phonon coupling, and thermal expansion to accurately reproduce experimental trends. We further quantified the contributions of electron-phonon coupling and thermal expansion to the temperature-induced band gap renormalization, showing that electron-phonon coupling dominates in Cs-based and MA-based compounds, whereas thermal expansion plays the leading role in FA-based systems. This behavior is attributed to the larger volumetric thermal expansion coefficients of FA-based compounds. In the case of locally disordered $\mathrm{FASnI_3}$, we found that the stereochemically active Sn lone pair enhances the thermal expansion contribution, which primarily accounts for the largest temperature coefficient of the band gap among the materials studied. Finally, we showed that even a single ZG polymorphous configuration, generated from the MSS structure and ASDM phonons, yields results comparable to Boltzmann-weighted averages over 10 ZG polymorphous configurations.

The strong correlations observed between local disorder and electronic properties indicate that band gap tuning and charge transport in halide perovskites are intrinsically linked to local structural fluctuations. This finding suggests that engineering local disorder, through strategies such as A-site cation selection or strain, could enable systematic optimization of the optoelectronic performance of these materials. We emphasize that our approach is readily applicable to mixed-halide perovskites and will be valuable in future studies exploring how A-site, B-site, or X-site mixing influences positional polymorphism and, in turn, electronic structure. We anticipate that our methodology will complement recent experimental efforts [29,31,33,35,46,91] aimed at elucidating local structural features not only in three-dimensional halide perovskites, but also in layered hybrid perovskites and nanocrystals. Furthermore, our theoretical framework will aid in gaining a deeper understanding of the fundamental limitations of the carrier transport (lifetimes and diffusion lengths) at elevated temperatures. It will also help understanding the decoherence limits for the spins of single charge carriers, particularly for bulk materials, or for excitons, which are more relevant for quantum dots. Both phenomena may be crucial: on the one hand, for spin transport in spintronic applications and, on the other hand, for single-photon emission in quantum optics applications [208,209].

To our knowledge, this is the first report of anharmonic quasiparticle phonon dispersions in hybrid halide perovskites, validated against experimental measurements. The anharmonic, temperature-dependent IFCs, along with the corresponding reference and polymorphous structures, which are available in the NOMAD repository [210], provide a foundation for state-of-the-art perturbative electron-phonon calculations [114–122] in cubic hybrid halide perovskites. These calculations can help elucidate key phenomena such as charge carrier mobilities [62,211], polaron formation [80], as well as nonequilibrium dynamics [212]. Furthermore, our finding that a single ZG polymorphous configuration within a 4×4×4 supercell provides an excellent approximation for nonperturbative electron-phonon calculations holds promise for extending this approach to large-scale, high-throughput studies across other hybrid halide perovskite systems.

We emphasize that machine learning force fields (MLFFs) [185,211,213,214] offer significant potential for advancing anharmonic phonon calculations and the exploration of polymorphous structures. However, the development of more systematic and efficient training protocols may be necessary to capture the complexity and long-range correlated positional polymorphism in hybrid halide perovskites using larger supercells. Furthermore, MLFFs can help effectively assess approximations in our electron-phonon calculations, such as the constant temperature phonon anharmonicity and the neglect of phonon renormalization due to thermal expansion.

In addition, our calculations revealing the breakdown of the phonon quasiparticle picture in both inorganic and hybrid halide perovskites are expected to be of significant interest to recent experimental spectroscopy and scattering studies [25,38,40,41,157,168,170,215]. Our results demonstrate that structural disorder, whether originating from surface effects, grain boundaries, or finite-size confinement, is intrinsic to single crystals, thin films, nanocrystals, polycrystalline pellets, and nanocrystal-based films, and must be taken into account to accurately describe the experimentally observed phonon behavior in these systems. Spectroscopic and scattering techniques, when complemented by first-principles calculations that explicitly include local disorder, offer a powerful framework not only for understanding the extremely overdamped phonons in ultrasoft halide perovskites, but also for elucidating the microscopic origins of their ultralow thermal conductivity [216–218].

Our comparative study underscores the critical role of data in materials science, particularly when include thermal effects and positional polymorphism. Capturing such effects is essential for generating datasets that reflect a more realistic material behavior which is vital for training machine learning models to discover reliable descriptors and trends for finite-temperature properties. These insights also open a path toward more predictive and transferable models for data-driven materials discovery.

A database of monomorphous, reference, and polymorphous structures of halide perovskites, together with input and output files that led to the results of this study, is available in the NOMAD repository [210].

ACKNOWLEDGMENTS

This research was funded by the European Union (Project ULTRA-2DPK/HORIZON-MSCA-2022-PF-01/Grant Agreement No. 101106654). Views and opinions expressed are however those of the authors only and do not necessarily reflect those of the European Union or the European Commission. Neither the European Union nor the granting authority can be held responsible for them. We thank D. R. Ceratti for graciously providing data on temperature-dependent band gaps of Br-based hybrid halide perovskite single crystals. J.E. acknowledges financial support from the Institut Universitaire de France. F.G. was supported by the the Robert A. Welch Foundation under Award No. F-2139-20230405 and by the National Science Foundation under DMREF Grant No. 2119555. G.V. acknowledges funding from the ANR through the CPJ program and the SURFIN project (Grant No. ANR-23-CE09-0001), the ALSATIAN project (Grant No. ANR-23-CE50-0030), and the ANR under the France 2030 programme, MINOTAURE project (Grant No. ANR-22-PETA-0015). We acknowledge that the results of this research have been achieved using computational resources from the EuroHPC Joint Undertaking and supercomputer LUMI [219], hosted by CSC (Finland) and the LUMI consortium through a EuroHPC Extreme Scale Access call. Preliminary calculations were performed at FOTON Institute using HPC resources of TGCC/CINES under the allocation A0140911434, A0160911434, and A0180911434 made by GENCI.

DATA AVAILABILITY

The data that support the findings of this article are openly available [210].

---

[1] A. Kojima, K. Teshima, Y. Shirai, and T. Miyasaka, Organometal halide perovskites as visible-light sensitizers for photovoltaic cells, J. Am. Chem. Soc. **131**, 6050 (2009).

[2] H. Snaith, Perovskites: The emergence of a new era for low-cost, high-efficiency solar cells, J. Phys. Chem. Lett. **4**, 3623 (2013).

[3] M. Filip, G. Eperon, H. Snaith, and F. Giustino, Steric engineering of metal-halide perovskites with tunable optical band gaps, Nat. Commun. **5**, 5757 (2014).

[4] L. Protesescu, S. Yakunin, M. Bodnarchuk, F. Krieg, R. Caputo, C. Hendon, R. Yang, A. Walsh, and M. Kovalenko, Nanocrystals of cesium lead halide perovskites ($CsPbX_3$, X = Cl, Br, and I): Novel optoelectronic materials showing bright emission with wide color gamut, Nano Lett. **15**, 3692 (2015).

[5] G. Volonakis, M. Filip, A. Haghighirad, N. Sakai, B. Wenger, H. Snaith, and F. Giustino, Lead-free halide double perovskites via heterovalent substitution of noble metals, J. Phys. Chem. Lett. **7**, 1254 (2016).

[6] G. Eperon, T. Leijtens, K. Bush, R. Prasanna, T. Green, J. T.-W. Wang, D. McMeekin, G. Volonakis, R. Milot, R. May, *et al.*, Perovskite-perovskite tandem photovoltaics with optimized band gaps, Science **354**, 861 (2016).

[7] H. Tsai, W. Nie, J.-C. Blancon, C. Stoumpos, R. Asadpour, B. Harutyunyan, A. Neukirch, R. Verduzco, J. Crochet, S. Tretiak, *et al.*, High-efficiency two-dimensional Ruddlesden–Popper perovskite solar cells, Nature (London) **536**, 312 (2016).

[8] T. Brenner, D. Egger, L. Kronik, G. Hodes, and D. Cahen, Hybrid organic-inorganic perovskites: Low-cost semiconductors with intriguing charge-transport properties, Nat. Rev. Mater. **1**, 15007 (2016).

[9] G. Volonakis, A. Haghighirad, R. Milot, W. Sio, M. Filip, B. Wenger, M. Johnston, L. Herz, H. Snaith, and F. Giustino, $Cs_2InAgCl_6$: A new lead-free halide double perovskite with direct band gap, J. Phys. Chem. Lett. **8**, 772 (2017).

[10] L. Mao, W. Ke, L. Pedesseau, Y. Wu, C. Katan, J. Even, M. Wasielewski, C. Stoumpos, and M. Kanatzidis, Hybrid Dion–Jacobson 2D lead iodide perovskites, J. Am. Chem. Soc. **140**, 3775 (2018).

[11] J. Hoffman, X. Che, S. Sidhik, X. Li, I. Hadar, J.-C. Blancon, H. Yamaguchi, M. Kepenekian, C. Katan, J. Even, C. Stoumpos, A. Mohite, and M. Kanatzidis, From 2D to 1D electronic dimensionality in halide perovskites with stepped and flat layers using propylammonium as a spacer, J. Am. Chem. Soc. **141**, 10661 (2019).

[12] X.-K. Liu, W. Xu, S. Bai, Y. Jin, J. Wang, R. Friend, and F. Gao, Metal halide perovskites for light-emitting diodes, Nat. Mater. **20**, 10 (2021).

[13] E. Marchenko, S. Fateev, A. Petrov, V. Korolev, A. Mitrofanov, A. Petrov, E. Goodilin, and A. B. Tarasov, Database of two-dimensional hybrid perovskite materials: Open-access collection of crystal structures, band gaps, and atomic partial charges predicted by machine learning, Chem. Mater. **32**, 7383 (2020).

[14] A. Dey, J. Ye, A. De, E. Debroye, S. Ha, E. Bladt, A. S. Kshirsagar, Z. Wang, J. Yin, Y. Wang, *et al.*, State of the art and prospects for halide perovskite nanocrystals, ACS Nano **15**, 10775 (2021).

[15] M. Ahmadi, M. Ziatdinov, Y. Zhou, E. Lass, and S. Kalinin, Machine learning for high-throughput experimental exploration of metal halide perovskites, Joule **5**, 2797 (2021).

[16] P. Jiang, D. Acharya, G. Volonakis, M. Zacharias, M. Kepenekian, L. Pedesseau, C. Katan, and J. Even, Pb-free halide perovskites for solar cells, light-emitting diodes, and photocatalysts, APL Mater. **10**, 060902 (2022).

[17] T. J. Jacobsson, A. Hultqvist, A. García-Fernández, A. Anand, A. Al-Ashouri, A. Hagfeldt, A. Crovetto, A. Abate, A.

Ricciardulli, Vijayan, *et al.*, An open-access database and analysis tool for perovskite solar cells based on the FAIR data principles, Nat. Energy **7**, 107 (2021).

[18] E. Unger and T. J. Jacobsson, The perovskite database project: A perspective on collective data sharing, ACS Energy Lett. **7**, 1240 (2022).

[19] S. Sidhik, Y. Wang, M. De Siena, R. Asadpour, A. Torma, T. Terlier, K. Ho, W. Li, A. Puthirath, X. Shuai, *et al.*, Deterministic fabrication of 3D/2D perovskite bilayer stacks for durable and efficient solar cells, Science **377**, 1425 (2022).

[20] I. Metcalf, S. Sidhik, H. Zhang, A. Agrawal, J. Persaud, J. Hou, J. Even, and A. D. Mohite, Synergy of 3D and 2D perovskites for durable, efficient solar cells and beyond, Chem. Rev. **123**, 9565 (2023).

[21] S. Sidhik, I. Metcalf, W. Li, T. Kodalle, C. Dolan, M. Khalili, J. Hou, F. Mandani, A. Torma, H. Zhang, *et al.*, Two-dimensional perovskite templates for durable, efficient formamidinium perovskite solar cells, Science **384**, 1227 (2024).

[22] M. Filip and L. Leppert, Halide perovskites from first principles: From fundamental optoelectronic properties to the impact of structural and chemical heterogeneity, Electron. Struct. **6**, 033002 (2024).

[23] J. Even, M. Carignano, and C. Katan, Molecular disorder and translation/rotation coupling in the plastic crystal phase of hybrid perovskites, Nanoscale **8**, 6222 (2016).

[24] A. Beecher, O. Semonin, J. Skelton, J. Frost, M. Terban, H. Zhai, A. Alatas, J. Owen, A. Walsh, and S. J. Billinge, Direct observation of dynamic symmetry breaking above room temperature in methylammonium lead iodide perovskite, ACS Energy Lett. **1**, 880 (2016).

[25] A. Marronnier, G. Roma, S. Boyer-Richard, L. Pedesseau, J.-M. Jancu, Y. Bonnassieux, C. Katan, C. Stoumpos, M. Kanatzidis, and J. Even, Anharmonicity and disorder in the black phases of cesium lead iodide used for stable inorganic perovskite solar cells, ACS Nano **12**, 3477 (2018).

[26] X.-G. Zhao, G. Dalpian, Z. Wang, and A. Zunger, Polymorphous nature of cubic halide perovskites, Phys. Rev. B **101**, 155137 (2020).

[27] D. Fabini, R. Seshadri, and M. Kanatzidis, The underappreciated lone pair in halide perovskites underpins their unusual properties, MRS Bull. **45**, 467 (2020).

[28] B. Hehlen, P. Bourges, B. Rufflé, S. Clément, R. Vialla, A. C. Ferreira, C. Ecolivet, S. Paofai, S. Cordier, C. Katan, A. Létoublon, and J. Even, Pseudospin-phonon pretransitional dynamics in lead halide hybrid perovskites, Phys. Rev. B **105**, 024306 (2022).

[29] D. Dirin, A. Vivani, M. Zacharias, T. Sekh, I. Cherniukh, S. Yakunin, F. Bertolotti, M. Aebli, R. Schaller, A. Wieczorek, *et al.*, Intrinsic formamidinium tin iodide nanocrystals by suppressing the Sn(IV) impurities, Nano Lett. **23**, 1914 (2023).

[30] M. Zacharias, G. Volonakis, F. Giustino, and J. Even, Anharmonic electron-phonon coupling in ultrasoft and locally disordered perovskites, npj Comput. Mater. **9**, 153 (2023).

[31] N. Weadock, C. MacKeen, X. Qin, L. Waquier, Y. Rakita, J. Vigil, H. Karunadasa, V. Blum, M. Toney, and F. Bridges, Thermal contributions to the local and long-range structural disorder in $Ch_3Nh_3PbBr_3$, PRX Energy **2**, 033004 (2023).

[32] V. Diez-Cabanes, S. Giannini, D. Beljonne, and C. Quarti, On the origin of energetic disorder in mixed halides lead perovskites, Adv. Opt. Mater. **12**, 2301105 (2024).

[33] A. Balvanz, M. Safdari, M. Zacharias, D. Kim, C. Welton, E. Oriel, M. Kepenekian, C. Katan, C. Malliakas, J. Even, *et al.*, Structural evolution and photoluminescence quenching across the $FASnI_{3-}xBr_x$ ($x = 0$–3) perovskites, J. Am. Chem. Soc. **146**, 16128 (2024).

[34] S. Caicedo-Davila, A. Cohen, S. Motti, M. Isobe, K. McCall, M. Grumet, M. Kovalenko, O. Yaffe, L. Herz, D. Fabini, and D. Egger, Disentangling the effects of structure and lone-pair electrons in the lattice dynamics of halide perovskites, Nat. Commun. **15**, 4184 (2024).

[35] M. Dubajic, J. Neilson, J. Klarbring, X. Liang, S. Bird, K. Rule, J. Auckett, T. Selby, G. Tumen-Ulzii, Y. Lu, Y.-K. Jung, C. Chosy, Z. Wei, Y. Boeije, M. Zimmermann, A. Pusch, L. Gu, X. Jia, Q. Wu, J. Trowbridge, *et al.*, Dynamic nanodomains dictate macroscopic properties in lead halide perovskites, Nat. Nanotechnol. **20**, 755 (2025).

[36] C. Quarti, E. Mosconi, and F. De Angelis, Structural and electronic properties of organo-halide hybrid perovskites from *ab initio* molecular dynamics, Phys. Chem. Chem. Phys. **17**, 9394 (2015).

[37] M. Carignano, S. A. Aravindh, I. Roqan, J. Even, and C. Katan, Critical fluctuations and anharmonicity in lead iodide perovskites from molecular dynamics supercell simulations, J. Phys. Chem. C **121**, 20729 (2017).

[38] O. Yaffe, Y. Guo, L. Tan, D. Egger, T. Hull, C. Stoumpos, F. Zheng, T. F. Heinz, L. Kronik, M. Kanatzidis, J. Owen, A. Rappe, M. Pimenta, and L. Brus, Local polar fluctuations in lead halide perovskite crystals, Phys. Rev. Lett. **118**, 136001 (2017).

[39] C. Katan, A. Mohite, and J. Even, Entropy in halide perovskites, Nat. Mater. **17**, 377 (2018).

[40] M. Fu, P. Tamarat, J.-B. Trebbia, M. Bodnarchuk, M. Kovalenko, J. Even, and B. Lounis, Unraveling exciton–phonon coupling in individual $FAPbI_3$ nanocrystals emitting near-infrared single photons, Nat. Commun. **9**, 3318 (2018).

[41] A. C. Ferreira, S. Paofai, A. Létoublon, J. Ollivier, S. Raymond, B. Hehlen, B. Rufflé, S. Cordier, C. Katan, J. Even, and P. Bourges, Direct evidence of weakly dispersed and strongly anharmonic optical phonons in hybrid perovskites, Commun. Phys. **3**, 48 (2020).

[42] M. Zacharias, G. Volonakis, F. Giustino, and J. Even, Anharmonic lattice dynamics via the special displacement method, Phys. Rev. B **108**, 035155 (2023).

[43] A. Marronnier, H. Lee, B. Geffroy, J. Even, Y. Bonnassieux, and G. Roma, Structural instabilities related to highly anharmonic phonons in halide perovskites, J. Phys. Chem. Lett. **8**, 2659 (2017).

[44] R. Sutton, M. Filip, A. Haghighirad, N. Sakai, B. Wenger, F. Giustino, and H. Snaith, Cubic or orthorhombic? Revealing the crystal structure of metastable black-phase $CsPbI_3$ by theory and experiment, ACS Energy Lett. **3**, 1787 (2018).

[45] T. A. Doherty, S. Nagane, D. Kubicki, Y.-K. Jung, D. Johnstone, A. Iqbal, D. Guo, K. Frohna, M. Danaie, E. Tennyson, *et al.*, Stabilized tilted-octahedra halide perovskites inhibit local formation of performance-limiting phases, Science **374**, 1598 (2021).

[46] X. He, M. Krogstad, M. Gupta, T. Lanigan-Atkins, C. Mao, F. Ye, Y. Liu, T. Hong, S. Chi, H. Wei, *et al.*, Multiple lattice instabilities and complex ground state in $Cs_2AgBiBr_6$, PRX Energy **3**, 013014 (2024).

[47] C. Patrick, K. Jacobsen, and K. S. Thygesen, Anharmonic stabilization and band gap renormalization in the perovskite CsSnI$_3$, Phys. Rev. B **92**, 201205(R) (2015).

[48] C. Quarti, E. Mosconi, J. Ball, V. D'Innocenzo, C. Tao, S. Pathak, H. Snaith, A. Petrozza, and F. Angelis, Structural and optical properties of methylammonium lead iodide across the tetragonal to cubic phase transition: Implications for perovskite solar cells, Energy Environ. Sci. **9**, 155 (2016).

[49] J. Ning, L. Zheng, W. Lei, S. Wang, J. Xi, and J. Yang, Temperature-dependence of the band gap in the all-inorganic perovskite CsPbI$_3$ from room to high temperatures, Phys. Chem. Chem. Phys. **24**, 16003 (2022).

[50] S. Seidl, X. Zhu, G. Reuveni, S. Aharon, C. Gehrmann, S. Caicedo-Dávila, O. Yaffe, and D. Egger, Anharmonic fluctuations govern the band gap of halide perovskites, Phys. Rev. Mater. **7**, L092401 (2023).

[51] G. Maculan, A. Sheikh, A. Abdelhady, M. Saidaminov, M. Haque, B. Murali, E. Alarousu, O. Mohammed, T. Wu, and O. Bakr, CH$_3$NH$_3$PbCl$_3$ single crystals: Inverse temperature crystallization and visible-blind UV-photodetector, J. Phys. Chem. Lett. **6**, 3781 (2015).

[52] R. Milot, G. Eperon, H. Snaith, M. Johnston, and L. Herz, Temperature-dependent charge-carrier dynamics in CH$_3$NH$_3$PbI$_3$ perovskite thin films, Adv. Funct. Mater. **25**, 6218 (2015).

[53] A. Wright, C. Verdi, R. Milot, G. Eperon, M. Pérez-Osorio, H. Snaith, F. Giustino, M. Johnston, and L. Herz, Electron–phonon coupling in hybrid lead halide perovskites, Nat. Commun. **7**, 11755 (2016).

[54] A. Kontos, A. Kaltzoglou, M. Arfanis, K. McCall, C. Stoumpos, B. Wessels, P. Falaras, and M. G. Kanatzidis, Dynamic disorder, band gap widening, and persistent near-IR photoluminescence up to at least 523 k in ASnI$_3$ perovskites (A = Cs$^+$, CH$_3$NH$_3^+$ and NH$_2$-CH$^+$NH$_2^+$), J. Phys. Chem. C **122**, 26353 (2018).

[55] H.-P. Hsu, L.-C. Li, M. Shellaiah, and K. Sun, Structural, photophysical, and electronic properties of CH$_3$NH$_3$PbCl$_3$ single crystals, Sci. Rep. **9**, 13311 (2019).

[56] G. Mannino, I. Deretzis, E. Smecca, A. La Magna, A. Alberti, D. Ceratti, and D. Cahen, Temperature-dependent optical band gap in CsPbBr$_3$, MAPbBr$_3$, and FAPbBr$_3$ single crystals, J. Phys. Chem. Lett. **11**, 2490 (2020).

[57] S. Kahmann, O. Nazarenko, S. Shao, O. Hordiichuk, M. Kepenekian, J. Even, M. Kovalenko, G. Blake, and M. Loi, Negative thermal quenching in FASnI$_3$ perovskite single crystals and thin films, ACS Energy Lett. **5**, 2512 (2020).

[58] Y. Chen, Y. Lei, Y. Li, Y. Yu, J. Cai, M.-H. Chiu, R. Rao, Y. Gu, C. Wang, W. Choi, *et al.*, Strain engineering and epitaxial stabilization of halide perovskites, Nature (London) **577**, 209 (2020).

[59] J. Peters, Z. Liu, M. De Siena, M. Kanatzidis, and B. Wessels, Photoluminescence spectroscopy of excitonic emission in CsPbCl$_3$ perovskite single crystals, J. Lumin. **243**, 118661 (2022).

[60] C. Stoumpos, C. Malliakas, and M. G. Kanatzidis, Semiconducting tin and lead iodide perovskites with organic cations: Phase transitions, high mobilities, and near-infrared photoluminescent properties, Inorg. Chem. **52**, 9019 (2013).

[61] E. Parrott, R. Milot, T. Stergiopoulos, H. Snaith, M. Johnston, and L. Herz, Effect of structural phase transition on charge-carrier lifetimes and defects in CH$_3$NH$_3$SnI$_3$ perovskite, J. Phys. Chem. Lett. **7**, 1321 (2016).

[62] S. Poncé, M. Schlipf, and F. Giustino, Origin of low carrier mobilities in halide perovskites, ACS Energy Lett. **4**, 456 (2019).

[63] Lewis A. D. Irvine, A. Walker, and M. Wolf, Quantifying polaronic effects on the scattering and mobility of charge carriers in lead halide perovskites, Phys. Rev. B **103**, L220305 (2021).

[64] B. Cucco, J. Leveillee, V.-A. Ha, J. Even, M. Kepenekian, F. Giustino, and G. Volonakis, Intrinsic limits of charge carrier mobilities in layered halide perovskites, PRX Energy **3**, 023012 (2024).

[65] X.-Y. Zhu and V. Podzorov, Charge carriers in hybrid organic–inorganic lead halide perovskites might be protected as large polarons, J. Phys. Chem. Lett. **6**, 4758 (2015).

[66] J. Frost, Calculating polaron mobility in halide perovskites, Phys. Rev. B **96**, 195202 (2017).

[67] K. Miyata, D. Meggiolaro, M. T. Trinh, P. Joshi, E. Mosconi, S. Jones, F. De Angelis, and X.-Y. Zhu, Large polarons in lead halide perovskites, Sci. Adv. **3**, e1701217 (2017).

[68] S. Bretschneider, I. Ivanov, H. Wang, K. Miyata, X. Zhu, and M. Bonn, Quantifying polaron formation and charge carrier cooling in lead-iodide perovskites, Adv. Mater. **30**, 1707312 (2018).

[69] E. Cinquanta, D. Meggiolaro, S. Motti, M. Gandini, Marcelo J. P. Alcocer, Q. Akkerman, C. Vozzi, L. Manna, F. De Angelis, A. Petrozza, and S. Stagira, Ultrafast THz probe of photoinduced polarons in lead-halide perovskites, Phys. Rev. Lett. **122**, 166601 (2019).

[70] D. Ghosh, E. Welch, A. Neukirch, A. Zakhidov, and S. Tretiak, Polarons in halide perovskites: A perspective, J. Phys. Chem. Lett. **11**, 3271 (2020).

[71] N. Österbacka, P. Erhart, S. Falletta, A. Pasquarello, and J. Wiktor, Small electron polarons in CsPbBr$_3$: Competition between electron localization and delocalization, Chem. Mater. **32**, 8393 (2020).

[72] A. Srimath Kandada and Carlos Silva, Exciton polarons in two-dimensional hybrid metal-halide perovskites, J. Phys. Chem. Lett. **11**, 3173 (2020).

[73] M. Puppin, S. Polishchuk, N. Colonna, A. Crepaldi, D. N. Dirin, O. Nazarenko, R. De Gennaro, G. Gatti, S. Roth, T. Barillot, *et al.*, Evidence of large polarons in photoemission band mapping of the perovskite semiconductor CsPbBr$_3$, Phys. Rev. Lett. **124**, 206402 (2020).

[74] O. Cannelli, N. Colonna, M. Puppin, T. Rossi, D. Kinschel, L. M. Leroy, J. Löffler, J. Budarz, A. March, G. Doumy, *et al.*, Quantifying photoinduced polaronic distortions in inorganic lead halide perovskite nanocrystals, J. Am. Chem. Soc. **143**, 9048 (2021).

[75] B. Guzelturk, T. Winkler, T. W. Van de Goor, M. Smith, S. Bourelle, S. Feldmann, M. Trigo, S. Teitelbaum, H.-G. Steinrück, G. de la Pena, *et al.*, Visualization of dynamic polaronic strain fields in hybrid lead halide perovskites, Nat. Mater. **20**, 618 (2021).

[76] L. R. Buizza and L. Herz, Polarons and charge localization in metal-halide semiconductors for photovoltaic and light-emitting devices, Adv. Mater. **33**, 2007057 (2021).

[77] M. Schilcher, P. Robinson, D. Abramovitch, L. Tan, A. Rappe, D. Reichman, and D. Egger, The significance of polarons and

dynamic disorder in halide perovskites, ACS Energy Lett. **6**, 2162 (2021).

[78] H. Zhang, E. Debroye, J. Steele, M. B. Roeffaers, J. Hofkens, H. Wang, and M. Bonn, Highly mobile large polarons in black phase $CsPbI_3$, ACS Energy Lett. **6**, 568 (2021).

[79] X. Yue, C. Wang, B. Zhang, Z. Zhang, Z. Xiong, X. Zu, Z. Liu, Z. Hu, G. O. Odunmbaku, Y. Zheng, *et al.*, Real-time observation of the buildup of polaron in α-$FAPbI_3$, Nat. Commun. **14**, 917 (2023).

[80] J. Lafuente-Bartolome, C. Lian, and F. Giustino, Topological polarons in halide perovskites, Proc. Natl. Acad. Sci. USA **121**, e2318151121 (2024).

[81] M. Baranowski, A. Nowok, K. Galkowski, M. Dyksik, A. Surrente, D. Maude, M. Zacharias, G. Volonakis, S. Stranks, J. Even, M. Maczka, R. Nicholas, and P. Plochocka, Polaronic mass enhancement and polaronic excitons in metal halide perovskites, ACS Energy Lett. **9**, 2696 (2024).

[82] H. Zhang, W. Li, J. Essman, C. Quarti, I. Metcalf, W.-Y. Chiang, S. Sidhik, J. Hou, A. Fehr, A. Attar, *et al.*, Ultrafast relaxation of lattice distortion in two-dimensional perovskites, Nat. Phys. **19**, 545 (2023).

[83] H. Seiler, D. Zahn, V. C. Taylor, M. Bodnarchuk, Y. Windsor, M. Kovalenko, and R. Ernstorfer, Direct observation of ultrafast lattice distortions during exciton–polaron formation in lead halide perovskite nanocrystals, ACS Nano **17**, 1979 (2023).

[84] S. Biswas, R. Zhao, F. Alowa, M. Zacharias, S. Sharifzadeh, D. Coker, D. Seferos, and G. Scholes, Exciton polaron formation and hot-carrier relaxation in rigid Dion–Jacobson-type two-dimensional perovskites, Nat. Mater. **23**, 937 (2024).

[85] X.-G. Zhao, Z. Wang, O. Malyi, and A. Zunger, Effect of static local distortions vs. dynamic motions on the stability and band gaps of cubic oxide and halide perovskites, Mater. Today **49**, 107 (2021).

[86] Z. Wang, O. Malyi, X. Zhao, and A. Zunger, Mass enhancement in $3d$ and s-p perovskites from symmetry breaking, Phys. Rev. B **103**, 165110 (2021).

[87] C. Quarti, R. Gautier, M. Zacharias, A. Gansmuller, and C. Katan, Nuclear quadrupolar resonance structural characterization of halide perovskites and perovskitoids: A roadmap from electronic structure calculations for lead–iodide-based compounds, J. Am. Chem. Soc. **147**, 278 (2025).

[88] R. Comes, M. Lambert, and A. Guinier, The chain structure of $BaTiO_3$ and $KNbO_3$, Solid State Commun. **6**, 715 (1968).

[89] H. Mashiyama, Y. Kurihara, and T. Azestu, Disordered cubic perovskite structure of $CH_3NH_3PbX_3$ (X=Cl, Br, I), J. Korean Phys. Soc. **32**, S156 (1998).

[90] M. S. Senn, D. A. Keen, T. C. A. Lucas, J. A. Hriljac, and A. L. Goodwin, Emergence of long-range order in $BaTiO_3$ from local symmetry-breaking distortions, Phys. Rev. Lett. **116**, 207602 (2016).

[91] S. Sabisch, M. Aebli, A. Kanak, V. Morad, S. Boehme, M. Wörle, L. Feld, C. Copéret, and M. V. Kovalenko, Temperature-dependent ^{207}Pb nuclear magnetic resonance spectroscopy: A spectroscopic probe for the local electron. struct. of lead halide perovskites, Chem. Mater. **37**, 3443 (2025).

[92] Z. Wang, X.-G. Zhao, R. Koch, Simon J. L. Billinge, and A. Zunger, Understanding electronic peculiarities in tetragonal FeSe as local structural symmetry breaking, Phys. Rev. B **102**, 235121 (2020).

[93] Y. Wang, M. Zacharias, X. Zhang, N. Pant, J. Even, P. F. P. Poudeu, and E. Kioupakis, Efficient first-principles framework for overdamped phonon dynamics and anharmonic electron-phonon coupling in superionic materials, Phys. Rev. Lett. **135**, 056402 (2025).

[94] X.-G. Zhao, O. Malyi, and A. Zunger, Polymorphous nature of the local structure of δ-Bi_2O_3, Phys. Rev. Mater. **8**, 125403 (2024).

[95] L.-Y. Huang and W. R. L. Lambrecht, Electronic band structure, phonons, and exciton binding energies of halide perovskites $CsSnCl_3$, $CsSnBr_3$, and $CsSnI_3$, Phys. Rev. B **88**, 165203 (2013).

[96] J. Even, L. Pedesseau, J.-M. Jancu, and C. Katan, Importance of spin–orbit coupling in hybrid organic/inorganic perovskites for photovoltaic applications, J. Phys. Chem. Lett. **4**, 2999 (2013).

[97] J. Even, L. Pedesseau, J.-M. Jancu, and C. Katan, DFT and $k \cdot p$ modelling of the phase transitions of lead and tin halide perovskites for photovoltaic cells, Phys. Status Solidi **8**, 31 (2013).

[98] A. Amat, E. Mosconi, E. Ronca, C. Quarti, P. Umari, M. Nazeeruddin, M. Grätzel, and F. Angelis, Cation-induced band-gap tuning in organohalide perovskites: Interplay of spin–orbit coupling and octahedra tilting, Nano Lett. **14**, 3608 (2014).

[99] P. Umari, E. Mosconi, and F. De Angelis, Relativistic GW calculations on $CH_3NH_3PbI_3$ and $CH_3NH_3SnI_3$ perovskites for solar cell applications, Sci. Rep. **4**, 4467 (2014).

[100] E. Mosconi, P. Umari, and F. De Angelis, Electronic and optical properties of $MAPbX_3$ perovskites (X = I, Br, Cl): A unified DFT and GW theoretical analysis, Phys. Chem. Chem. Phys. **18**, 27158 (2016).

[101] M. Bokdam, T. Sander, A. Stroppa, S. Picozzi, D. D. Sarma, C. Franchini, and G. Kresse, Role of polar phonons in the photo excited state of metal halide perovskites, Sci. Rep. **6**, 28618 (2016).

[102] W. Saidi, S. Poncé, and B. Monserrat, Temperature dependence of the energy levels of methylammonium lead iodide perovskite from first-principles, J. Phys. Chem. Lett. **7**, 5247 (2016).

[103] L. Whalley, J. Frost, Y.-K. Jung, and A. Walsh, Perspective: Theory and simulation of hybrid halide perovskites, J. Chem. Phys. **146**, 220901 (2017).

[104] B. Traoré, G. Bouder, W. Lafargue-Dit-Hauret, X. Rocquefelte, C. Katan, F. Tran, and M. Kepenekian, Efficient and accurate calculation of band gaps of halide perovskites with the Tran-Blaha modified Becke-Johnson potential, Phys. Rev. B **99**, 035139 (2019).

[105] H. Ghaithan, Z. Alahmed, S. M. Qaid, M. Hezam, and A. Aldwayyan, Density functional study of cubic, tetragonal, and orthorhombic $CsPbBr_3$ perovskite, ACS Omega **5**, 7468 (2020).

[106] S. Wang, W.-B. Xiao, and F. Wang, Structural, electronic, and optical properties of cubic formamidinium lead iodide perovskite: A first-principles investigation, RSC Adv. **10**, 32364 (2020).

[107] Z. Muhammad, P. Liu, R. Ahmad, S. Jalali-Asadabadi, C. Franchini, and I. Ahmad, Revealing the quasiparticle elec-

tronic and excitonic nature in cubic, tetragonal, and hexagonal phases of FAPbI$_3$, AIP Adv. **12**, 025330 (2022).

[108] M. Zacharias and F. Giustino, One-shot calculation of temperature-dependent optical spectra and phonon-induced band-gap renormalization, Phys. Rev. B **94**, 075125 (2016).

[109] M. Zacharias and F. Giustino, Theory of the special displacement method for electronic structure calculations at finite temperature, Phys. Rev. Res. **2**, 013357 (2020).

[110] M. Zacharias, G. Volonakis, L. Pedesseau, C. Katan, F. Giustino, and J. Even, companion paper, Electron-phonon couplings in polymorphous crystals, Phys. Rev. B **113**, L081104 (2026).

[111] C. López, O. Fabelo, C. Abia, M. Fernández-Diaz, and J. A. Alonso, Crystal growth, structural phase transitions and optical gap evolution of FAPb(Br$_{1\text{-}x}$Cl$_x$)$_3$ hybrid perovskites (FA: formamidinium ion, CH(NH$_2$)$_2^+$), Discover Nano **20**, 6 (2025).

[112] A. Francisco-López, B. Charles, O. Weber, M. I. Alonso, M. Garriga, M. Campoy-Quiles, M. Weller, and A. Goñi, Equal footing of thermal expansion and electron–phonon interaction in the temperature dependence of lead halide perovskite band gaps, J. Phys. Chem. Lett. **10**, 2971 (2019).

[113] A. Rubino, A. Francisco-López, A. Barker, A. Petrozza, M. Calvo, A. Goñi, and H. Míguez, Disentangling electron–phonon coupling and thermal expansion effects in the band gap renormalization of perovskite nanocrystals, J. Phys. Chem. Lett. **12**, 569 (2021).

[114] S. Baroni, S. de Gironcoli, A. Dal Corso, and P. Giannozzi, Phonons and related crystal properties from density-functional perturbation theory, Rev. Mod. Phys. **73**, 515 (2001).

[115] F. Giustino, Electron-phonon interactions from first principles, Rev. Mod. Phys. **89**, 015003 (2017).

[116] D. Sangalli, A. Ferretti, H. Miranda, C. Attaccalite, I. Marri, E. Cannuccia, P. Melo, M. Marsili, F. Paleari, A. Marrazzo, G. Prandini, *et al.*, Many-body perturbation theory calculations using the Yambo code, J. Phys.: Condens. Matter **31**, 325902 (2019).

[117] X. Gonze, B. Amadon, G. Antonius, F. Arnardi, L. Baguet, J.-M. Beuken, J. Bieder, F. Bottin, J. Bouchet, E. Bousquet, *et al.*, The ABINITproject: Impact, environment and recent developments, Comput. Phys. Commun. **248**, 107042 (2020).

[118] M. Engel, M. Marsman, C. Franchini, and G. Kresse, Electron-phonon interactions using the projector augmented-wave method and Wannier functions, Phys. Rev. B **101**, 184302 (2020).

[119] J.-J. Zhou, J. Park, I.-T. Lu, I. Maliyov, X. Tong, and M. Bernardi, Perturbo: A software package for *ab initio* electron–phonon interactions, charge transport and ultrafast dynamics, Comput. Phys. Commun. **264**, 107970 (2021).

[120] H. Yang, M. Govoni, A. Kundu, and G. Galli, Computational protocol to evaluate electron–phonon interactions within density matrix perturbation theory, J. Chem. Theory Comput. **18**, 6031 (2022).

[121] H. Lee, S. Poncé, K. Bushick, S. Hajinazar, J. Lafuente-Bartolome, J. Leveillee, C. Lian, J.-M. Lihm, F. Macheda, H. Mori, *et al.*, Electron–phonon physics from first principles using the EPW code, npj Comput. Mater. **9**, 156 (2023).

[122] Z. Li, G. Antonius, Y.-H. Chan, and S. Louie, Electron-phonon coupling from *GW* perturbation theory: Practical workflow combining BerkeleyGW, ABINIT, and EPW, Comput. Phys. Commun. **295**, 109003 (2024).

[123] A. Franceschetti, First-principles calculations of the temperature dependence of the band gap of Si nanocrystals, Phys. Rev. B **76**, 161301(R) (2007).

[124] B. Monserrat, Electron–phonon coupling from finite differences, J. Phys.: Condens. Matter **30**, 083001 (2018).

[125] J. Wiktor, U. Rothlisberger, and A. Pasquarello, Predictive determination of band gaps of inorganic halide perovskites, J. Phys. Chem. Lett. **8**, 5507 (2017).

[126] M. Zacharias, M. Scheffler, and C. Carbogno, Fully anharmonic nonperturbative theory of vibronically renormalized electronic band structures, Phys. Rev. B **102**, 045126 (2020).

[127] P. Allen and V. Heine, Theory of the temperature dependence of electronic band structures, J. Phys. C: Solid State Phys. **9**, 2305 (1976).

[128] P. B. Allen and M. Cardona, Theory of the temperature dependence of the direct gap of germanium, Phys. Rev. B **23**, 1495 (1981).

[129] D. J. Hooton, LI. A new treatment of anharmonicity in lattice thermodynamics: I, London Edinburgh Philos. Mag. J. Sci. **46**, 422 (1955).

[130] P. Souvatzis, O. Eriksson, M. I. Katsnelson, and S. P. Rudin, Entropy driven stabilization of energetically unstable crystal structures explained from first principles theory, Phys. Rev. Lett. **100**, 095901 (2008).

[131] S. Brown, I. Georgescu, and V. A. Mandelshtam, Self-consistent phonons revisited. II. A general and efficient method for computing free energies and vibrational spectra of molecules and clusters, J. Chem. Phys. **138**, 044317 (2013).

[132] O. Hellman, I. A. Abrikosov, and S. I. Simak, Lattice dynamics of anharmonic solids from first principles, Phys. Rev. B **84**, 180301(R) (2011).

[133] O. Hellman, P. Steneteg, I. A. Abrikosov, and S. I. Simak, Temperature dependent effective potential method for accurate free energy calculations of solids, Phys. Rev. B **87**, 104111 (2013).

[134] I. Errea, M. Calandra, and F. Mauri, Anharmonic free energies and phonon dispersions from the stochastic self-consistent harmonic approximation: Application to platinum and palladium hydrides, Phys. Rev. B **89**, 064302 (2014).

[135] T. Tadano, Y. Gohda, and S. Tsuneyuki, Anharmonic force constants extracted from first-principles molecular dynamics: Applications to heat transfer simulations, J. Phys.: Condens. Matter **26**, 225402 (2014).

[136] T. Tadano and S. Tsuneyuki, Self-consistent phonon calculations of lattice dynamical properties in cubic SrTiO$_3$ with first-principles anharmonic force constants, Phys. Rev. B **92**, 054301 (2015).

[137] L. Monacelli, R. Bianco, M. Cherubini, M. Calandra, I. Errea, and F. Mauri, The stochastic self-consistent harmonic approximation: Calculating vibrational properties of materials with full quantum and anharmonic effects, J. Phys.: Condens. Matter **33**, 363001 (2021).

[138] A. van Roekeghem, J. Carrete, and N. Mingo, Quantum self-consistent *ab-initio* lattice dynamics, Comput. Phys. Commun. **263**, 107945 (2021).

[139] A. Isihara, The Gibbs-Bogoliubov inequality dagger, J. Phys. A: Gen. Phys. **1**, 539 (1968).

[140] R. Bianco, I. Errea, L. Paulatto, M. Calandra, and F. Mauri, Second-order structural phase transitions, free energy curvature, and temperature-dependent anharmonic phonons in the self-consistent harmonic approximation: Theory and stochastic implementation, Phys. Rev. B **96**, 014111 (2017).

[141] G. Kieslich, S. Sun, and A. Cheetham, Solid-state principles applied to organic-inorganic perovskites: New tricks for an old dog, Chem. Sci. **5**, 4712 (2014).

[142] M. Filip and F. Giustino, The geometric blueprint of perovskites, Proc. Natl. Acad. Sci. USA **115**, 5397 (2018).

[143] X. Li, M. Kepenekian, L. Li, H. Dong, C. Stoumpos, R. Seshadri, C. Katan, P. Guo, J. Even, and M. Kanatzidis, Tolerance factor for stabilizing 3D hybrid halide perovskitoids using linear diammonium cations, J. Am. Chem. Soc. **144**, 3902 (2022).

[144] C. Motta, F. El-Mellouhi, S. Kais, N. Tabet, F. Alharbi, and S. Sanvito, Revealing the role of organic cations in hybrid halide perovskite $CH_3NH_3PbI_3$, Nat. Commun. **6**, 7026 (2015).

[145] E. Smecca, Y. Numata, I. Deretzis, G. Pellegrino, S. Boninelli, T. Miyasaka, A. La Magna, and A. Alberti, Stability of solution-processed $MAPbI_3$ and $FAPbI_3$ layers, Phys. Chem. Chem. Phys. **18**, 13413 (2016).

[146] M. Zacharias, H. Seiler, F. Caruso, D. Zahn, F. Giustino, P. Kelires, and R. Ernstorfer, Multiphonon diffuse scattering in solids from first principles: Application to layered crystals and two-dimensional materials, Phys. Rev. B **104**, 205109 (2021).

[147] T. Lanigan-Atkins, X. He, M. J. Krogstad, D. M. Pajerowski, D. L. Abernathy, G. N. M. Xu, Z. Xu, D.-Y. Chung, M. G. Kanatzidis, S. Rosenkranz, R. Osborn, and O. Delaire, Two-dimensional overdamped fluctuations of the soft perovskite lattice in $CsPbBr_3$, Nat. Mater. **20**, 977 (2021).

[148] F. Brivio, K. Butler, A. Walsh, and M. van Schilfgaarde, Relativistic quasiparticle self-consistent electronic structure of hybrid halide perovskite photovoltaic absorbers, Phys. Rev. B **89**, 155204 (2014).

[149] C. Davies, M. Filip, J. Patel, T. Crothers, C. Verdi, A. Wright, R. Milot, F. Giustino, M. Johnston, and L. Herz, Bimolecular recombination in methylammonium lead triiodide perovskite is an inverse absorption process, Nat. Commun. **9**, 293 (2018).

[150] M. Filip, J. Haber, and J. Neaton, Phonon screening of excitons in semiconductors: Halide perovskites and beyond, Phys. Rev. Lett. **127**, 067401 (2021).

[151] M. Sajedi, M. Krivenkov, D. Marchenko, J. Sánchez-Barriga, A. Chandran, A. Varykhalov, E. D. L. Rienks, I. Aguilera, S. Blügel, and O. Rader, Is there a polaron signature in angle-resolved photoemission of $CsPbBr_3$? Phys. Rev. Lett. **128**, 176405 (2022).

[152] Z. Yang, A. Surrente, K. Galkowski, A. Miyata, O. Portugall, R. J. Sutton, A. A. Haghighirad, H. J. Snaith, D. K. Maude, P. Plochocka, and R. J. Nicholas, Impact of the halide cage on the electronic properties of fully inorganic cesium lead halide perovskites, ACS Energy Lett. **2**, 1621 (2017).

[153] M. Baranowski, P. Plochocka, R. Su, L. Legrand, T. Barisien, F. Bernardot, Q. Xiong, C. Testelin, and M. Chamarro, Exciton binding energy and effective mass of $CsPbCl_3$: A magneto-optical study, Photon. Res. **8**, A50 (2020).

[154] K. Galkowski, A. Mitioglu, A. Miyata, P. Plochocka, O. Portugall, G. Eperon, J. T.-W. Wang, T. Stergiopoulos, S. Stranks, H. Snaith, and R. Nicholas, Determination of the exciton binding energy and effective masses for methylammonium and formamidinium lead tri-halide perovskite semiconductors, Energy Environ. Sci. **9**, 962 (2016).

[155] J. Perdew, M. Ernzerhof, and K. Burke, Rationale for mixing exact exchange with density functional approximations, J. Chem. Phys. **105**, 9982 (1996).

[156] I. Garba, L. Trombini, C. Katan, J. Even, M. Zacharias, M. Kepenekian, and G. Volonakis, Three-dimensional to layered halide perovskites: A parameter-free hybrid functional method for predicting electronic band gaps, ACS Mater. Lett. **7**, 1922 (2025).

[157] A. V. Andrianov, A. N. Aleshin, and L. B. Matyushkin, Terahertz vibrational modes in $CH_3NH_3PbI_3$ and $CsPbI_3$ perovskite films, JETP Lett. **109**, 28 (2019).

[158] Y. Lv, C. Yin, C. Zhang, X. Wang, Z.-G. Yu, and M. Xiao, Exciton-acoustic phonon coupling revealed by resonant excitation of single perovskite nanocrystals, Nat. Commun. **12**, 2192 (2021).

[159] Y. He, L. Matei, H. Jung, K. McCall, M. Chen, C. Stoumpos, Z. Liu, J. A. Peters, D. Y. Chung, B. W. Wessels, M. R. Wasielewski, *et al.*, High spectral resolution of gamma-rays at room temperature by perovskite $CsPbBr_3$ single crystals, Nat. Commun. **9**, 1609 (2018).

[160] M. Frenzel, M. Cherasse, J. Urban, F. Wang, B. Xiang, L. Nest, L. Huber, L. Perfetti, M. Wolf, T. Kampfrath, *et al.*, Nonlinear terahertz control of the lead halide perovskite lattice, Sci. Adv. **9**, eadg3856 (2023).

[161] V. Cherrette, F. Babbe, J. Cooper, and J. Zhang, Octahedral distortions generate a thermally activated phonon-assisted radiative recombination pathway in cubic $CsPbBr_3$ perovskite quantum dots, J. Phys. Chem. Lett. **14**, 8717 (2023).

[162] M. Sebastian, J. A. Peters, C. C. Stoumpos, J. Im, S. S. Kostina, Z. Liu, M. G. Kanatzidis, A. J. Freeman, and B. W. Wessels, Excitonic emissions and above-band-gap luminescence in the single-crystal perovskite semiconductors $CsPbBr_3$ and $CsPbCl_3$, Phys. Rev. B **92**, 235210 (2015).

[163] L. Lang, Y.-Y. Zhang, P. Xu, S. Chen, H. J. Xiang, and X. G. Gong, Three-step approach for computing band offsets and its application to inorganic ABX_3 halide perovskites, Phys. Rev. B **92**, 075102 (2015).

[164] Y. He, C. Stoumpos, I. Hadar, Z. Luo, K. McCall, Z. Liu, D. Y. Chung, B. W. Wessels, and M. G. Kanatzidis, Demonstration of energy-resolved γ-ray detection at room temperature by the $CsPbCl_3$ perovskite semiconductor, J. Am. Chem. Soc. **143**, 2068 (2021).

[165] V. Guilloux, T. Barisien, F. Bernardot, M. Bernard, F. Margaillan, S. Majrab, I. Stenger, E. Lhuillier, C. Testelin, M. Chamarro, *et al.*, Phonon modes and exciton-phonon interactions in $CsPbCl_3$ single nanocrystals, Physica E **151**, 115713 (2023).

[166] M. Sendner, P. Nayak, D. Egger, S. Beck, C. Müller, B. Epding, W. Kowalsky, L. Kronik, H. Snaith, A. Pucci, and R. Lovrinčić, Optical phonons in methylammonium lead halide perovskites and implications for charge transport, Mater. Horiz. **3**, 613 (2016).

[167] S. Fasahat, N. Fiuza-Maneiro, B. Schäfer, K. Xu, S. Gómez-Graña, M. I. Alonso, L. Polavarapu, and A. Goñi, Sign of the gap temperature dependence in $CsPb(Br, Cl)_3$ nanocrystals determined by Cs-rattler-mediated electron–phonon coupling, J. Phys. Chem. Lett. **16**, 1134 (2025).

[168] M. Nagai, T. Tomioka, M. Ashida, M. Hoyano, R. Akashi, Y. Yamada, T. Aharen, and Y. Kanemitsu, Longitudinal optical phonons modified by organic molecular cation motions in organic-inorganic hybrid perovskites, Phys. Rev. Lett. **121**, 145506 (2018).

[169] K. Boldyrev, V. Anikeeva, O. Semenova, and M. N. Popova, Infrared spectra of the $CH_3NH_3PbI_3$ hybrid perovskite: Signatures of phase transitions and of organic cation dynamics, J. Phys. Chem. C **124**, 23307 (2020).

[170] V. Anikeeva, K. Boldyrev, O. Semenova, T. Sukhikh, and M. Popova, Broad-range high-resolution optical spectroscopy of $CH_3NH_3PbBr_3$ hybrid perovskite single crystals: Optical phonons, absorption edge, phase transitions, Opt. Mater.: X **20**, 100259 (2023).

[171] J. Wang, E. Motaharifar, L. N. Murthy, M. Higgins, D. Barrera, T. Daunis, Y. Zheng, A. Malko, F. Ely, M. Quevedo-Lopez, *et al.*, Revealing lattice and photocarrier dynamics of high-quality $MAPbBr_3$ single crystals by far infrared reflection and surface photovoltage spectroscopy, J. Appl. Phys. **125**, 025706 (2019).

[172] K. Cho, T. Yamada, H. Tahara, T. Tadano, H. Suzuura, M. Saruyama, R. Sato, T. Teranishi, and Y. Kanemitsu, Luminescence fine structures in single lead halide perovskite nanocrystals: Size dependence of the exciton–phonon coupling, Nano Lett. **21**, 7206 (2021).

[173] Y. Kawamura, H. Mashiyama, and K. Hasebe, Structural study on cubic–tetragonal transition of $CH_3NH_3PbI_3$, J. Phys. Soc. Jpn. **71**, 1694 (2002).

[174] M. Schlipf, S. Poncé, and F. Giustino, Carrier lifetimes and polaronic mass enhancement in the hybrid halide perovskite $CH_3NH_3PbI_3$ from multiphonon Fröhlich coupling, Phys. Rev. Lett. **121**, 086402 (2018).

[175] H. Mashiyama, Y. Kawamura, E. Magome, and Y. Kubota, Displacive character of the cubic-tetragonal transition in $CH_3NH_3PbX_3$, J. Korean Phys. Soc. **42**, 1026 (2003).

[176] F. Zu, P. Amsalem, D. Egger, R. Wang, C. Wolff, H. Fang, M. Loi, D. Neher, L. Kronik, S. Duhm, and N. Koch, Constructing the electron. struct. of $CH_3NH_3PbI_3$ and $CH_3NH_3PbBr_3$ perovskite thin films from single-crystal band structure measurements, J. Phys. Chem. Lett. **10**, 601 (2019).

[177] Y. Takahashi, R. Obara, Z.-Z. Lin, Y. Takahashi, T. Naito, T. Inabe, S. Ishibashi, and K. Terakura, Charge-transport in tin-iodide perovskite $CH_3NH_3SnI_3$: Origin of high conductivity, Dalton Trans. **40**, 5563 (2011).

[178] Z. Muhammad, P. Liu, R. Ahmad, S. Jalali Asadabadi, C. Franchini, and I. Ahmad, Tunable relativistic quasiparticle electronic and excitonic behavior of the $FAPb(I_{1-x}Br_x)_3$ alloy, Phys. Chem. Chem. Phys. **22**, 11943 (2020).

[179] D. Fabini, C. Stoumpos, G. Laurita, A. Kaltzoglou, A. G. Kontos, P. Falaras, M. G. Kanatzidis, and R. Seshadri, Reentrant structural and optical properties and large positive thermal expansion in perovskite formamidinium lead iodide, Angew. Chem. Int. Ed. **55**, 15392 (2016).

[180] E. Schueller, G. Laurita, D. Fabini, C. Stoumpos, M. Kanatzidis, and R. Seshadri, Crystal structure evolution and notable thermal expansion in hybrid perovskites formamidinium tin iodide and formamidinium lead bromide, Inorg. Chem. **57**, 695 (2018).

[181] S. Govinda, B. Kore, D. Swain, A. Hossain, C. De, T. Guru Row, and D. D. Sarma, Critical comparison of $FAPbX_3$ and $MAPbX_3$ ($X = Br$ and Cl): How do they differ? J. Phys. Chem. C **122**, 13758 (2018).

[182] M. I. Dar, G. Jacopin, S. Meloni, A. Mattoni, N. Arora, A. Boziki, S. Zakeeruddin, U. Rothlisberger, and M. Grätzel, Origin of unusual bandgap shift and dual emission in organic-inorganic lead halide perovskites, Sci. Adv. **2**, e1601156 (2016).

[183] J. Even, Pedestrian guide to symmetry properties of the reference cubic structure of 3D all-inorganic and hybrid perovskites, J. Phys. Chem. Lett. **6**, 2238 (2015).

[184] X. Gonze and C. Lee, Dynamical matrices, Born effective charges, dielectric permittivity tensors, and interatomic force constants from density-functional perturbation theory, Phys. Rev. B **55**, 10355 (1997).

[185] J. Lahnsteiner and M. Bokdam, Anharmonic lattice dynamics in large thermodynamic ensembles with machine-learning force fields: $CsPbBr_3$, a phonon liquid with Cs rattlers, Phys. Rev. B **105**, 024302 (2022).

[186] Y. Dang, Y. Zhou, X. Liu, D. Ju, S. Xia, H. Xia, and X. Tao, Formation of hybrid perovskite tin iodide single crystals by top-seeded solution growth, Angew. Chem. Int. Ed. **55**, 3447 (2016).

[187] T. Handa, H. Tahara, T. Aharen, A. Shimazaki, A. Wakamiya, and Y. Kanemitsu, Large thermal expansion leads to negative thermo-optic coefficient of halide perovskite $CH_3NH_3PbCl_3$, Phys. Rev. Mater. **4**, 074604 (2020).

[188] Y. Rakita, S. Cohen, N. Kedem, G. Hodes, and D. Cahen, Mechanical properties of $APbX_3$ ($A = Cs$ or CH_3NH_3; $X = I$ or Br) perovskite single crystals, MRS Commun. **5**, 623 (2015).

[189] P. S. Whitfield, N. Herron, W. E. Guise, K. Page, Y. Q. Cheng, I. Milas, and M. K. Crawford, Structures, phase transitions and tricritical behavior of the hybrid perovskite methyl ammonium lead iodide, Sci. Rep. **6**, 35685 (2016).

[190] S. Poncé, Y. Gillet, J. Laflamme Janssen, A. Marini, M. Verstraete, and X. Gonze, Temperature dependence of the electronic structure of semiconductors and insulators, J. Chem. Phys. **143**, 102813 (2015).

[191] A. Miglio, V. Brousseau-Couture, E. Godbout, G. Antonius, Y.-H. Chan, S. Louie, M. Côté, M. Giantomassi, and X. Gonze, Predominance of non-adiabatic effects in zero-point renormalization of the electronic band gap, npj Comput. Mater. **6**, 167 (2020).

[192] M. Engel, H. Miranda, L. Chaput, A. Togo, C. Verdi, M. Marsman, and G. Kresse, Zero-point renormalization of the band gap of semiconductors and insulators using the projector augmented wave method, Phys. Rev. B **106**, 094316 (2022).

[193] G. Antonius, S. Poncé, P. Boulanger, M. Côté, and X. Gonze, Many-body effects on the zero-point renormalization of the band structure, Phys. Rev. Lett. **112**, 215501 (2014).

[194] A. Marini, S. Poncé, and X. Gonze, Many-body perturbation theory approach to the electron-phonon interaction with density-functional theory as a starting point, Phys. Rev. B **91**, 224310 (2015).

[195] P. Giannozzi, *et al.*, QUANTUM ESPRESSO: A modular and open-source software project for quantum simulations of materials, J. Phys.: Condens. Matter **21**, 395502 (2009).

[196] P. Giannozzi, *et al.*, Advanced capabilities for materials modelling with Quantum ESPRESSO, J. Phys.: Condens. Matter **29**, 465901 (2017).

[197] D. R. Hamann, Optimized norm-conserving Vanderbilt pseudopotentials, Phys. Rev. B **88**, 085117 (2013).

[198] M. J. van Setten, M. Giantomassi, E. Bousquet, M. J. Verstraete, D. R. Hamann, X. Gonze, and G.-M. Rignanese, The PseudoDojo: Training and grading a 85 element optimized norm-conserving pseudopotential table, Comput. Phys. Commun. **226**, 39 (2018).

[199] J. Perdew, A. Ruzsinszky, G. Csonka, O. Vydrov, G. Scuseria, L. Constantin, X. Zhou, and K. Burke, Restoring the density-gradient expansion for exchange in solids and surfaces, Phys. Rev. Lett. **100**, 136406 (2008).

[200] C. Adamo and V. Barone, Toward reliable density functional methods without adjustable parameters: The PBE0 model, J. Chem. Phys. **110**, 6158 (1999).

[201] G. Kresse and J. Furthmüller, Efficient iterative schemes for *ab initio* total-energy calculations using a plane-wave basis set, Phys. Rev. B **54**, 11169 (1996).

[202] G. Kresse and D. Joubert, From ultrasoft pseudopotentials to the projector augmented-wave method, Phys. Rev. B **59**, 1758 (1999).

[203] F. Lehmann, A. Franz, D. Többens, S. Levcenco, T. Unold, A. Taubert, and S. Schorr, The phase diagram of a mixed halide (Br, I) hybrid perovskite obtained by synchrotron x-ray diffraction, RSC Adv. **9**, 11151 (2019).

[204] Y. Wang, J. Wang, W. Wang, Z. Mei, S. Shang, L. Q. Chen, and Z. Liu, A mixed-space approach to first-principles calculations of phonon frequencies for polar materials, J. Phys.: Condens. Matter **22**, 202201 (2010).

[205] M. Zacharias, H. Seiler, F. Caruso, D. Zahn, F. Giustino, P. Kelires, and R. Ernstorfer, Efficient first-principles methodology for the calculation of the all-phonon inelastic scattering in solids, Phys. Rev. Lett. **127**, 207401 (2021).

[206] L.-M. Peng, S. Dudarev, and M. Whelan, *High-energy Electron Diffraction and Microscopy* (Oxford University Press, Oxford, UK, 2004).

[207] F. Giustino, *Materials Modelling Using Density Functional Theory: Properties and Predictions* (Oxford University Press, Oxford, UK, 2014), p. 199.

[208] J. Xu, K. Li, U. Huynh, M. Fadel, J. Huang, R. Sundararaman, V. Vardeny, and Y. Ping, How spin relaxes and dephases in bulk halide perovskites, Nat. Commun. **15**, 188 (2024).

[209] S. Boehme, T. P. Nguyen, C. Zhu, I. Cherniukh, L. Feld, D. Dirin, M. Bodnarchuk, C. Katan, J. Even, M. Kovalenko, and G. Rainò, Single-photon superabsorption in $CsPbBr_3$ perovskite quantum dots, Nat. Photon. **19**, 864 (2025).

[210] M. Zacharias, Nomad dataset: Database of polymorphous halide perovskites+ZG structures (2025), http://doi.org/10.17172/NOMAD/2025.09.03-1.

[211] L. Ranalli, C. Verdi, M. Zacharias, J. Even, F. Giustino, and C. Franchini, Electron mobilities in $SrTiO_3$ and $KTaO_3$: Role of phonon anharmonicity, mass renormalization, and disorder, Phys. Rev. Mater. **8**, 104603 (2024).

[212] F. Caruso, Nonequilibrium lattice dynamics in monolayer MoS_2, J. Phys. Chem. Lett. **12**, 1734 (2021).

[213] R. Jinnouchi, J. Lahnsteiner, F. Karsai, G. Kresse, and M. Bokdam, Phase transitions of hybrid perovskites simulated by machine-learning force fields trained on the fly with Bayesian inference, Phys. Rev. Lett. **122**, 225701 (2019).

[214] O. Unke, S. Chmiela, H. Sauceda, M. Gastegger, I. Poltavsky, K. Schütt, A. Tkatchenko, and K.-R. Müller, Machine learning force fields, Chem. Rev. **121**, 10142 (2021).

[215] A. Manoli, P. Papagiorgis, K. Gahlot, K. Georgiou, E. Lioudakis, A. Othonos, L. Protesescu, and G. Itskos, Optical properties of thin films of tin iodide perovskite nanostructures, Adv. Opt. Mater. **13**, 2500792 (2025).

[216] A. Pisoni, J. Jaćimović, O. Barišić, M. Spina, R. Gaál, L. Forró, and E. Horváth, Ultra-low thermal conductivity in organic–inorganic hybrid perovskite $CH_3NH_3PbI_3$, J. Phys. Chem. Lett. **5**, 2488 (2014).

[217] W. Lee, H. Li, A. Wong, D. Zhang, M. Lai, Y. Yu, Q. Kong, E. Lin, J. Urban, J. Grossman, and P. Yang, Ultralow thermal conductivity in all-inorganic halide perovskites, Proc. Natl. Acad. Sci. USA **114**, 8693 (2017).

[218] T. Haeger, R. Heiderhoff, and T. Riedl, Thermal properties of metal-halide perovskites, J. Mater. Chem. C **8**, 14289 (2020).

[219] https://lumi-supercomputer.eu.